DUAL-POLARIZATION CLOUD LIDAR

DESIGN AND CHARACTERIZATION

by

Nathan Lewis Seldomridge

A thesis submitted in partial fulfillment
of the requirements of the degree

of

Master of Science

in

Electrical Engineering

MONTANA STATE UNIVERSITY
Bozeman, Montana

June 2005

APPROVAL

of a thesis submitted by

Nathan Lewis Seldomridge

This thesis has been read by each member of the thesis committee and has been found to be satisfactory regarding content, English usage, format, citations, bibliographic style, and consistency, and is ready for submission to the College of Graduate Studies.

Dr. Joseph A. Shaw,
Chair of Committee

Approved for the Department of Electrical and Computer Engineering

Dr. James N. Peterson,
Department Head

Approved for the College of Graduate Studies

Dr. Bruce R. McLeod,
Graduate Dean

STATEMENT OF PERMISSION TO USE

Nathan Lewis Seldomridge

June 1st, 2005

ACKNOWLEDGEMENTS

I thank my advisor Dr. Joseph Shaw for his guidance in this project and for sharing the contagious enjoyment that he takes in all his work. I also thank Dr. James Churnside and James Wilson at the NOAA Environmental Technology Laboratory for their advice and occasional collaboration over the past few years. Dr. Bruce Davis, at the NASA Stennis Space Center, encouraged this project by supporting me with a Graduate Student Researchers Program (GSRP) fellowship.

TABLE OF CONTENTS

TABLE OF CONTENTS – CONTINUED

LIST OF TABLES

LIST OF FIGURES

LIST OF FIGURES – CONTINUED

ABSTRACT

Lidar has proven to be a very useful tool in many kinds of atmospheric research and remote sensing applications. Specialized lidar instruments have been built to detect certain atmospheric constituents, some with additional capabilities such as polarization sensitivity or multiple wavelength operation. Many lidar systems are large, expensive and designed for one application only.

This thesis describes the design and characterization of a lidar system for the direct detection of clouds, but which is versatile enough to be reconfigured for other applications. The source is an Nd:YAG laser at a wavelength of 532 nm and with pulse energies of 118 mJ. A dual-polarization receiver is implemented with a liquid crystal polarization rotator. The system is designed to be compact (a 31 cm × 46 cm × 97 cm optics package plus a half-size rack of electronics) and robust enough for transport and deployment. The control software was developed in LabVIEW and runs on a Windows platform. These design criteria make the system useful both as a science tool and as an educational tool.

Information on local cloud coverage, with high spatial and temporal resolution, is useful for studying how the radiative properties of clouds affect the climate. The resolution of a lidar allows for detection of subvisual cloud and aerosol layers, and for determining particle sizes of the scatterers. A cloud lidar sensitive to polarization can distinguish between ice and water in clouds, since ice crystals are more depolarizing than water droplets. Cloud lidars complement either ground-based or space-based cloud imagers by supplying the missing vertical dimension.

Data presented show the lidar system is capable of detecting clouds up to 9.5 km above ground level (the normal operating range is 15 km) with a 3 m range resolution. Two orthogonal polarization states are measured on alternate laser pulses (at 30 pulses/second). Polarization discrimination is sufficient to measure depolarization ratios with better than 0.4% accuracy. The receiver field of view is conveniently variable up to 8.8 mrad. Daytime operation is possible, thanks to laser-line interference filters and a gated photomultiplier tube.

CHAPTER 1

INTRODUCTION

Overview of Lidar in Environmental Applications

Lidar – an acronym for Light Detection And Ranging – is a remote sensing technique analogous to radar, except with a laser as the source of radiation. In both cases, short pulses of radiation are emitted by the instrument and scattered off some distant target. Subsequently, the backscattered light is detected and sampled as a function of time, and this signal is translated into a spatial profile of the scattering intensity. Lidar has been used to study the atmosphere for over 40 years now, almost since the very advent of the laser, and the same basic idea was carried out with other pulsed-light sources decades before that (Collis 1966; Collis and Ligda 1966).

Compared to radar, lidar instruments have a narrower field of view and a much higher sensitivity to certain targets. Higher sensitivity for lidars is the result of stronger scattering for laser wavelengths by the relevant aerosol and cloud particle sizes, compared to radio wavelengths. Stronger scattering can be a fault when it comes to penetrating through optically thick media, and so lidars tend to have more signal extinction to worry about than radars have. The narrow field of view of lidars results from the low divergence of laser beams. By concentrating laser power in a small angle, the receiver field of view can be made similarly narrow, limiting sky noise and allowing lidars to see deeper than they otherwise would.

Major innovations in laser technology, as they were developed, have been taken advantage of in different types of lidar instruments. Raman lidars measure a specific atmospheric constituent by detecting the unique wavelength-shifted Raman scattering for the molecule of interest. This was first demonstrated with Raman scattering of nitrogen (Leonard 1967; Cooney 1968), but has since been accomplished on water vapor, which is a more interesting problem due to its variability and effects on climate (Melfi and Whiteman 1985; Whiteman et al. 1992). Raman lidars usually require high power ultraviolet lasers and large receiver telescopes.

Differential absorption (DIAL) lidars use laser wavelength tunability to identify atmospheric constituents with particular molecular absorption lines. This technique was first tried early in the history of lidar, with a thermally tuned ruby laser (Schotland 1966). Since then, DIAL has been shown to have significantly more potential sensitivity and range than Raman lidar for detecting specific atmospheric constituents (Byer and Garbuny 1973). Advances in the DIAL technique have been led by more precise knowledge of how absorption cross sections vary with temperature and pressure, and the development of high power, stable, tunable laser sources (Grant 1991). DIAL has usefully been employed in measurements of ozone (Browell 1989) and water vapor (Grant 1991; Wulfmeyer and Walther 2001), for example.

Doppler lidars make use of the coherence of narrow line-width frequency-stable laser light to measure the velocity of the scatterers. An acousto-optic modulator and amplifier combination is often used to produce RF-modulated lidar pulses. The received lidar signal is combined with the local oscillator to measure beats. High-bandwidth detection and signal processing are required. With this technique, three-dimensional wind field measurements have been made with CO_2 lasers (Post et al. 1981) Nd:YAG lasers (Kane et al. 1987; Hawley et al. 1993), and other solid-state mid-infrared lasers (Frehlich et al. 1997).

A micro pulse lidar (MPL) is a simple direct-detection lidar with low pulse energy and a high pulse repetition rate. The high pulse rate and some temporal averaging result in a range and sensitivity similar to a traditional (large pulse) lidar. The principal advantage is that the combination of small pulse energies and an expanded beam allow for eye-safe – and therefore, unattended – operation. Rather than digitizing a signal from a photomultiplier tube for every laser pulse, pulses from a photon-counting avalanche photo diode (APD) are counted with a multichannel scaler. This technique was made possible by the development of these detectors, as well as by the development of small diode-pumped lasers with pulse repetition rates of 2-5 kHz. Other than the capability for unattended operation, micro pulse lidars have the added advantage of being compact and relatively inexpensive. These features make them ideal for distribution to many remote sites and for constant and long-term monitoring of aerosols and clouds. A potential problem for micro pulse lidars is sky noise, which is a bigger component of the measured signal than for traditional lidars. Common strategies for reducing noise include using a narrow optical filter bandwidth, such as 0.2 nm, and a narrow receiver field of view, such as 100 μrad (Spinhirne 1993; Campbell et al. 2002).

The lidar described in this thesis is intended to be useful for cloud and aerosol measurements, as well as for some airborne applications, such as the detection of vegetation or fish schools. So before I discuss more cloud and aerosol lidars and their usefulness, I would like to round out what has become a diverse picture of lidar applications by acknowledging a few lidars that have found their way into airborne platforms. The most famous of these is NASA's Lidar In-space Technology Experiment (LITE), which was flown on the shuttle in 1994 (Winker et al. 1996). LITE is three-wavelength Nd:YAG backscatter lidar designed primarily for measuring clouds and aerosols. Space-based lidar has the advantage of seeing the atmosphere from a perspective in which dense low clouds don't obstruct the view of thin high clouds, so layered structure is observed with more accuracy. Also, the signal dynamic range is compressed somewhat by being far away from all the scatterers.

Lidar has also been used in airborne applications that look at the earth's surface instead of the atmosphere. While airborne imagers can classify regions as forested or otherwise, they have difficulty quantifying a vegetation canopy structure. A lidar flown on an airplane can measure the vertical dimension with high resolution, so it complements the capabilities of an imager. And beyond this simple laser altimetry, using multiple laser wavelengths and measuring the polarization of the return gives information that can be used to discriminate between tree species (Tan and Narayanan 2004). On the other hand, for mapping ground elevation, the effect of vegetation must be removed. This requires some combination of reducing the laser footprint, increasing the pulse rate, and developing an algorithm to distinguish between ground and canopy (Hodgson et al. 2003).

The same general type of lidar has also been used to detect schools of fish. The common 532 nm wavelength is effective for transmission through water. An airborne lidar fish survey can be cheaper, for the coverage area, compared to surveys conducted by boat, and more accurate than airborne spotting by eye. This has been shown to be effective for water depths up to 20 m during the day and 36 m at night (Churnside et al. 2001).

Motivation for Lidar Cloud Research

Why use a lidar to detect clouds? The radiative properties of clouds, along with those of water vapor, may be the most important factors in the heat budget of the earth, and as such, their effect on the climate is key (Liou 2002, chapter 8). The effects of clouds are not always the same; they depend on the ice or water particle shapes, sizes and concentrations, and on the vertical position of the cloud in the atmosphere.

Low-altitude water clouds tend to be optically thick. Liquid cloud droplets have radii of approximately 10-50 μm, and concentrations of approximately 1-1000 cm^{-3} (Rogers and Yau 1989, chapter 5). A known or assumed drop-size distribution allows you to calculate liquid-water content from a lidar-measured backscatter cross-section (Reagan et al. 1989). The density of these clouds makes them good reflectors of short-wave solar radiation, and they absorb and re-emit thermal infrared (IR) radiation like a blackbody with a temperature near that of the earth's surface. These clouds have a net cooling influence on the earth's surface, because the low short-wave transmission ultimately reduces the IR emission from the surface that is available to be trapped by the clouds.

High-altitude cirrus clouds tend to be much less optically dense. The name "cirrus" is given to clouds with a filament-like or wispy appearance, and these are typically found at altitudes between 6-12 km. Below about -40 °C, they can be treated as composed exclusively of ice crystals of various hexagonal shapes, ranging in size from 10-2000 μm, but the great majority of crystals are less than 200 μm. The largest crystals create characteristic fallstreaks in the sky. Temperature is the dominant control of ice crystal size, with lower temperatures (higher altitudes) reducing crystal sizes (Heymsfield and Platt 1984). The particle number density ranges from 0.1-1.0 cm^{-3} (Liou 1986). Cirrus cloud blackbody emissivities are down around 0.47 (Liou 1986), so they are not good blackbodies, but the infrared absorption and re-emission is still important. Cloud emissivity can be calculated with cloud height data from a lidar and radiance data from a radiometer. Despite sometimes being composed of very small particles (which tend to be *more* reflective of short-wave solar energy), cirrus clouds reflect less solar energy (R ~ 20%) than low clouds because of the lower water/ice content. The combination of the high transmission of visible solar energy and the absorption and re-emission of exiting IR from the earth's surface means that cirrus clouds tend to have a net greenhouse warming effect on the earth-atmosphere system.

Feedback between clouds and the climate is thought to be significant, and it is not clear how to tell if the feedback is negative – they regulate each other, or positive – each amplifying a change in the other (McGuffie and Henderson-Sellers 2001). For example, an increase in temperature could increase the proportion of water, as opposed to ice, in clouds. This would have a cooling effect, by the reflection of more solar radiation, and thus, negative feedback. Alternatively, surface warming can provide more efficient conditions for precipitation which would reduce the quantity of low clouds. Since low clouds are those that usually provide cooling, this is an example of positive feedback (Liou 1986).

A full accounting of factors affecting the climate would have to include natural aerosols and pollutants, even though their densities, on the order of 10^{-6} g/kg, are much less than those of clouds, which are on the order of 1 g/kg (Reagan et al. 1989). Aerosols can have a direct radiative effect on climate, by absorption or scattering, or they may have an indirect effect, by acting as condensation or deposition nuclei for the formation of clouds. For example, airplane contrails are made of ice crystals which have been formed on engine exhaust particles. The air at low temperatures is often supersaturated with water vapor, and only lacks nuclei on which to form ice crystals. This adds to the natural amount of cirrus-type clouds, and could potentially warm a climate locally (Liou et al. 1998). Natural aerosols such as dust can have the same effect. For example, Asian dust has been suggested to have influenced the formation of ice clouds over Alaska (Sassen 2005).

"Subvisual" cirrus is a category of cloud that is sometimes vaguely defined as too thin to see by eye. Somewhat more precisely, they have been defined as having optical thicknesses ≤ 0.03 (Sassen et al. 1989; Sassen and Cho 1992). Sometimes they are the result of spreading contrail cirrus. These clouds also presumably have a net warming effect on the climate, but this is not easy to measure. Subvisual cirrus is easily missed by satellite imagery, although it can be seen in the infrared if you have enough information for positive identification, so more information is needed on the characteristics and frequency of these clouds.

The feedback between clouds and the climate is affected by both the size and shape of ice crystals. For a given water content, smaller ice crystals have more area and absorb more short-wave radiation, and this warming, which occurs moreso in tropical regions, affects moisture distributions (Kristjánsson et al. 2000). Complicated ice crystal shapes tend to reflect more solar energy compared to spherical particles of the same dimension (Liou et al. 1998).

In summary, the relationship between clouds and climate cannot be understood by measuring two-dimensional cloud coverage alone. The net radiative effect of various clouds depends strongly on their vertical distribution and microphysical properties. A lidar is uniquely suited to measure both of these, and thus, a lidar complements the role of a cloud imager.

The Lidar Equation

The lidar equation gives the expected optical signal power incident on the detector as a function of range. In general, contributions to the signal come from background skylight, elastic single scattering of laser light, elastic multiple scattering of laser light, and any inelastic scattering. This instrument is a direct-detection elastic lidar, not a Raman lidar, so the detected wavelength is the same as the transmitted wavelength; inelastic scattering is irrelevant. Multiple scattering and background light can be significant, but strategies are employed to minimize or compensate for them. Single scattering is usually the desirable part of the signal.

The lidar equation for single scattering power *P(r)* at the detector is:

$$P(r) = P_0 \xi_\lambda \frac{A}{r^2} \frac{c\tau_0}{2} \beta_\pi(r) \xi(r) \exp\left[-2\int_0^r \kappa_t(x)\,dx\right]. \qquad (1.1)$$

In this equation and in what follows, I have used parts of the form and notation from Measures (1984, chapter 7) and parts from Kovalev and Eichinger (2004, chapter 3.) P_0 is the peak optical power of the laser transmitter during the pulse, and assumes a square pulse shape in time. All the other terms modify this power, dictating the fraction of the transmitted light that, having been backscattered from range *r*, will arrive back at the detector. The constant ξ_λ is the optical transmission of the receiver for the appropriate wavelength. A/r^2 is the solid angle, in units of steradians (sr), of the receiver aperture area *A* as viewed from the scattering particle at range *r*. The range is assumed to be large enough that the signal scales linearly with this solid angle.

The laser pulse duration is τ_0, so the pulse length in space is $c\tau_0$. In any particular sample of the detector, light is being measured that was backscattered from ranges extending over half a pulse length. One way to think about this is that the pulse duration represents an ambiguity in the round-trip time from transmission to reception, so half of the pulse duration, converted to a distance with the speed of light, is the uncertainty in the one-way range measurement. I will return to the subject of range resolution in the design chapter, but the purpose here is to show that the range being instantaneouly sampled is $c\tau_0/2$ deep. The scatterers, whether molecular or particulate, have a backscatter cross-section volume density β_π. The cross-sectional area is the effective particle size – the size of a perfect isotropic scatterer which would produce the observed scattering in the backwards direction (π scattering angle). The volume density of these particles represents the probability of incident light being scattered in the backwards direction, per unit solid angle. β_π has dimensions of area per solid angle per volume, usually given in $m^{-1}sr^{-1}$. β_π is a function of range, because the types and densities of scattering particles vary. In fact, often the goal is to solve lidar equation to back out $\beta_\pi(r)$. The m^{-1} part of the units of $\beta_\pi(r)$ should be thought of as canceling the units of depth of the sampled range, $c\tau_0/2$ [m], while the sr^{-1} part cancels the units of the receiver solid angle. ξ(r) is the overlap factor, which is fractional overlap of the laser spot and telescope field of view as a function of range. This depends on laser divergence, receiver field of view, and the horizontal separation and inclination angle between the two. Ideally, the overlap is complete and this factor is one. The last term, the exponential, is the two-way transmittance of the atmosphere between the lidar and the sampled range. $\kappa_t(r)$ [m^{-1}] is the total (particulate and molecular) extinction coefficient, representing losses due to light being scattered out of the beam as well as due to absorption.

It is difficult to compute the overlap accurately enough to give useful data in regions of partial overlap. This is mainly because the overlap is heavily dependent on the angle between telescope and laser, which is hard to measure. Further complications result from non-gaussian beam shapes and the effect of turbulence on the energy distribution in the beam. Overlap functions can be empirically derived from lidar measurements in sufficiently homogeneous atmospheric conditions. Often, *a priori* calculations of the overlap function serve only to estimate the region of complete overlap (I perform this calculation in the chapter on characterization). If we restrict the region of interest to where the overlap factor is one, and split the extinction integral into two parts (one for the region of interest and one for before that region), then we can rewrite the lidar equation as:

$$P(r) = P_0 \xi_\lambda \frac{A}{r^2} \frac{c\tau_0}{2} \beta_\pi(r) T_0^{\,2} \exp\left[-2\int_{r_0}^{r} \kappa_t(x)\,dx\right], \qquad (1.2)$$

where

$$T_0 = \exp\left[-\int_0^{r_0} \kappa_t(x)dx\right], \tag{1.3}$$

and there is complete overlap for ranges from r_0 to r. This manipulation is worthwhile in cases where T_0 (the transmission up to the region of complete overlap) can be considered constant, such as over a data session of a few hours. Then if all the constant terms are grouped together in one set of parentheses, we have:

$$P(r) = \left(P_0 \xi_\lambda T_0^{\ 2} A \frac{c\tau_0}{2}\right)\frac{\beta_\pi(r)}{r^2}\exp\left[-2\int_{r_0}^{r} \kappa_t(x)dx\right]. \tag{1.4}$$

This shows that, in cases where extinction is small, the signal is proportional to the backscatter cross-section volume density divided by the range-squared. A "range-corrected signal," $Z_r(r)$, obtained by multiplying the signal by r^2, is useful because of its direct proportionality to the density of scatterers:

$$Z_r(r) = r^2 P(r) = \left(P_0 \xi_\lambda T_0^{\ 2} A \frac{c\tau_0}{2}\right)\beta_\pi(r)\exp\left[-2\int_{r_0}^{r} \kappa_t(x)dx\right]. \tag{1.5}$$

For a homogeneous atmosphere (in which β_π and κ_t are constant), the natural logarithm of the range-corrected signal is linear with range, and has slope $-2\kappa_t$. The extinction is figured from this slope, and inhomogeneities (such as clouds or aerosol layers) can be automatically identified as deviations from otherwise linear data.

In this discussion, I have not dealt with the responsivity of the detector or effects related to digitizing its signal. I present details of the data analysis and a detector gain calibration in the chapter on characterization.

Capabilities of a Dual-Polarization Cloud Lidar

A dual-polarization lidar is one that separates the backscattered light into two orthogonal linear polarization states, and measures each in a separate signal channel. The laser source is linearly polarized, so the two received states are measured with respect to the source and are termed "co-polarized" and "cross-polarized." The amplitude of the co-pol signal gives the usual lidar information about the strength of the backscattering interaction. The added capability of a dual-polarization lidar is that a comparison of the co-pol and cross-pol signals can be used to distinguish between different shapes of scattering particles.

Such a comparison employs the depolarization ratio, δ, the ratio of the received cross-polarized and co-polarized signals ($P_\perp$ and $P_\parallel$, respectively). This ratio is the same as the ratio of cloud or aerosol backscattering cross sections per unit volume for each polarization ($\beta_\perp$ and $\beta_\parallel$). Everything else in the lidar equation cancels out in the ratio, except for possible atmospheric transmission differences. Since molecular scattering cross section densities are more than a thousand times smaller than those of cloud particles at this wavelength (Measures, 1984, p. 42 calculates rayleigh scattering from a standard atmosphere as a function of wavelength), and since any depolarization due to atmospheric transmission would be a much smaller effect than that, the depolarization ratio can be ascribed directly to scattering properties of the cloud particles (Schotland et al. 1971):

$$\delta(r) = \frac{P_\perp(r)}{P_\parallel(r)} = \frac{\beta_\perp(r)}{\beta_\parallel(r)}. \tag{1.6}$$

When applied to clouds, dual-polarization lidar (called, more generally, "polarization diversity lidar" by Sassen, 1994) allows discrimination between quasi-spherical liquid cloud droplets and polyhedral ice crystals. I will now give a brief description of ice crystal shapes and demonstrate how ice crystals introduce a cross-polarized signal. I will also describe characteristic depolarization signatures of various types of clouds, and note common problems with this technique.

The basic shapes of natural crystals are usually hexagonal; they include columns, plates, and dendrites. Liou and Hansen (1971) showed that for particle radii greater than $400\lambda/2\pi$ (34 μm for λ = 532 nm), scattering can be treated to good approximation with geometrical ray tracing (for reflection and refraction) plus the far field diffraction. These approximate the full Mie scattering theory. Of most interest are the rays that exit the crystal in the exact backwards direction – rays that would be detected by the lidar. Liou and Lahore (1974) found that most of the backscattered energy from single scattering in a group of randomly oriented hexagonal plates or columns is the result of precisely two internal reflections. In contrast, for a spherical water droplet, the backscatter is primarily the result of an edge ray, which travels by surface waves, though a small contribution comes from a central ray (Figure 1).

Reflection and refraction are treated with the Fresnel equations (Saleh and Teich 1991, chapter 6). For the trivial normal-incidence case, these equations show that light is reflected the same amount regardless of the incident polarization – there is no preferred orientation in the geometry of the problem. Therefore, the backscattered light has the same polarization as the incident light for the normal-incidence case. On the other hand,

Figure 1. Primary backscatter ray paths for common particle shapes: a sphere, a hexagonal plate, and a hexagonal column (after Liou and Lahore 1974).

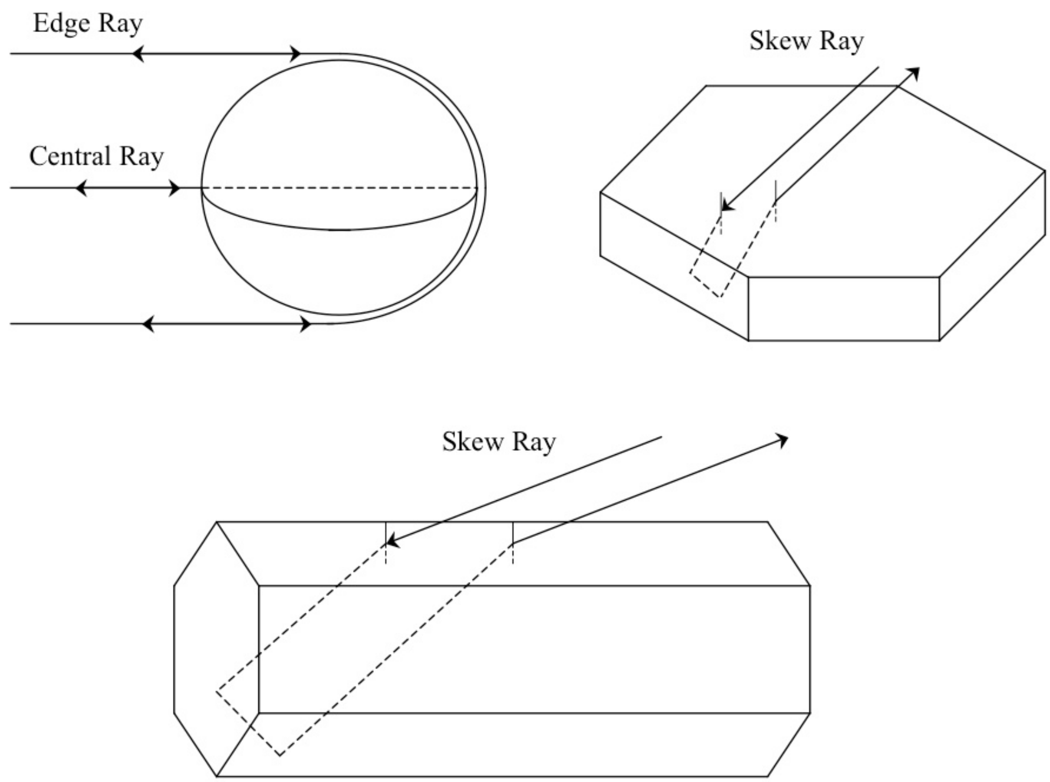

for light incident at an oblique angle, the equations show that the fraction reflected or transmitted, in general, is different for each component of the incident polarization (components defined in the plane of reflection, and orthogonal to it). This familiar effect is seen in the polarization of light reflected off the surface of a lake, and is what causes ice crystals to alter the polarization of the lidar beam. Consequentially, for a fixed laser source polarization, the polarization of the backscattered light (which is the result of a transmission, two reflections and another transmission) depends on the ice crystal orientation. For a single ice crystal, the backscattered light could possibly be in *any* linear polarization, depending on the crystal shape and orientation. Perhaps it is best not to think of an ice crystal as *changing* the incident polarization state, so much as it *differentially backscatters* the components of the incident polarization state. For a randomly oriented ensemble of crystals, we should expect a significant cross-polarized component in addition to a co-polarized component. So there is a clear mechanism for backscatter depolarization of single-scattered light from ice crystals. For spherical water drops, there is no mechanism for depolarization apart from multiple scattering effects, a topic to which I will return.

At this point, I should note that determining the presence of ice is not as simple as measuring the air temperature. The freezing of liquid water requires a nucleation process, a stable beginning of a crystal on which the water molecules can order themselves. This nucleus is often a piece of foreign material, such as dust, and separate nuclei are required for each crystal. Without the presence of nuclei, water droplets smaller than 20 μm will not homogeneously freeze unless the temperature is below -39 °C (Wallace and Hobbs 1977, chapter 4). Larger drops freeze at slightly warmer temperatures. Liquid water below 0 °C is called “supercooled,” and it is not rare to find supercooled liquid clouds at -20 to -30 °C. Mixtures of ice and liquid water are common up to -5 °C, above which ice becomes rare.

If the atmosphere is saturated with water vapor, a 100% relative humidity, then it is supersaturated with respect to ice. For example, at -30 °C, an atmosphere just saturated with respect to water has a supersaturation of vapor with respect to ice of greater than 130% (Rogers and Yau 1989, chapter 9). The consequence is that once an ice crystal is started by heterogeneous nucleation, it quickly grows by diffusion of vapor onto the crystal surface. The combination of the temperature and the excess vapor density at the time of formation dictate the type of ice crystal: plates generally are formed at relatively warmer temperatures with high vapor supersaturations, and columns are formed at cold temperatures with only slight supersaturation of vapor. Since plates occur more frequently than columns in warmer temperatures, the fact that plates have a slightly greater chance of normal-incidence (low depolarization) scattering has been thought to account for slightly lower average lidar depolarization observed during the daytime, compared to night (Sassen et al. 2003).

Having described ice crystals and their depolarization mechanism, I will give the typical range of observed lidar depolarization values for ice and liquid water clouds. Early measurements on liquid droplets of 10 - 2000 μm diameter found $\delta = 0.03$ or less (Schotland et al. 1971), and the reason this is not zero is presumably due to multiple scattering. Scattering of light off one droplet, off another droplet, and then back toward the lidar involves reflection and refractions other than at normal incidence, and this is depolarizing. In the same study, ice crystals of 20 - 100 μm gave $\delta = 0.38$ and large crystals of > 350 μm gave $\delta > 0.8$. A depolarization ratio equal to one is the theoretical limit for randomly oriented particles. Sassen (1974) measured $\delta = 0.03$ for liquid water and $\delta = 0.5$ for ice. The values most often accepted for cloud depolarization are $\delta < 0.03$ for water and $\delta = 0.4$ to 0.5 for ice, though the value for ice can vary from 0.2 to 0.8 or so (Sassen 1991). A criterion that has been used to identify liquid-dominated mixed phase clouds is $\delta \leq 0.25$ (Sassen and Zhao 1993). Depolarizations larger than 0.7 are characteristic of snowflakes, because of their more complex shape. Differences in depolarization by different crystals is a result of the relative importance of normal-incident back-reflections off outside surfaces as opposed to reflections off inner surfaces, which involve oblique angles. As previously noted, columns and plates are very similar, but columns probably have depolarization ratios greater than those of plates by at least 0.02 (Sassen et al. 2003).

There are two common complications with the depolarization method of discrimination between ice and water. The first I have already mentioned, and that is depolarization due to multiple scattering of water droplets. Distinguishing between this depolarization and the depolarization due to single scattering from ice crystals can be a problem. This effect is worse with a wide receiver field of view, so a narrow field of view is desirable. Also, multiple scattering characteristically increases the depolarization ratio more with penetration depth in a cloud. Pal and Carswell (1973) measured near zero depolarization at the bottom of a water cloud, and an increase to $\delta = 0.4$ after about 150 m, with a 5 mrad field of view and a source divergence of less than 3 mrad. Another symptom of multiple scattering is the peak in the cross-polarized signal occuring about 40 m after the peak in the co-polarized signal, since singly scattered co-polarized light would return to the detector sooner than multiply scattered light which takes a more complex path. Multiple scattering will depend on droplet size and concentration as well as the receiver field of view.

The other common complication creates the opposite problem: ice crystals can generate zero depolarization and appear to be liquid water. In many cases, and especially if the crystals are large, ice crystals are not randomly oriented, but tend to fall with their long axes horizontal. This makes normal-incidence reflection the primary backscatter path. Platt et al. (1978) showed that some clouds previously classified as supercooled liquid at very cold temperatures were probably ice. The hypothesis can be tested by tilting the lidar by about 2.5° (Sassen 1991), to see if the depolarization jumps up. Very low crystal flutter angles have been observed; Platt et al. (1978) observed a 97% reduction in the cross-polarized signal with only a 0.5° tilt away from the zenith.

Incidentally, water phase discrimination by depolarization doesn't work for cloud radars, which observe rayleigh scattering from cloud particles. The shape of the particle does not affect the polarization for this combination of wavelength and particle size. Yet radars have the advantage of low extinction, so cloud tops can be seen from beneath.

The task of measuring cloud horizontal and vertical extent, visible extinction, infrared emissivity, and microphysical properties is best met by a number of different instruments. Data from one instrument can help interpret data from another. Along with instruments such as radars and radiometers, dual-polarization cloud lidars have proven to be an essential tool contributing to the complete picture.

This thesis describes the design and characterization of a lidar system for the direct detection of clouds, but which is versatile enough to be reconfigured for other applications. Other design criteria include dual-polarization receiver sensitivity, and a compact, robust package. Chapter 2 describes how these criteria are accomplished. Chapter 3 discusses sample data and assesses the performance of the instrument. Chapter 4 suggests directions for future work. The appendices provide specific instructions for operating the instrument and using the data.

CHAPTER 2

DESIGN

Overall Schematic

The lidar system is composed of a laser transmitter, a receiver telescope, receiver and detector optics, a signal digitizer, timing and power supply electronics, and a computer for control and data recording. Figure 2 shows a schematic of the relations between these parts. The laser pulses are triggered internally by the laser power supply at 30 Hz. A photo-diode near the laser detects the pulses and triggers a delay generator, which controls the timing of the rest of the system. The receiver consists of a telescope, a series of optical components in a light-tight box, and a gated photomultiplier tube (PMT)

Figure 2. Overall schematic of the lidar system. Optical components are shaded yellow and electrical components are shaded blue.

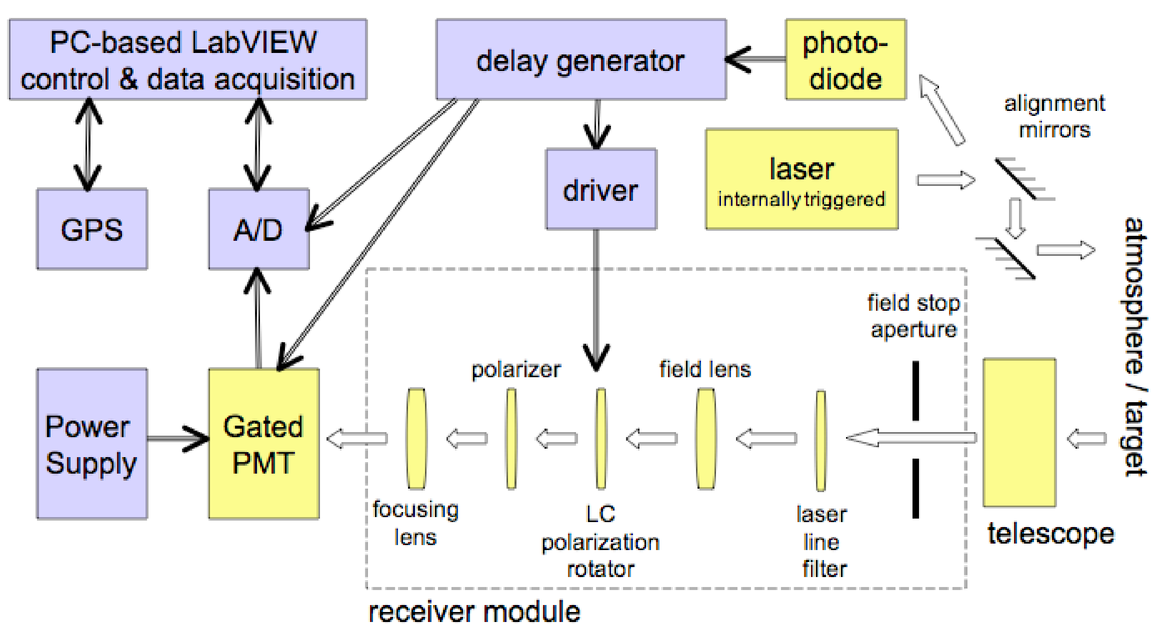

detector. A fast and high-resolution analog-to-digital (A/D) converter resides in the computer.

Figure 3 is a number of labeled photographs of the system, showing the locations of the major parts in the optics package and electronics rack. The optics package consists of a 1' × 3' (30.5 cm × 91.5 cm) aluminum plate, mounted vertically on a base, with the transmitter on one side and the receiver on the other. With the mounted components, the optics package measures 31 cm wide × 46 cm deep × 97 cm tall. The figure shows that the package is very modular, so that it would be easy to change to a different telescope, detector, laser, or receiver optics box, if need be. The electronics reside in a half-size rack, which has removable lids and padding for easy transport. There is space in the rack for the future installation of the laser power supply and cooling, which currently is a stand-alone unit.

This is a relatively compact lidar system, though by no means unique in this regard. It does not require the space and weight of an optical table or breadboard. It is easy to orient horizontally or upside down, for purposes other than cloud detection, including calibration. This chapter walks through the major system components in more detail and explains the reasoning behind the design choices that were made.

Laser Source

There are many factors to consider in the choice of a laser. The first is to choose an appropriate wavelength, keeping in mind the availability at a given wavelength of high power, short pulse-length lasers. The wavelength for this lidar should be such that there is high transmission through the molecular atmosphere, strong scattering by cloud and

Figure 3. Labeled photographs of the lidar system.

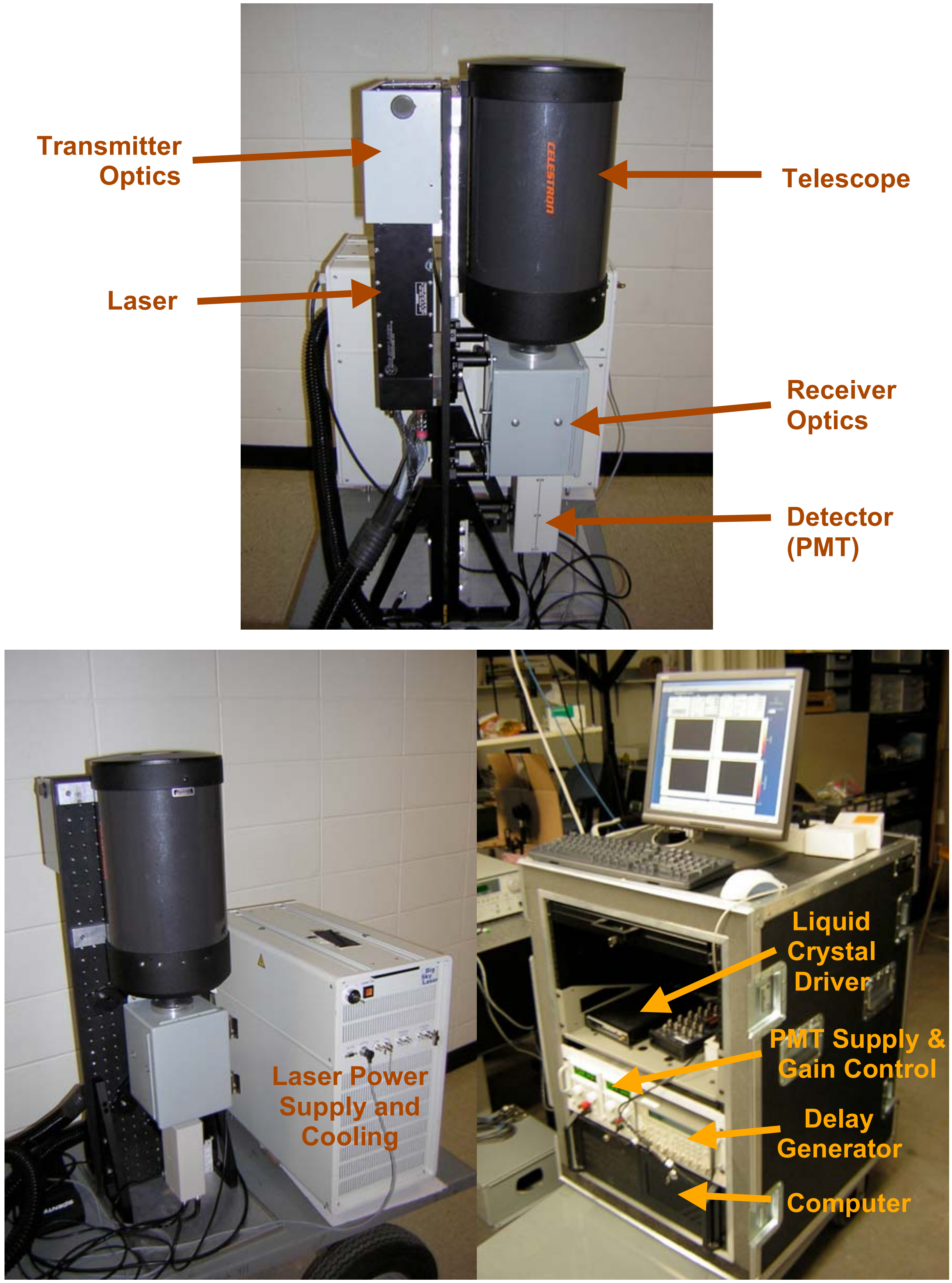

aerosol particles, low absorption by ice (in order to get enough ice crystal depolarization, which, as I noted, results from *internal* reflections), and low absorption by water (for applications like fish detection).

The chosen laser is a frequency-doubled, flashlamp-pumped Nd:YAG (532 nm). As a measure of transmission and absorption, I will compare the 1/e penetration depth at various wavelengths. For pure water, the highest transmission occurs at a wavelength of 417.5 nm, where the penetration depth is 83.2 m (Pope and Fry 1997). For 532.5 nm, the depth is 8.23 m, and for 692.5 nm (near the ruby laser wavelength) it is only 0.68 m. So 532 nm is acceptable for water transmission, but not ideal.

For ice transmission at 530 nm, the penetration depth is 6.1 m (Warren 1984), which is plenty considering the small size of ice crystals. At a wavelength of 10 μm, the penetration depth is only about 6 μm (Warren 1984). As this would suggest, CO_2 Lasers at 10.59 μm have been shown not to be useful for dual-polarization cloud lidar, and the high ice absorption only subsides for wavelengths below about 2 μm (Eberhard 1992).

The transmission through the molecular atmosphere at 532 nm is very good, with the nearest absorption line (found in the HITRAN database) being a weak water vapor line at 532.5 nm, far enough away from the doubled Nd:YAG at 532.1 nm. Cloud and aerosol particle backscatter cross sections vary widely with their size and the wavelength when the size and wavelength are comparable (Measures 1984). Generally, particles that are big compared to the wavelength scatter stronger than small particles, and so a short wavelength scatters stronger off the same ensemble of particles than a long wavelength.

Therefore, a 532 nm lidar should see certain small particles better than a 1064 nm lidar (although differences in the detectors required is probably a bigger effect).

The availability of a suitable detector at 532 nm is good (the detector is discussed in a following section). As far as eye safety is concerned, wavelengths longer than 1.5 μm are better, except that the aversion response to visible light lends some help. Appendix A includes eye safety calculations for pulsed lasers at 532 nm.

Another consideration is whether to build a micropulse lidar or not. I have noted that the main advantage of a micropulse lidar is eye safety and therefore the possibility of unattended operation. Some disadvantages are that more than one pulse is required to see anything, and a very narrow field of view is required to limit sky noise (a narrow linewidth interference filter also requires small ray incidence angles, and so the field of view is limited for a second reason). Large-energy pulses do not require averaging, and they provide enough signal to have a large field of view. Though a large field of view is not desirable for a cloud lidar, due to multiple scattering problems, it is desirable to make the lidar as versatile as possible.

The laser used for the lidar is a Big Sky Laser CFR-200. Its pulse repetition rate is 30 Hz, the pulse energy is nominally 130 mJ, and the pulse width is 10 ns. I measure the pulse shape in time in chapter 3. The far-field ($1/e^2$ power) divergence full angle is 2.16 mrad. The laser is specified with a pointing stability of 100 μrad, which is worse when the laser temperature has not yet stabilized. Figure 4 shows the laser head on the optics package with two mirrors for steering the beam into the telescope field of view.

Figure 4. Labeled photographs of the laser and transmitter optics.

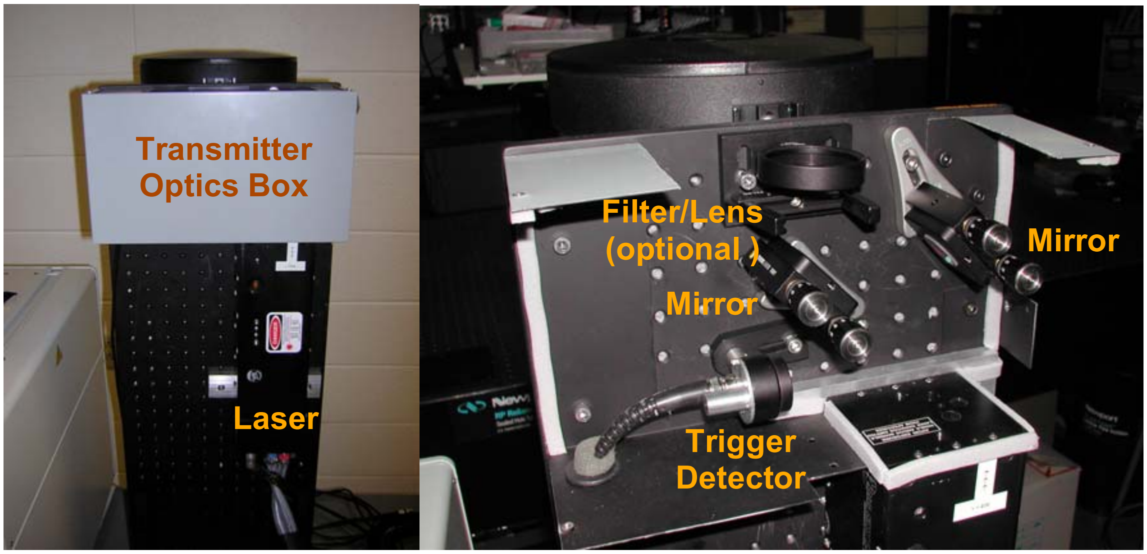

Receiver Telescope

The telescope used as a receiver is a Celestron C8-S, which is an 8" (20.3 cm) aperture Schmidt-Cassegrain design (Figure 3). For a given aperture size and F/#, Schmidt-Cassegrain telescopes are particularly compact in the long-dimension because light traverses almost the whole length of the scope three times between the primary and secondary mirrors. A disadvantage with these scopes is the central obstruction where the secondary mirror is mounted. Besides reducing the effective aperture area by 11%, this obstruction has no spatial effect on light scattered from far enough away. The telescope is 43 cm long. Its focal length is specified as 2032 mm (making it f/10), but a focus knob on the telescope makes the location of the focus variable. The opening at the rear of the telescope is 38 mm in diameter without any attachments, and it is the ultimate limit to the size of the field stop. Therefore, the maximum full-angle field of view, calculated in this case by dividing the diameter of the field stop by the focal length, is roughly 18-19 mrad.

An alternative to the telescope is a large condenser lens. A single lens as large as 150 mm in diameter can be bought off the shelf with a 450 mm focal length. (This makes it similar in length to the aforementioned telescope, but with about two-thirds the area, taking into account the central obstruction of the telescope.) The problem with this lens is that its aberrated spot size is large compared to the field stop (an external iris in this case) when the field of view (FOV) is small. For example, to get a 1 mrad FOV one would use a 0.45 mm aperture (0.001 × 450 mm) located at the focus of the lens, but Zemax ray traces of this lens show an RMS spot diameter of 0.84 mm. By way of contrast, a 1 mrad FOV with the telescope would require a field stop of about 2 mm, which is much larger than the spot size of the telescope. (A Zemax model of a similar telescope has an RMS spot diameter < 12 μm.) To determine the field of view with certainty, I would use a single condenser lens like this only for a field of view of 10 mrad or greater. A receiver of this type is used on a lidar for fish detection, which uses a field of view of 15-50 mrad (Churnside et al. 2001). Still, because the telescope seems like overkill, a doublet lens was also considered, but these get expensive quickly as they get large. Telescopes have the cost advantage of being manufactured on a larger scale.

A possible drawback from using a Schmidt-Cassegrain telescope is that depolarization could result from the reflections, making measurements of atmospheric depolarization problematic. Apparently, other dual-polarization lidar systems that use reflective telescopes don’t have this problem. However, the question has been raised, and

I am not aware of any definitive polarization measurements of reflective telescopes. I measure the polarization purity of the receiver in Chapter 3.

Receiver Ray Trace and Field of View

The light collected by the telescope, before it hits the detector, must have its field of view restricted, its spectrum filtered, and its different polarizations separated or selctively transmitted. These functions are accomplished in a light-tight box between the telescope and detector. The box opens with convenient latches and ordinary optical mounts can be installed, making it very easy to modify. The box is divided into two regions, separated by a baffle. See Figure 5 for a labeled photograph of the interior of the box. In the center of the baffle is a ½" long tube in which 1" optics can be mounted or on to which other tubes can be screwed. As shown in the figure, a laser line interference filter is screwed onto the top of the baffle. This way, the baffle serves to keep out reflected light that doesn't make it through the filter.

The field stop must be located at the telescope focus, so that the field of view is a binary function: various rays from a small object are either all passed or all blocked by the field stop, depending on the location of the object. A field lens is located shortly after the field stop to keep the beam from diverging any further and getting vignetted. After the polarization optics (which are discussed in the following section) a second lens focuses the light onto the detector. The detector has a 10 mm diameter active area, so there is no need for a tight focus. A ray trace, produced using Zemax, is shown in Figure 6. In this figure, the blue rays come from a point source on the optical axis, and the green rays come from the widest field point that is practical for the size of the optical components

Figure 5. Labeled photograph of the receiver optics inside the box.

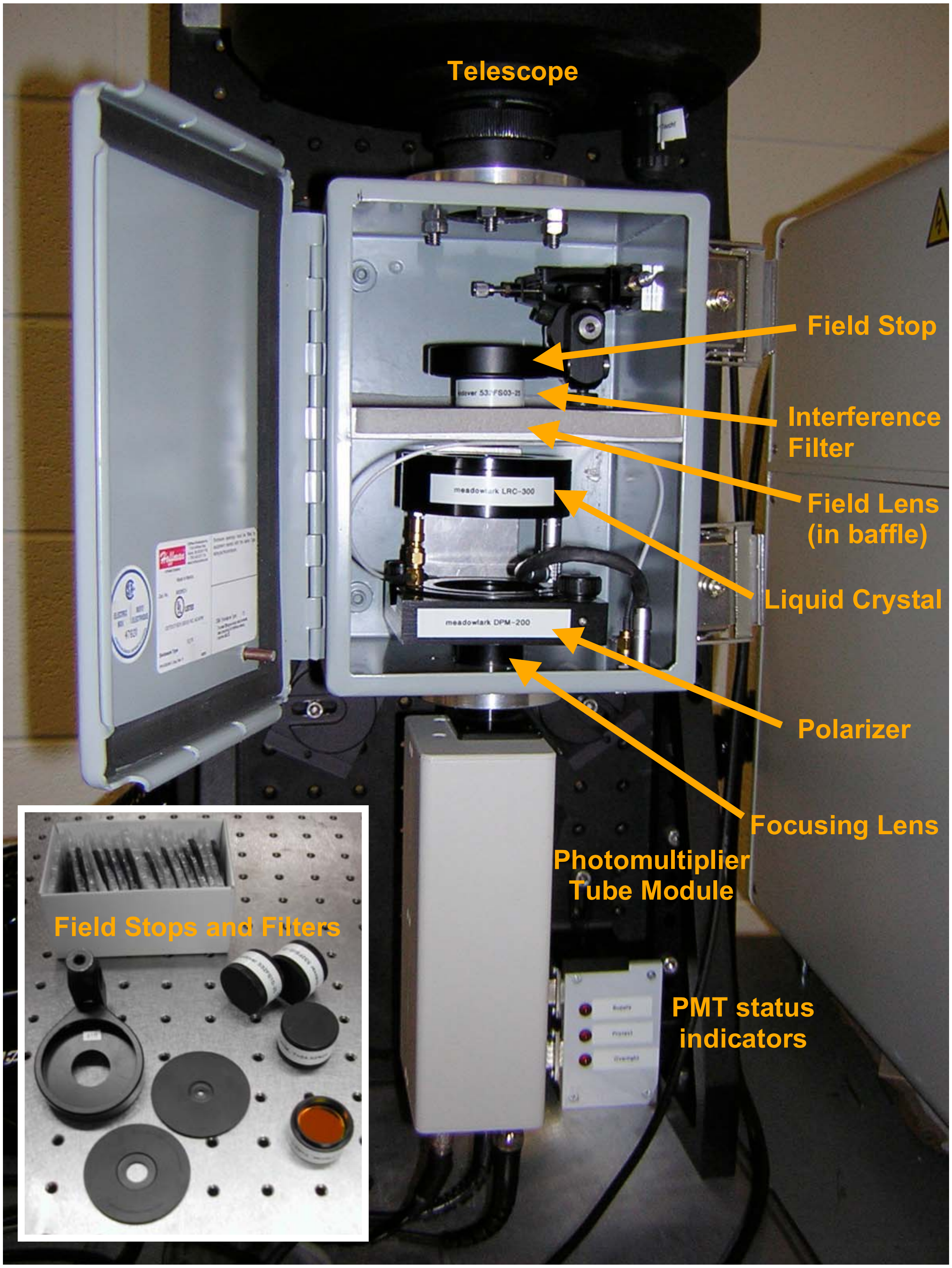

Figure 6. Optical ray trace for the receiver set at its widest field of view (produced using Zemax).

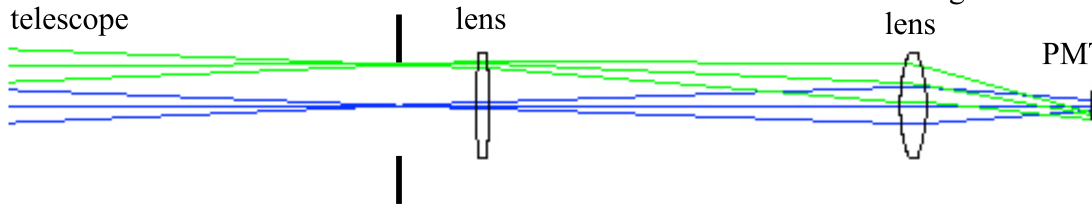

Table 1. Receiver Optical Design Data (all units are mm).

#	Type	Comment	Curvature	Thickness	Glass	Semi-Diameter	Focal Length
0	STANDARD		0.000E+00	1.000E+10		0.000E+00	
1	PARAXIAL	TELESCOPE	0.000E+00	2.282E+03		1.000E+02	2.265E+03
2	STANDARD	THOR LB1945A	4.865E-03	2.790E+00	BK7	1.270E+01	2.000E+02
3	STANDARD		-4.865E-03	9.500E+01		1.270E+01	
4	STANDARD	THOR LB1027A	2.492E-02	6.120E+00	BK7	1.270E+01	4.000E+01
5	STANDARD		-2.492E-02	3.800E+01		1.270E+01	
6	STANDARD	DETECTOR	0.000E+00	0.000E+00		3.506E+00	

(an 8.83 mrad full angle). An aperture is used as a field stop to set 8.83 mrad as the field of view, but if it were much bigger it would be limited by the laser line filter. Table 1 shows the data used for the ray trace in Figure 6. Note that the field lens is located 17 mm behind the focus. That space is required for the interference filter to be put between them. The part numbers for the 1" coated bi-convex lenses are also in the table. The clear-aperture radius through a mounted 1" optic is 11.43 mm; the ray trace shows the widest ray height is 10.84 mm at the field lens and 10.24 mm at the focusing lens. The maximum beam radius at the detector is 3.5 mm, spreading the signal over the detector active area (to avoid spatial uniformity problems) without clipping on the edges.

The telescope (not shown in the ray trace) was modeled as a perfect paraxial object with focal length of 2265 mm. The focus knob of the telescope was adjusted so that focus was at the field stop. The best way to determine the location of the focus is to point the telescope at a target that is essentially at infinity, such as distant mountains, and find their image on a card. The location of the focus can be moved from inside the telescope to at least 10 cm behind it. With the focus adjusted to be at the field stop, the field of view can be measured, with a certain field stop size, in order to infer the focal length. Measured at 100 m away, the width of the field divided by that distance is the field of view in radians. Then, the diameter of the field stop divided by the field of view equals the focal length. This focal length is measured to be 2265 mm ± 3%. Once the focal length is found, it can be used to calculate the field of view for other stop sizes. The field stops are anodized aluminum discs with 2" outer diameters and various inner diameters, and each stop is identified with a number. Table 2 gives their inner dimensions and their consequent fields of view. Note that #10, at 8.83 mrad, is the largest size that will work with the receiver optical design as it stands, with 1" optics (Figure 6).

The center wavelength of laser line interference filters shifts with incidence angle, because its effective length is longer for off-axis rays (Smith 2000, chapter 7). The worst-case incidence angles for different regions in the ray trace are given in Table 3, and Table 4 gives the calculated maximum acceptable angles for various filter linewidths. The narrower the filter, the smaller the incidence angle must be so that the laser wavelength is not blocked. These data show that I can use the narrow 1 nm FWHM filter only if I locate it in the system before the field lens, where the ray angles are the smallest. I will discuss the effect of ray angles on the polarization optics in the next section.

Table 2. Field stop aperture sizes.

Aperture #	Aperture diameter [mm]	Field of view, full angle (with 2265 mm telescope focal length) [mrad]
1	1.0	0.441
2	2.0	0.883
3	3.0	1.324
4	4.1	1.810
5	6.0	2.649
6	6.6	2.914
7	8.0	3.532
8	10.0	4.414
9	15.3	6.754
10	20.0	8.829
11	25.0	11.036
12	30.0	13.243
13	36.0	15.892

Table 3. Maximum ray angles in the receiver for the widest field of view.

	Maximum ray angle (at widest field of view, 8.83 mrad)
Prior to field lens (through interference filter)	2.78°
After field lens (through liquid crystal and polarizer)	4.97°

Table 4. Maximum acceptable ray angles for 532 nm - centered interference filters with various bandwidths.

532 nm filter, with $n_e = 2.05$, and FWHM:	Incidence angle for a center shift of 70% of the half width	Incidence angle for a center shift of 90% of the half width
1 nm	4.26°	4.84°
3 nm	7.39°	8.39°
10 nm	13.58°	15.43°

Polarization Discrimination

The most common way of building a dual-polarization lidar receiver is to use a polarizing beam splitter after the telescope and send the two polarizations to separate detectors. Some systems even use two separate telescopes (Tan and Narayanan 2004). Either way, this requires calibrating for the difference between the detectors.

Another method is to measure only one polarization at a time, but to alternate the sampled polarization quickly enough that the target is presumed not to have changed. The depolarization ratio is computed between different pulses, or between different sets of pulses. The advantage is that it is simpler to use one detector and telescope. The disadvantage is a loss of time resolution (because there are fewer useful pulses – not a loss of sampling resolution for a given pulse).

The alternating-pulse method has been implemented in NOAA's Depolarization And Backscatter Unattended Lidar, DABUL, using a Pockel cell (Intrieri et al. 2002). A Pockel cell is an electro-optic device in which the index of refraction depends on the applied voltage. The indices along the two axes perpendicular to the propagating light can be varied differently, introducing a relative retardance between the two linear polarizations. The applied voltage can be tuned to achieve a 90° rotation of the incident polarization. If the cell is followed by a polarizer, together they act to pass one linear polarization or the orthogonal linear polarization, depending on the applied voltage (which is usually kilovolts). Pockel cells switch quickly, on the order of 1 ns, but they are long and have small apertures, which can be a difficulty for some optical designs.

A similar method is to use a liquid crystal instead of a Pockel cell. A twisted nematic liquid crystal has long molecules that are locally oriented parallel to each other (like a crystal) but their positions are random (like a liquid). The front and back of the crystal is bounded by two plates of glass that are polished in opposite directions. The crystal molecules on the ends line up with the polishing, and those in the middle are oriented to various degrees in between the two – hence, the name "twisted" (Saleh and Teich, chapters 6 and 18). Like a Pockel cell, a liquid crystal can rotate the incident polarization. Compared to Pockel cells, liquid crystals are slow (10s of ms switching times), but they can be thinner and only require a few volts. An applied voltage between the front and back of the crystal makes some of the center molecules orient themselves in the axis of propagation, so that they do not affect the polarization of the light. In this way, the voltage can be tuned to achieve a half-wave retardance between the two transverse axes for a particular wavelength. It cannot be tuned to zero retardance unless it is combined with a fixed wave plate that acts as a compensator. With a compensator, the device ideally acts like a half-wave plate that can be switched on and off.

I also tested a ferroelectric liquid crystal, which only has two stable orientations for the molecules, so it only provides switching between two retardance values for a given wavelength. The advantage here is that the devices are thinner and faster than other liquid crystals. But since the retardance was not exactly right, and it was not tunable with voltage, the measured depolarization ratio error was worse than 3%.

The chosen device is a twisted nematic liquid crystal variable retarder from Meadowlark Optics (Figure 5). It has a 1.6" clear aperture, and it is temperature-controlled (which is important to keep a uniform retardance). It allows continuous tuning of the retardance with voltage, and an integrated compensator allows tuning down to zero retardance and slightly beyond.

The Micro Pulse Lidar system, MPL (Campbell et al. 2002), is the only known instance of a liquid crystal being used for lidar. The dual-polarization version of the system is still in development at Pacific Northwest National Laboratory for the DOE's Atmospheric Radiation Measurement (ARM) Program, using the very same model liquid crystal device (Flynn 2005).

I will now show mathematically how the liquid crystal and polarizer combination discriminates between different linear polarizations. Afterward, I will explore the behavior of the liquid crystal for light that is incident at oblique angles. The polarization state of incoherent light can be described with a Stokes vector, and the effect on that polarization state by a system component can be described with a Mueller matrix. Briefly, the four elements of a Stokes vector correspond to the overall power of the light, the amount of horizontal or vertical linearly polarized light, the amount of ±45° linearly polarized light, and the amount of right- and left-handed circularly polarized light, in that order. The potential for minus signs on the latter three terms provides all the necessary degrees of freedom. For example, with the amplitude normalized to one, vertically polarized light has a Stokes vector

$$S_{vertical} = \begin{bmatrix} 1 \\ -1 \\ 0 \\ 0 \end{bmatrix}, \tag{2.1}$$

whereas horizontal light has a positive second element. If vertical light is transmitted by the laser and is depolarized by some target, we need a matrix to describe depolarization, a scrambling, to some extent, of the polarization states. An ideal depolarizer is described by the Mueller matrix

$$M_{depolarizer} = \begin{bmatrix} 1 & 0 & 0 & 0 \\ 0 & a & 0 & 0 \\ 0 & 0 & a & 0 \\ 0 & 0 & 0 & a \end{bmatrix} \tag{2.2}$$

(Chipman 1999), where $a = 1$ for no depolarization and $a = 0$ for complete depolarization (yielding a depolarization ratio of 1). The light is then received by the telescope and is incident on the polarization optics. As noted before, the liquid crystal, at its most basic level, is a half-wave plate that can be switched on and off. For a half-wave plate oriented with the fast and slow axes 45° off vertical, and for a vertical linear polarizer, the ideal Mueller matrices are

$$M_{half-waveplate\ at\ 45^\circ} = \begin{bmatrix} 1 & 0 & 0 & 0 \\ 0 & -1 & 0 & 0 \\ 0 & 0 & 1 & 0 \\ 0 & 0 & 0 & -1 \end{bmatrix} \tag{2.3}$$

and

$$M_{vertical\ polarizer} = \begin{bmatrix} 0.5 & -0.5 & 0 & 0 \\ -0.5 & 0.5 & 0 & 0 \\ 0 & 0 & 0 & 0 \\ 0 & 0 & 0 & 0 \end{bmatrix}. \tag{2.4}$$

These matrices are applied in the order that they act on the signal, and the power incident on the detector is the first element in the resulting Stokes vector.

$$\begin{aligned} S_{cross-pol\ signal} &= M_{vertical\ polarizer} M_{half-waveplate\ at\ 45^\circ} M_{depolarizer} S_{vertical} \\ S_{co-pol\ signal} &= M_{vertical\ polarizer} M_{depolarizer} S_{vertical} \end{aligned} \tag{2.5}$$

The co-pol signal is measured with the liquid crystal set to zero retardance (an identity matrix that is omitted in Equation 2.5). Figure 7 shows the ideal normalized co-polarized and cross-polarized signals as a function of the depolarization coefficient *a*. As expected, it shows the two signals are the same for *a* = 0, and the cross-polarized signal is 0 for *a* = 1. The depolarization ratio is also plotted to show that it is *not* as simple as 1-*a*.

Figure 7. Ideal normalized depolarization signals measured by a variable retarder and polarizer (computed with Mueller calculus).

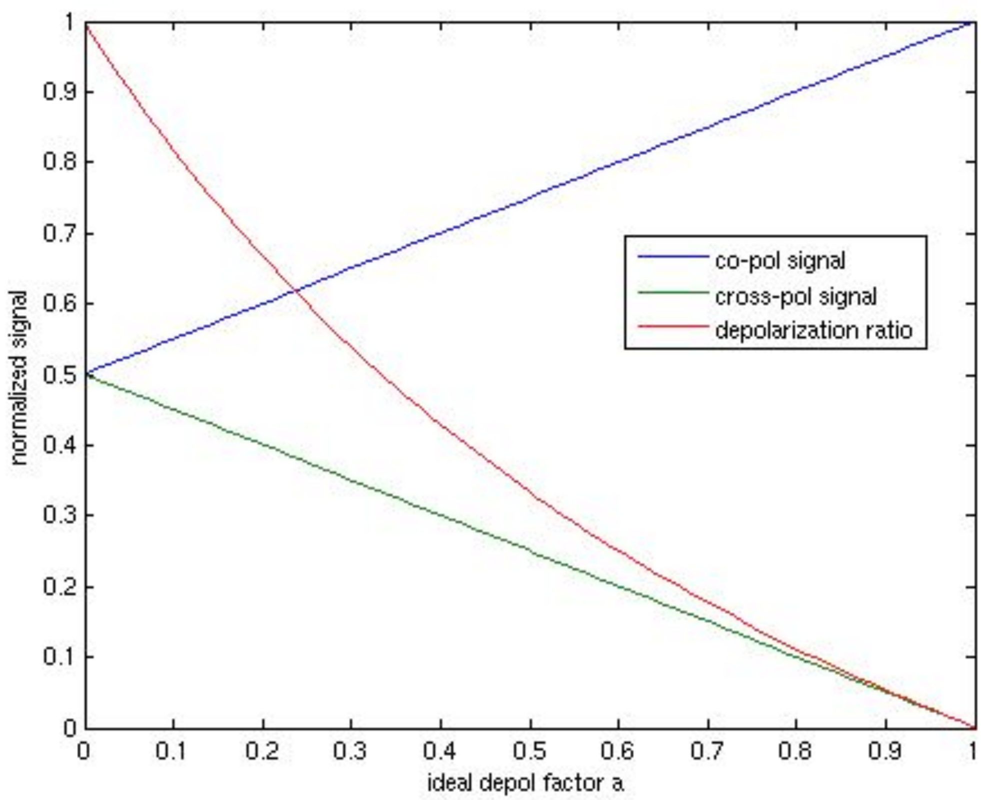

Rather than continuing to represent the liquid crystal with the Mueller matrix of a waveplate, a matrix can be written which shows the dependence on the physical orientation of the device's slow axis θ (assumed above to be 45°), and the relative retardance between the two axes δ (assumed above to be π radians). Xiao et al. (2003) give the Mueller matrix:

$$M_{LC} = \begin{bmatrix} 1 & 0 & 0 & 0 \\ 0 & \cos^2 2\theta + \cos\delta \sin^2 2\theta & (1-\cos\delta)\sin 2\theta \cos 2\theta & -\sin\delta \sin 2\theta \\ 0 & (1-\cos\delta)\sin 2\theta \cos 2\theta & \sin^2 2\theta + \cos\delta \cos^2 2\theta & \sin\delta \cos 2\theta \\ 0 & \sin\delta \sin 2\theta & -\sin\delta \cos 2\theta & \cos\delta \end{bmatrix}. \tag{2.6}$$

This matrix has a hidden dependence on the incidence angle of the light. This is because both the effective axis angle θ and the retardance δ depend on the relative angle between the internal light ray and the molecular axis. The molecular axis depends on the applied voltage (as well as material constants and the wavelength).

The worst case will be when the liquid crystal is set to half-wave retardance, because that is the setting for the cross-polarized signal, which is often small and is more sensitive to errors. Table 3 lists the maximum ray angle incident on the liquid crystal as less than 5°. Xiao et al. (2003) showed that for similar conditions (a liquid crystal oriented at 45° and set near a half-wave retardance), external incidence angles of 5° cause the half-wave retardance to vary by about 0.08λ and cause the 45° rotation angle to effectively vary by about 2°. With both of these errors at their worst, I evaluate the Mueller matrix:

$$M = \begin{bmatrix} 1 & 0 & 0 & 0 \\ 0 & -0.959 & -0.137 & 0.248 \\ 0 & -0.137 & 0.990 & 0.0174 \\ 0 & -0.248 & -0.0174 & -0.969 \end{bmatrix}. \tag{2.7}$$

Compare this to the ideal half-wave plate (Equation 2.3). Using it in the previous calculations shows that the error in θ alone causes 1.6% of the co-pol light to leak into the cross-pol measurement, whereas the error in δ causes 0.5% leakage. For the worst case combined, the cross-pol signal (with no target depolarization) is 2.0%.

Only a small fraction of the light is likely to have a 5° incidence angle. To predict this, it is not as simple as integrating over all accepted incidence angles, since that ignores the location of the beam within the field, which varies with range (see the overlap calculation in chapter 3.) Suffice it to say that no measurement should have the full 2% error from this source. But this problem is another reason to prefer narrower fields.

A last design consideration related to the liquid crystal is the switching speed. The speed is quicker at higher temperatures and at higher voltages. It is also quicker for the transition to a higher voltage (to less retardance) because the opposite transition relies on the relaxation to the natural state of the crystal. A common strategy is to overshoot the desired voltage for a short time in order to speed up the transistion. This is called the Transient Nematic Effect (Meadowlark Optics Application Note, 2003). I operate the device at 40 °C, and at this temperature, the voltages for half-wave and zero retardances at 532 nm are found to be 2.055 V and 4.950 V, respectively. The waveform is actually a 2 kHz squarewave that is 0 VDC (to keep charge from building up on the crystal), but the driver insulates the user from having to worry about that. The waveform is programmed to switch between 2.055 V and 4.950 V, but the first 5 ms for each transition are overshot to 10 V and 0 V. This general shape is called a T. N. E. waveform, and 5 ms was found to be the best length for these spikes in order to accelerate the transitions well and still give it time to stabilize afterwards. Table 5 gives the response times that were found with this waveform. The times are good enough to allow switching between 30 Hz laser pulses, a 33 ms period, if the device is switched soon after the laser pulse.

Table 5. Liquid crystal switching times for 532 nm, with the liquid crystal at 40 °C and using a 5 ms, 0-10 V transient nematic effect drive waveform.

	10%-90% switching time	~100% switching time
zero to half-wave (to 2.055 V)	8.2 ms	22 ms
half-wave to zero (to 4.950 V)	5.2 ms	9 ms

Photomultiplier Tube Detector

Photomultiplier tubes (PMTs) are most often used as the detectors for lidar systems operating at wavelengths of 200-900 nm. In this region, compared to silicon detectors, PMTs generally have lower noise, higher gain, larger active area and faster response (Burle Technologies, 1980). A photomultiplier consists of a cathode and an anode with about 10 dynodes in between. A photon incident on the cathode can free an electron from its surface (with a quantum efficiency of about 10%). A large voltage accelerates the electrons, and at each dynode stage more electrons are produced. The signal is measured as a current drawn by the anode.

The main difficulty with PMTs is instability at high light levels. The signal is not merely clipped at some saturation level; instead, too much light affects the shape of the signal by reducing the amount of electrons available to multiply photoelectrons arriving at a later time. Since the gain is variable with the power supply voltage, the linearity and saturation characteristics are best correlated to the PMT signal current, not to the signal optical power. For example, a low light level may saturate a PMT at a high gain because the signal current is the same as if it were a high light level with low gain.

A 1 nm FWHM spectral filter helps limit the background skylight on the detector. Another way to limit the background is to gate the detector on only when lidar signals are expected to return. For cloud lidar, I am interested in altitudes of up to 15 km. Light travels to this altitude and back in 100 μs. I use 120 μs long gates, and with 30 laser pulses per second, the PMT has just a 0.36% duty cycle. This keeps the constant background between pulses from affecting the signal during a sampling period.

The Hamamatsu H7680-01 is a PMT module which includes the high voltage power supply and gating circuitry. The peak in the responsivity occurs at 420 nm, and at 532 nm the responsivity is about 57% of the peak. The total responsivity (the responsivity at the anode) is the cathode responsivity times the gain. The cathode responsivity is about 50 mA/W at 532 nm, and the gain is variable from $10^3 – 10^7$ with a control voltage between 2 and 5 V. I will calibrate the anode responsivity at a number of gain control voltages in chapter 3.

Also important are the PMT's characteristics in time. Electrons have a transit time through the tube, specified for this tube at 16 ns for a gain control voltage of 4.5 V. This time is dependent on the gain, and it affects the absolute accuracy of range measurements, but it can be calibrated for. A potentially worse problem is the transit time spread, which describes how a delta function of light into the PMT is spread into a signal current over some time, and fortunately it is specified at only 500 ps. And finally, the rise time is specified at 1.7 ns, which is satisfactory because it is no longer than the rise time of the laser pulse itself.

Signal Acquisition

Lidar signals have a large dynamic range due both to their inverse range-squared dependence (Equation 1.4) and the wide contrast between scattering from very thin features or thick, bright clouds. When it comes to digitizing the signal, there is a hardware trade-off between high dynamic range and fast sampling rates. A fast sampling rate allows a high spatial resolution if the laser pulse length is also short. For applications that simply measure the range to a hard target far from the instrument (like laser altimetry), less dynamic range is required and it is traded for extremely high spatial resolution. While high spatial resolution is not needed for clouds, both high dynamic range and fast sampling are desired, of course, to keep the instrument as versatile as possible. This section discusses strategies to compress the dynamic range of the signal, and then it fleshes out the consequences of the sampling rate on the range resolution.

Methods to reduce the dynamic range of the signal before it is digitized include switching the gain on the detector, while sampling, based on the signal level (Spinhirne and Reagan 1976). The signals at different gains are pieced back together, one after another, with small gaps. Another method is to vary an optical attenuator over time, before the detector, in a repeatable way (Lehmann et al. 1997). NOAA's fish lidar, which requires a fast sampling rate, compresses the dynamic range with a logarithmic amplifier after the detector (Churnside et al. 2001). This works with a sufficiently wide bandwidth amplifier, but is not exactly logarithmic, so it introduces artificial features in the data that must be calibrated out. An attempt was also made to use two fast A/D converters, each with just an 8-bit dynamic range, but at different ranges (Wilson 2003). As always, piecing the two signals together is the tricky part. Other systems use multiple laser beams with different overlap functions for a single receiver. The two overlap functions combine to provide a response that still varies widely with range, but not over as many orders of magnitude (Zhao et al. 1992). Finally, if the signal near the instrument can be ignored, then it helps to delay the detector turn-on time until the bright near-field is small enough to fit in the desired A/D range.

In general, the A/D range, which is usually software programmable, should be reduced until the signal fills most of the range. This resolves the signal with the greatest number of bits possible. Some A/D cards allow a DC offset of the range, and in this case the range should be biased strongly toward the negative voltages, ranging up to just slightly above zero. (The signal from the PMT is negative.)

The A/D converter for this lidar is a Gage 14100 PCI Card. It has a 14-bit dynamic range and its speed is 100 MSample/sec. It has no DC offset for the range, so one bit is effectively wasted. The effective number of bits is also reduced by random amplitude noise and phase distortion (differential phase offsetting of the signal harmonics). The specified signal-to-noise ratio is 63 dB for 1 MHz signals, for a 10.2 effective number of bits; it depends on signal input frequency and amplitude (Girard, Signatec Application Note AN95091). There are also DC errors caused by the low-pass filter that comes before the digitizer. When the maximum range is set to ±500 mV or above, the DC accuracy is 0.5% (it is worse at smaller ranges).

The A/D card is triggered by a Stanford Research Systems DG535 Digital Delay Generator, which also simultaneously sent a gate pulse to the PMT. (The delay generator itself is triggered by a photo-diode that detects flashes from the laser pulses near the transmitter optics.) Upon an external trigger, the A/D card is set to take slightly more than 10^4 samples at 100 MS/s, which corresponds to the 100 μs window in which the PMT is on and lidar returns are expected. After the A/D card samples the signal from one lidar pulse, its buffer is read into the computer's RAM. I will return to the subject of the computer software and the data files shortly.

Range Resolution

If the target is "hard," meaning that it only scatters light at one range, then the lidar return pulse shape is the same as the transmitted pulse shape. The range can be determined as finely as the sampling allows the detection of the front edge of that return pulse. If the sampling period is T_s, and the distance light travels between samples is cT_s, then the range resolution is half that,

$$\Delta R_{hard\ target} = \frac{cT_s}{2}, \tag{2.8}$$

since the range is a distance out and back. For the hard-target case, the range resolution is just the uncertainty due to sampling.

"Soft" targets, such as aerosols or even thick clouds, do not have such high extinction, so their backscatter is a distributed function of range. In my discussion of the lidar equation, I noted that a single sample measures light that could have been scattered from multiple ranges. Since the laser pulse duration FWHM τ_0 is 10 ns (about 3 m long in space), the range being instantaneouly sampled is 1.5 m deep. This pulse-length uncertainty also contributes to the total range resolution of the lidar. Therefore, the range resolution for soft targets is either limited by the sampling uncertainty or the pulse-length uncertainty, whichever is worse.

$$\Delta R_{soft\ target} = \text{the greater of } \frac{cT_s}{2} \text{ or } \frac{c\tau_0}{2}. \qquad (2.9)$$

With a 100 MS/s sampling rate (a 10 ns sampling period) and a 10 ns laser pulse duration, the range resolution is simultaneously limited to 1.5 m by both effects.

If the sampling rate was increased to 1 GHz, the range resolution would be dominated by the pulse-length uncertainty, and it would not be better than 1.5 m. In cases like this, where the pulse-length uncertainty is long compared to the sampling uncertainty, the pulse shape can be deconvolved from the data if you measure the pulse shape in time and make some boundary assumptions.

Another factor affecting range resolution is the bandwidth of the A/D card. It is limited to 50 MHz (so that the sampling rate is at or above the Nyquist frequency for all signals that are passed). This may also limit the range resolution to 3 m, depending on the signal.

Control Software

The instrument control and data handling software is programmed in LabVIEW, operating on a Windows operating system. The data are post-processed in MATLAB. LabVIEW was chosen because of its ease of communication with instruments, while MATLAB was the most familiar analysis tool, and lends itself well to array operations. See Appendices B and C for more details on the LabVIEW and MATLAB routines. Figure 8 is a picture of the front panel of the control software in operation.

An operating system that is not real-time, like Windows, presents challenges for time-critical tasks, such as reading the data and switching the liquid crystal between laser pulses. It is valuable to be able to view the signal levels and the depolarization while operating the lidar so that settings can be optimized, but care is taken to avoid disturbing the critical tasks with processing that could be done later. The known instances of LabVIEW lidar software either post-process the data (Tan and Narayanan 2004) or use multiple computers for different control tasks (Weibring et al. 2003).

Figure 8. Front panel of the LabVIEW control software in operation.

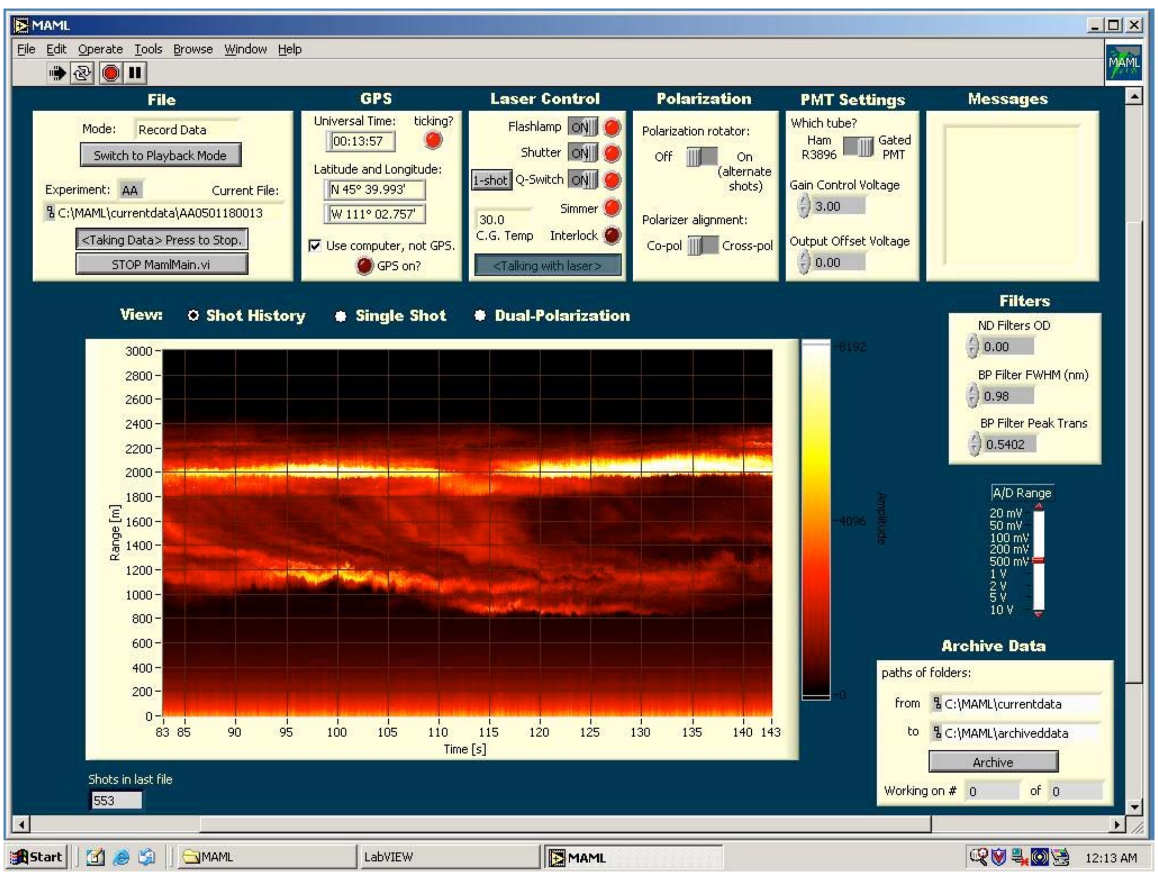

CHAPTER 3

CHARACTERIZATION

Data

Data Format

After each laser shot, data from the A/D buffer are read into the computer's memory. After each minute, the data are saved in datalog format by LabVIEW. (Datalog is the binary format preferred in LabVIEW for appending the newest data to an existing array.) At the end of a lidar data session, each datalog (.dat) file is read and saved as a MATLAB (.mat) file by LabVIEW, which is smaller and is prepared for MATLAB post-processing routines.

The 14-bit data (integers between -8191 and 8192) are treated as 16-bit (single precision) integers. There are 10112 samples taken for each shot, but the saved sequence has 10200 elements. Some of the extra 88 elements are used to save system settings such as the UTC time, liquid crystal state, PMT Gain, A/D Range, time between shots, and even the optical configuration. All of this information must be encoded in an integer format (see Appendix B). Since there are approximately 1800 shots in each minute (at 30 Hz), the file format is an array 10200 × 1800, but the second dimension is not exact. Typically, ~10 shots are missed per minute for unknown reasons (and more are missed if the computer is kept busy with other tasks), and also a file may be smaller if the session was started or stopped in that period. Datalog files are 32-bit, so the minute-long files are about 72 MB each, but the MATLAB files are 16-bit, so the files are about 36 MB each.

Datalog files are deleted when they are later archived into MATLAB files. If saving a datalog file is bypassed altogether, and instead a MATLAB file is saved every minute, too much processor time is required for new data to be read in a timely manner.

As it is, with the datalog files automatically deleted, the data rate is 2.16 GB/hour. To reduce this for long term cloud applications, some averaging should probably be done as the data are taken (on the A/D card or on a separate computer). Averaging can either be over multiple shots, or else over multiple samples of the same shot, usually with decreasing vertical resolution for higher altitudes where the signal is small. For applications such as fish lidar, the full temporal and spatial resolution is desired, but the number of samples could be reduced because the maximum range is less.

Interpreting Sample Data

Certain data processing steps are required before the data are useful for inferring cloud properties. For each file, the co-pol and cross-pol shots are compiled into separate arrays. They are distinguished based on the encoded liquid crystal state in the footer of the data. If the number of shots of co-pol and cross-pol data are not the same, some shots are discarded.

To reduce noise, a few different methods are employed. In what follows, the "horizontal" dimension refers to shot-to-shot comparisons, and "vertical" refers to sample-to-sample comparisons. (Therefore, "vertical" also refers to vertical range, but "horizontal" only corresponds to horizontal distance to the extent that spatial properties of clouds corresponds to temporal properties of the clouds in the lidar beam). A horizontal 3-point median filter is run across the whole minute-long data file, which allows single-pixel extreme value to be filtered out. Occasionally, a shot appears as if the liquid crystal failed to switch (a column in the array with values unlike those on each side). The purpose of a horizontal median filter is to remove this, as well as random noise. A one-second-wide median filter (15-points, for each polarization) is an option, as well as turning the whole file into a single-shot equivalent by taking the median of all shots, for each sample. In cases where you don't need more time resolution, this is a nice way of reducing the data volume and getting a clean signal. A median filter takes more time than simple averaging, but it is better since it is less affected by the extreme values. A vertical 3-point filter is an option, but it shouldn't be used for hard target scattering, since it could skip over the entire signal.

Next, sky noise, which is constant in the sampling dimension, is removed. It cannot be assumed constant over the entire file, especially during the daytime. This is illustrated in Figure 9, which shows a minute of data from 7 March 2005, 22:42 UTC, with two cloud layers. Figures 9A and 9B are the co-pol signal and the depolarization ratio, respectively. The co-pol signal doesn't obviously have varying sky noise, but the depolarization ratio is very dependent on small cross-pol values. To get the ratio right, the noise level (in data numbers) must be subtracted from the co-pol and cross-pol signals first. The offsets will be different for the two polarizations, and, as illustrated by Figure 9B, they can vary on the order of seconds. I compute the offset for each shot with the assumption that there is no signal between 14-15 km, and taking the median of all samples in that region. This is a safe assumption for this particular application, with gain levels such as they are, though it is thought possible to gate out more of the signal near the lidar, turn up the gain, extend the sampling range and see an aerosol layer this high.

Figure 9. The effect of the changing sky noise on the depolarization, and its correction.

A.)

B.)

C.)

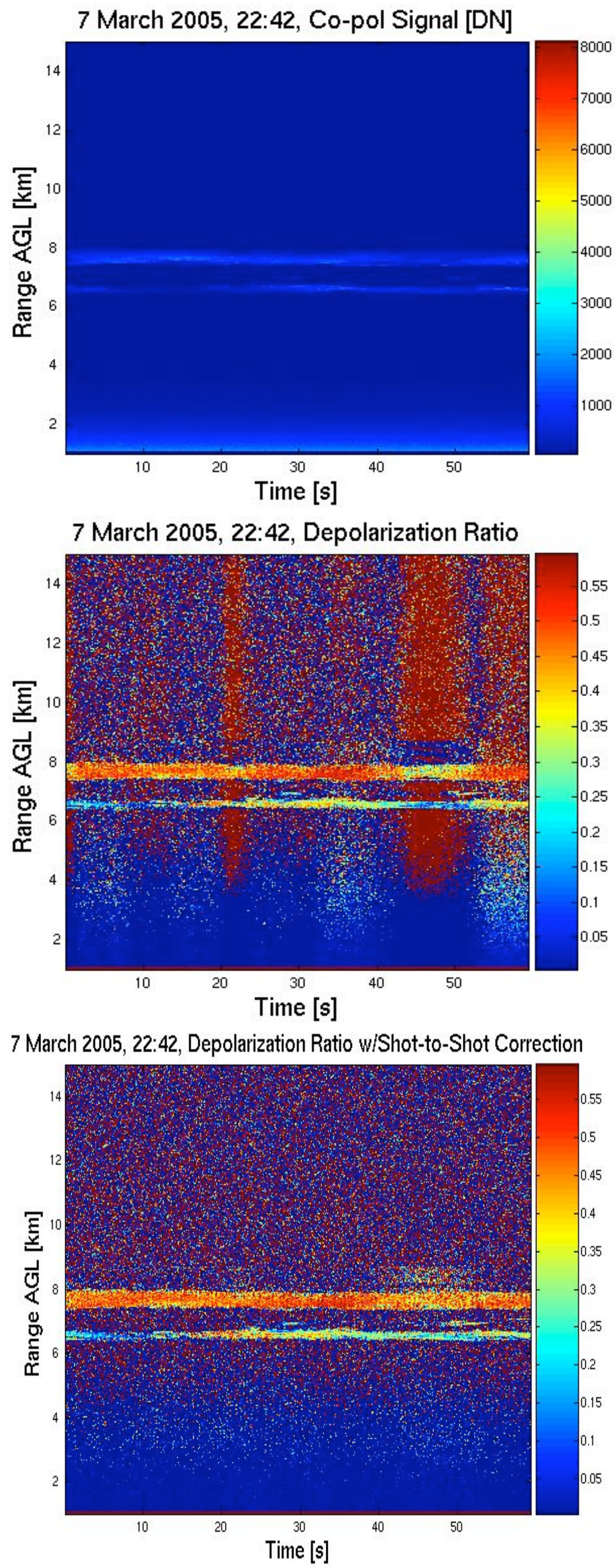

Figure 9C shows the depolarization array resulting from subtracting this offset from each shot before taking the ratio.

The data are range corrected (to be proportional to the backscattering cross section volume density, using Equation 1.5) by multiplying by the range, in km, squared. The only reason to use kilometers instead of meters is to make the numbers smaller, but it will need to be converted to meters-squared for use in the lidar equation. This correction has the effect of flattening the near field significantly, and enhancing the resolution at high altitudes. Figure 10 shows a one-second median co-pol lidar profile from 8 March 2005, 02:22 UTC. The large signal at near range is the result of the $1/R^2$ signal dependence, as well as the high aerosol density in the lower atmosphere. The signal between 7 and 9 km above ground level (AGL) is from clouds. Figure 10 also shows the range-corrected version of this signal. The near-field signal is not completely removed, showing that it is not completely attributable to the $1/R^2$ dependence. The ranges used to correct each sample are given in the range calibration section (Equation 3.4).

Finally, a depolarization ratio array is computed, dividing the cross-pol by the co-pol arrays, element by element. Figure 11 shows the co-pol and cross-pol arrays for the minute of data that includes the profiles from Figure 10. Notice that the clouds show up in the cross-pol channel as a somewhat reduced signal, but the near-field scattering in the cross-pol channel is so faint as to be invisible. In the resulting depolarization ratio array there are many positive and negative infinities, since we have already zeroed the noise levels. Because of this, the depolarization array must be displayed on a scale that shows the interesting values, between 0 and 0.6. When the signals fall into the noise, the displayed depolarization randomly varies between the extremes.

Figure 10. One second of data from 8 March 2005, 02:22 UTC, illustrating the range correction.

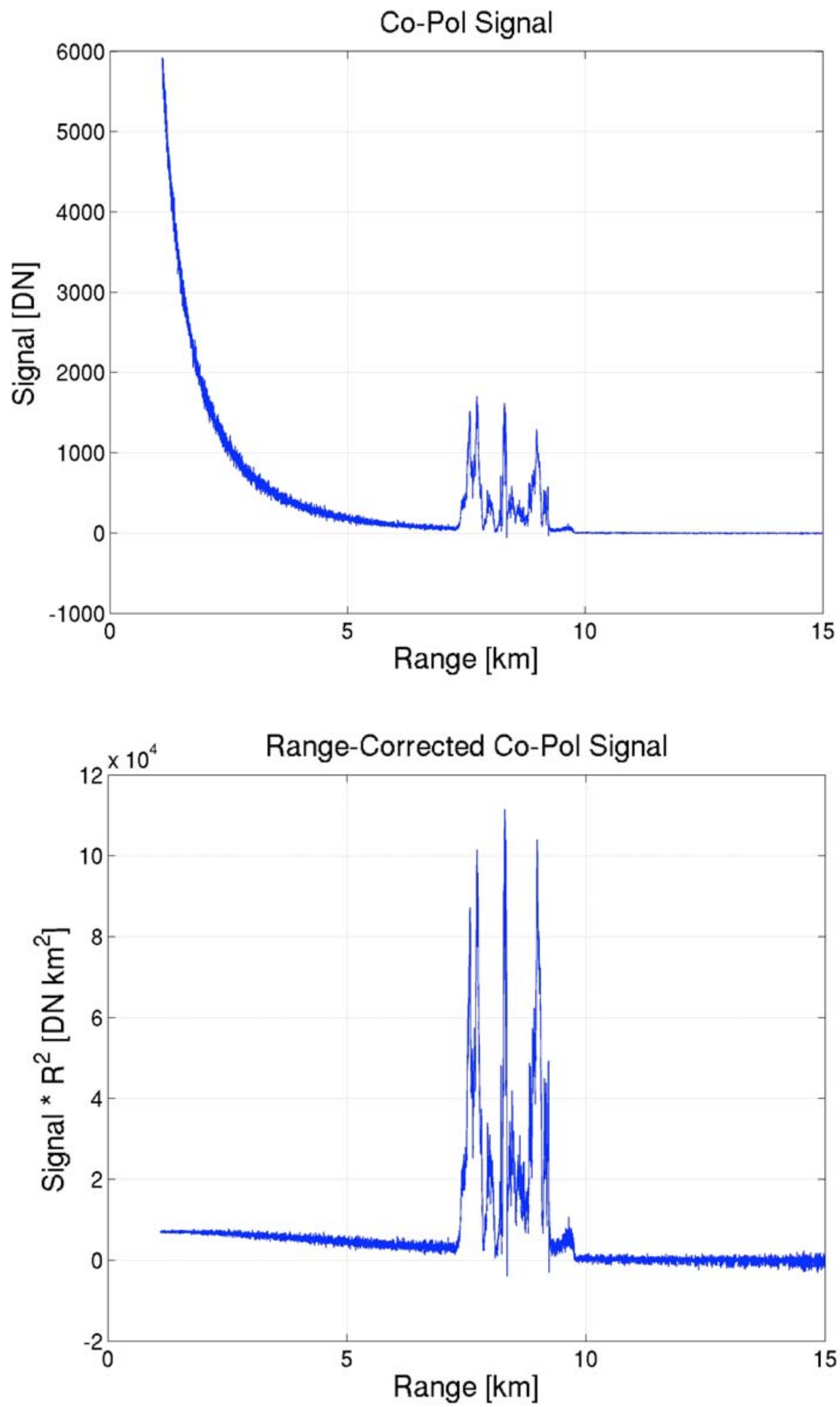

Figure 11. Co-pol and cross-pol data for 8 March 2005, 02:22 UTC.

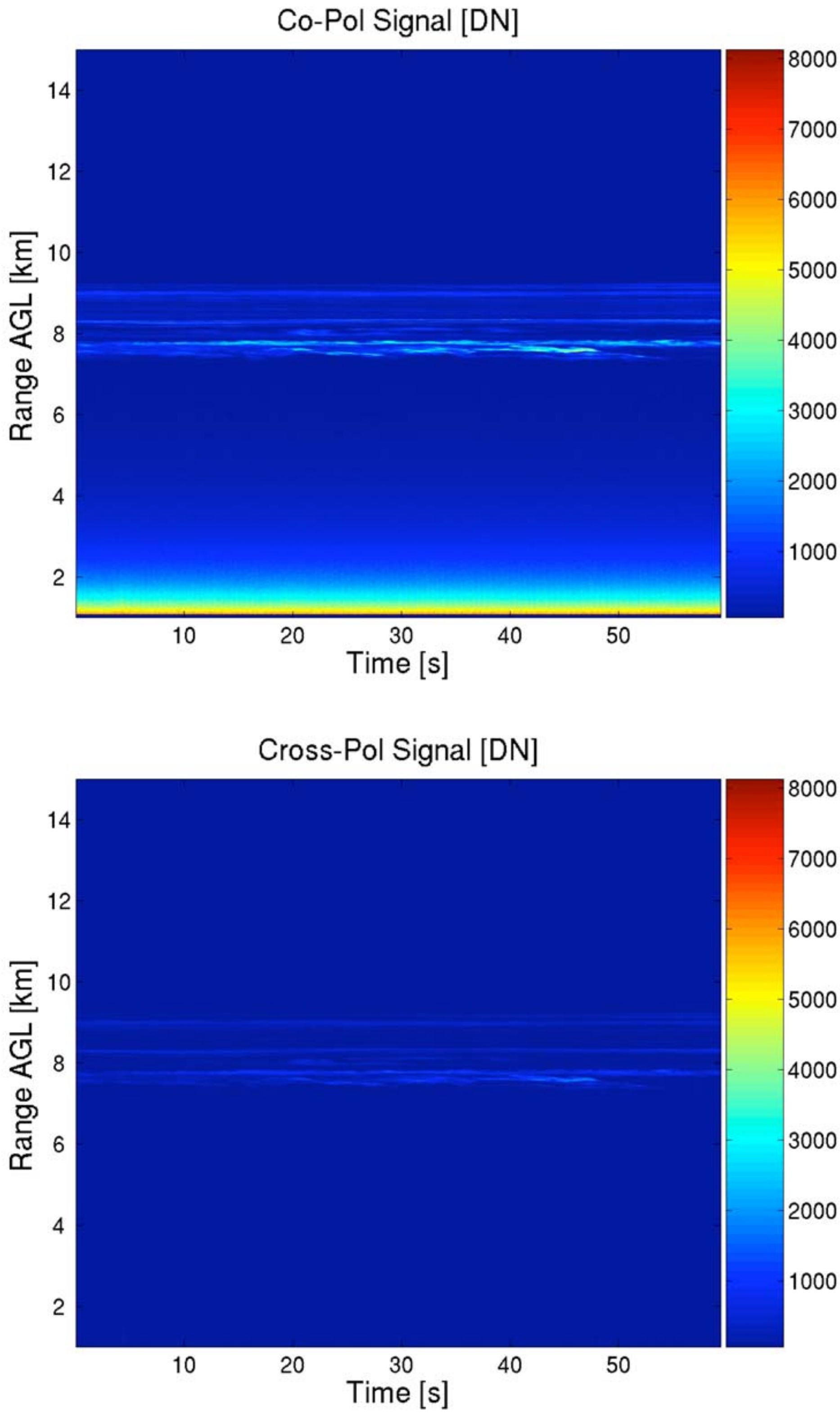

For some of the steps described so far, the order they are applied matters. The separation of polarizations must always come first. The offset should come before the range correction and the depolarization computation, but the depolarization is independent of any range correction so it could come first.

Next, I will quantify measured depolarization ratios and give physical interpretations of the data. For each case, the most useful way of viewing the data is with the combination of the range-corrected co-pol array (for backscattering intensity) and the depolarization ratio array.

Comparison with Radiosonde Profiles

For physical interpretation of depolarization ratios, a temperature profile is very helpful. On four days of lidar operation in early March 2005, weather balloons with radiosonde sensors were launched from our location on the roof of Cobleigh Hall on Montana State University, Bozeman. (On three of these days, a cloud imager was also operated, but I will address it after presenting the lidar data.)

Figures 12 and 13 show the temperature and dewpoint for March 1, 3, 8, and 10. Where the dewpoint approaches the temperature, the relative humidity is high. However, the presence of clouds is not simply determined by the relative humidity. The absolute water vapor content from radiosonde data can be integrated to give an equivalent liquid water vapor column in centimeters. The figures are labeled with the measured water vapor column. Water vapor doesn’t scatter nearly as strongly as cloud droplets at this wavelength, and it is measured not so much for the benefit of the lidar as for correcting data from the Infrared Cloud Imager, which sees both clouds and water vapor.

Figure 12. Radiosonde temperature and dewpoint profiles on 1 and 3 March 2005.

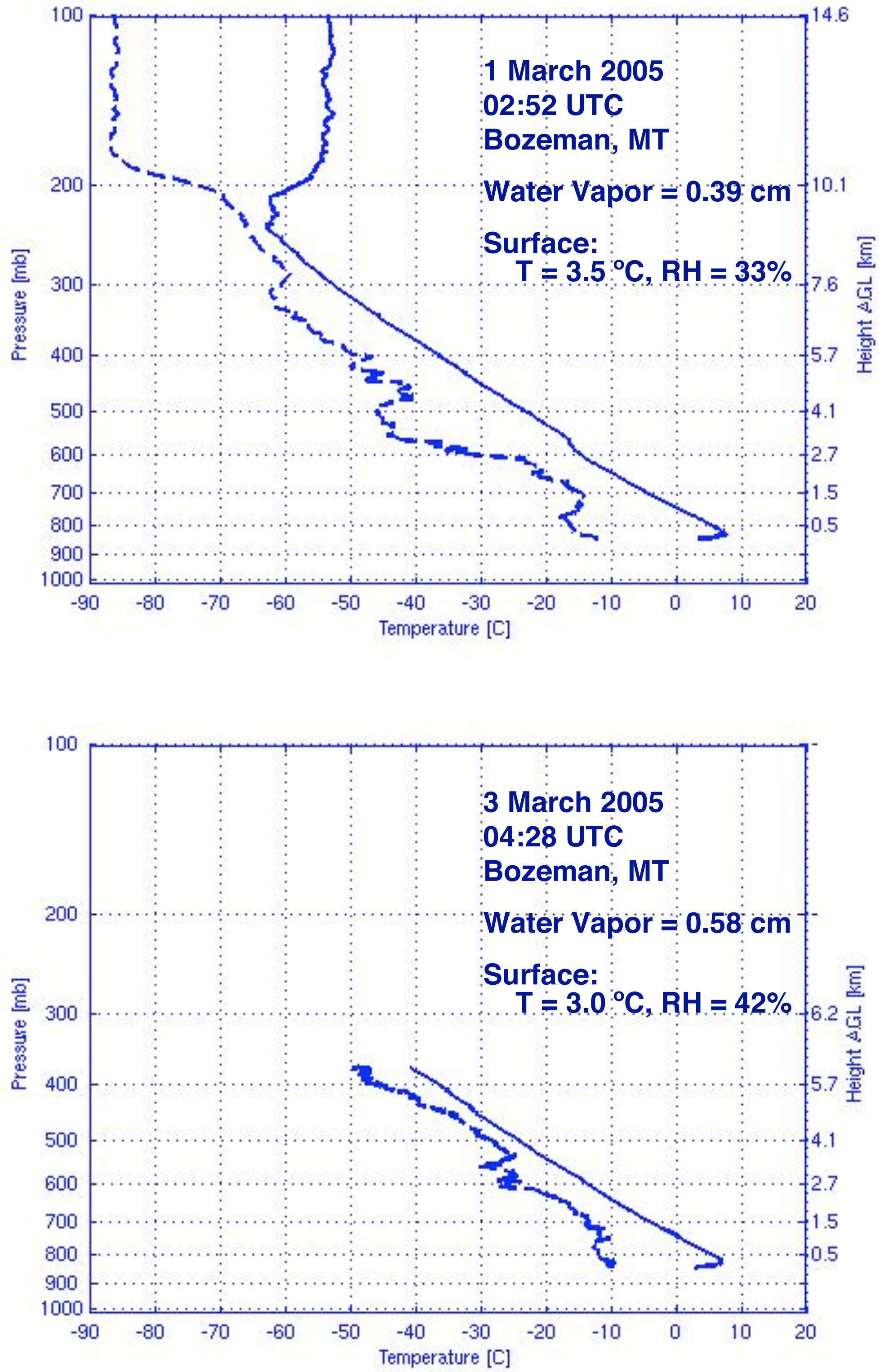

Figure 13. Radiosonde temperature and dewpoint profiles on 8 and 10 March 2005.

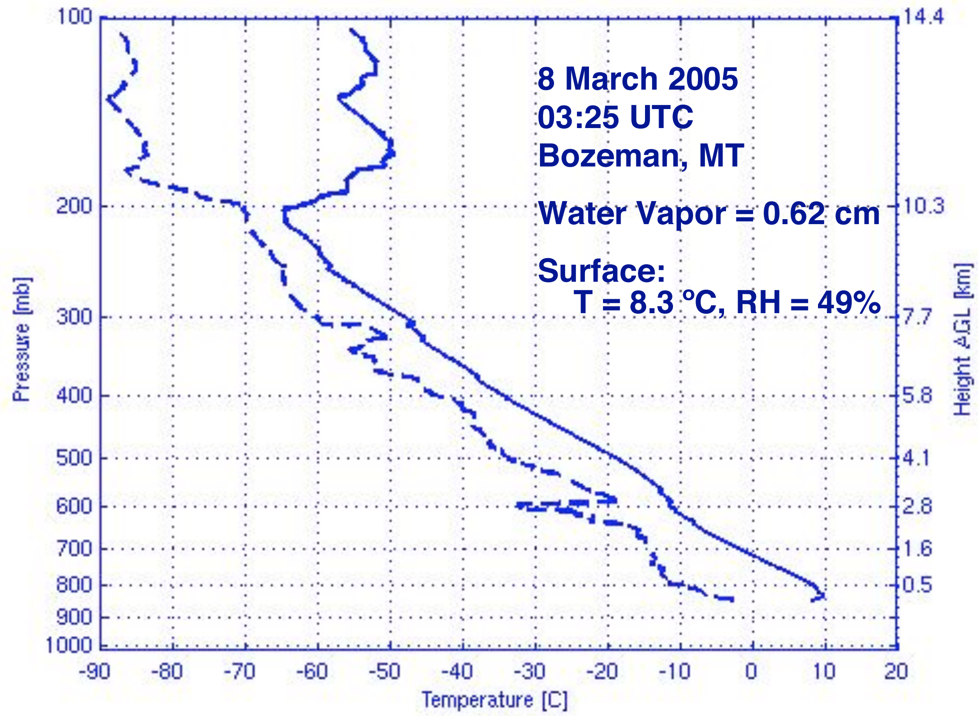

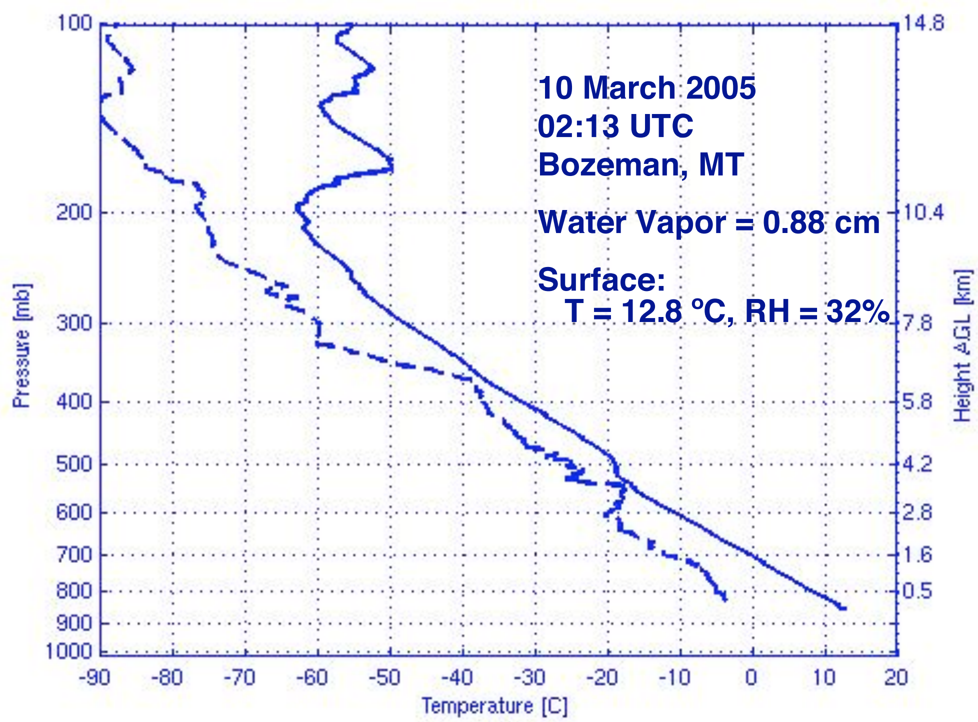

The temperature is useful in physically explaining lildar depolarization ratios, because if it is below -40 ºC, it is impossible to have liquid water (because it would freeze at this temperature even in the absence of condensation nuclei, as explained in the introduction). The radiosonde data in the figures are converted to height above ground level for comparison with the lidar. The launch on March 3 terminated after only 6 km, but it is still useful, because most of the water vapor is below this altitude, and because it happened to terminate at about -40 ºC, the key temperature.

Figures 14-18, 20, 22 and 23, are eight one-minute lidar data segments which are representative of the variety of conditions observed on these four days. All these data were taken with field stop #10 (8.83 mrad FOV) and a 1 nm FWHM spectral filter. Table 6 is a summary of the scattering features in these figures, with measured depolarization ratios, heights and temperatures.

7 March 2005, 23:04 UTC (Figure 14) — In the co-pol signal, there is a dense layer at 6.2 km. That layer has a depolarization ratio $\delta = 0.046$, but it is surrounded on top and bottom with a regions of $\delta = 0.5$. It is important to use the co-pol signal to interpret the depolarization ratios, since the uncertainty in the ratio is worst where the signals are small. The temperature at this layer is -37.8 °C. Because of the low depolarization ratio, this cloud can be classified as supercooled liquid water. Thin (in range) but dense layers with relatively sharp backscatter gradients on the edges are typical of supercooled water (Hogan et al. 2004). The temperature makes this interpretation possible, but it is near the edge of being too cold for liquid water. It is also typical to have faint ice crystal scattering with high depolarization around a supercooled layer.

Figure 14. Co-polarized signal and depolarization ratio for 7 March 2005, 23:04 UTC.

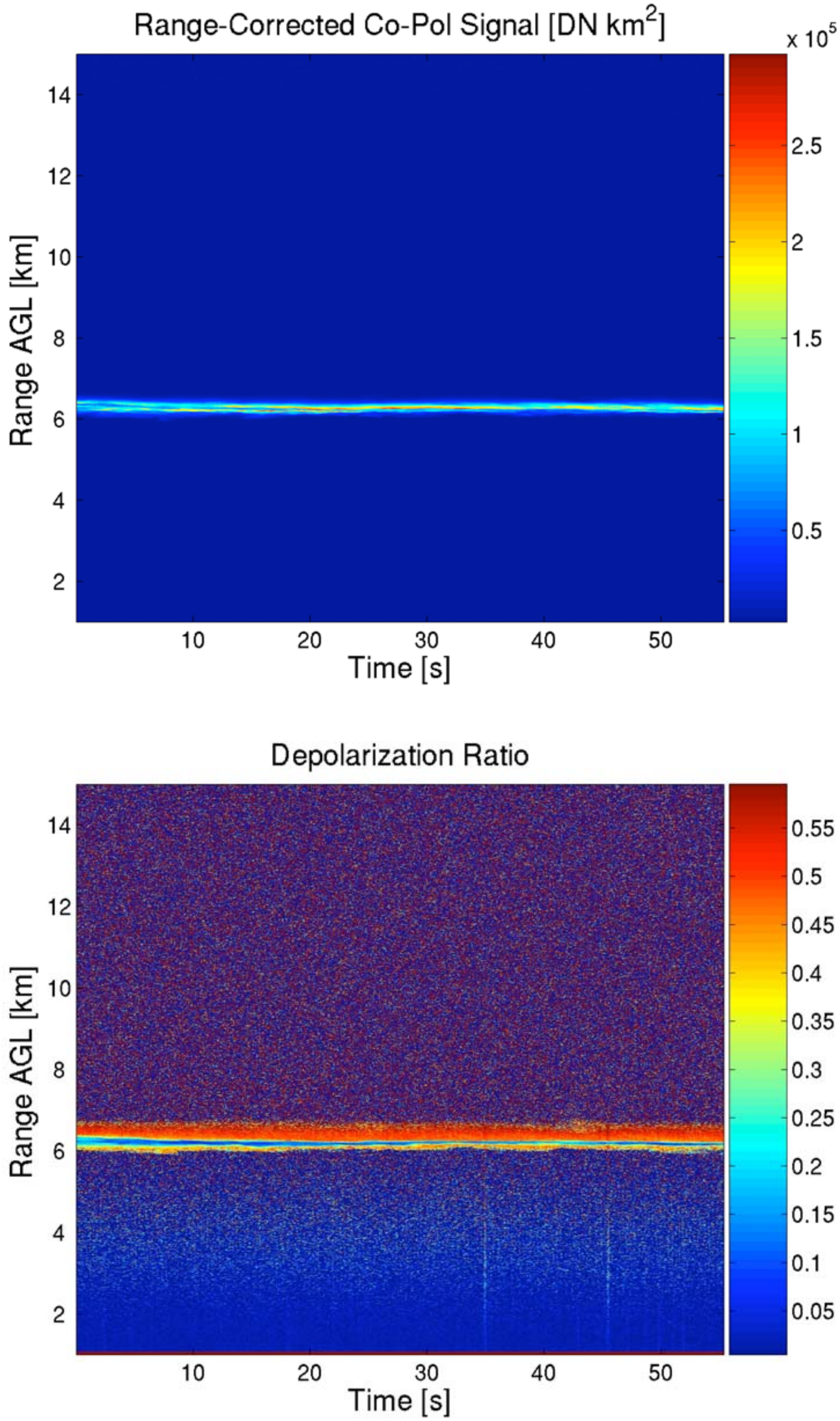

9 March 2005, 22:04 UTC (Figure 15) — This image is mostly clear, but there is a layer at 4.4 km for the first half of the minute, with $\delta = 0.022$. The temperature there is -19.6 °C, and this cloud is certainly liquid water. One test of the lidar system is to see if low depolarization ratios can be measured, because most problems with the polarization of the system tend to increase the measured depolarization. I will discuss laboratory tests of the polarization purity of the system in a following section, but these data are encouraging. Recall that the most common depolarization figure for liquid water is $\delta <$ 3%. This layer is only about 40 m thick, and there is minimal multiple scattering (unlike the next case).

10 March 2005, 01:42 UTC (Figure 16) — This case has lots of scatter from a thick cloud between 3.9 and 5 km. The depolarization image looks like a rainbow – δ increases with penetration depth into the cloud. This is the most recognizable feature of multiple scattering, since photons that penetrate deeper have a greater chance of scattering off more than one cloud particle. The depolarization ranges from less than 0.1 up to 0.43, while the temperature ranges from -18.7 °C to -24.4 °C. The bottom of this cloud is certainly liquid water, and the rest of it could be liquid or ice or a mixture of the phases. In this case, multiple scattering is a real problem for phase discrimination.

3 March 2005, 04:19 UTC (Figure 17) — This image shows two narrow layers, with very different depolarizations. The layers at 4.2 km and 7.8 km have $\delta = 0.023$ and 0.22, respectively. The lower layer, at -25 °C is water, and the high layer, well below -40 °C (this was the sonde launch that terminated early), is probably ice but could also be an aerosol layer. Notice the two faint layers at 8.4 and 8.6 km, with low depolarization.

Figure 15. Co-polarized signal and depolarization ratio for 9 March 2005, 22:04 UTC.

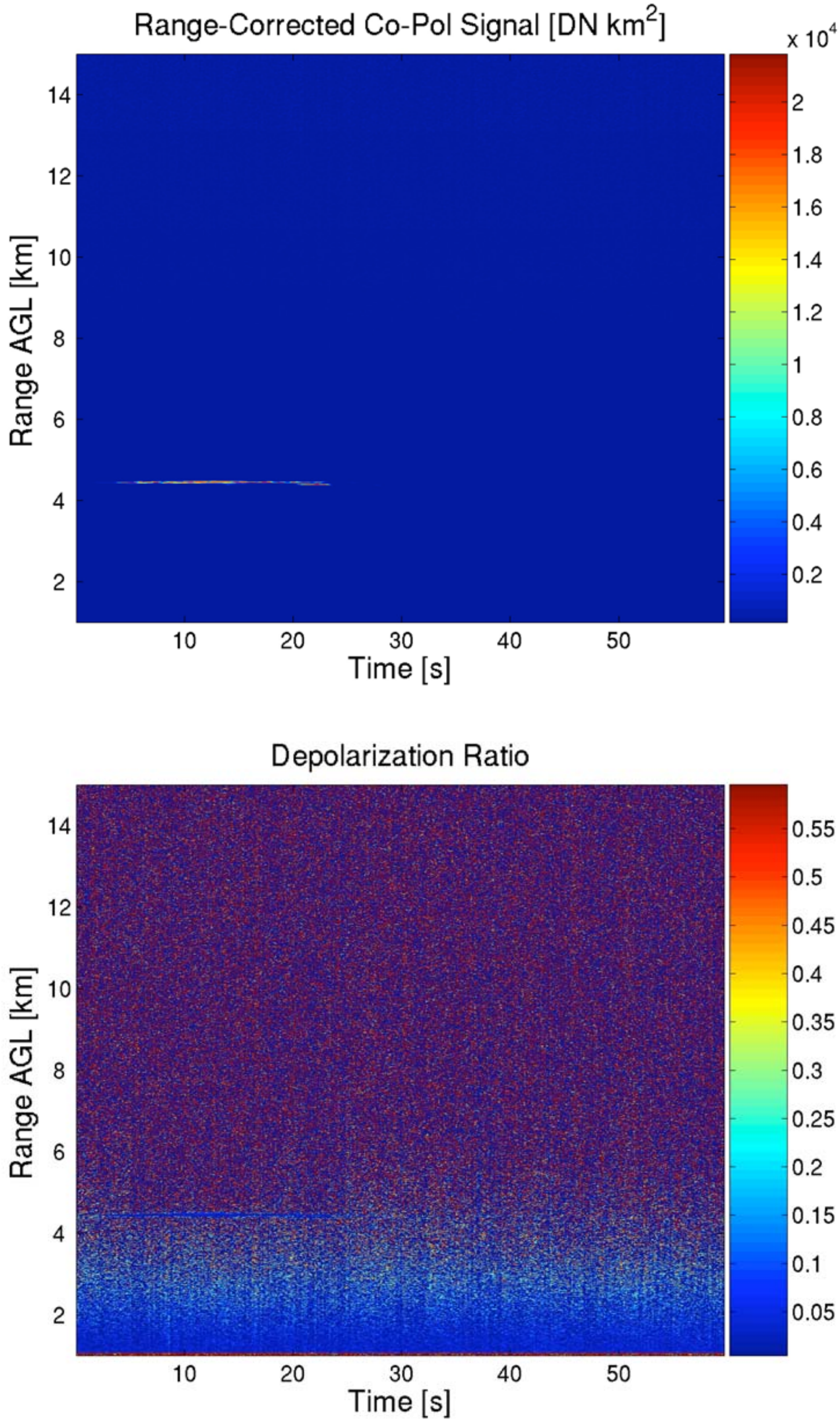

Figure 16. Co-polarized signal and depolarization ratio for 10 March 2005, 01:42 UTC.

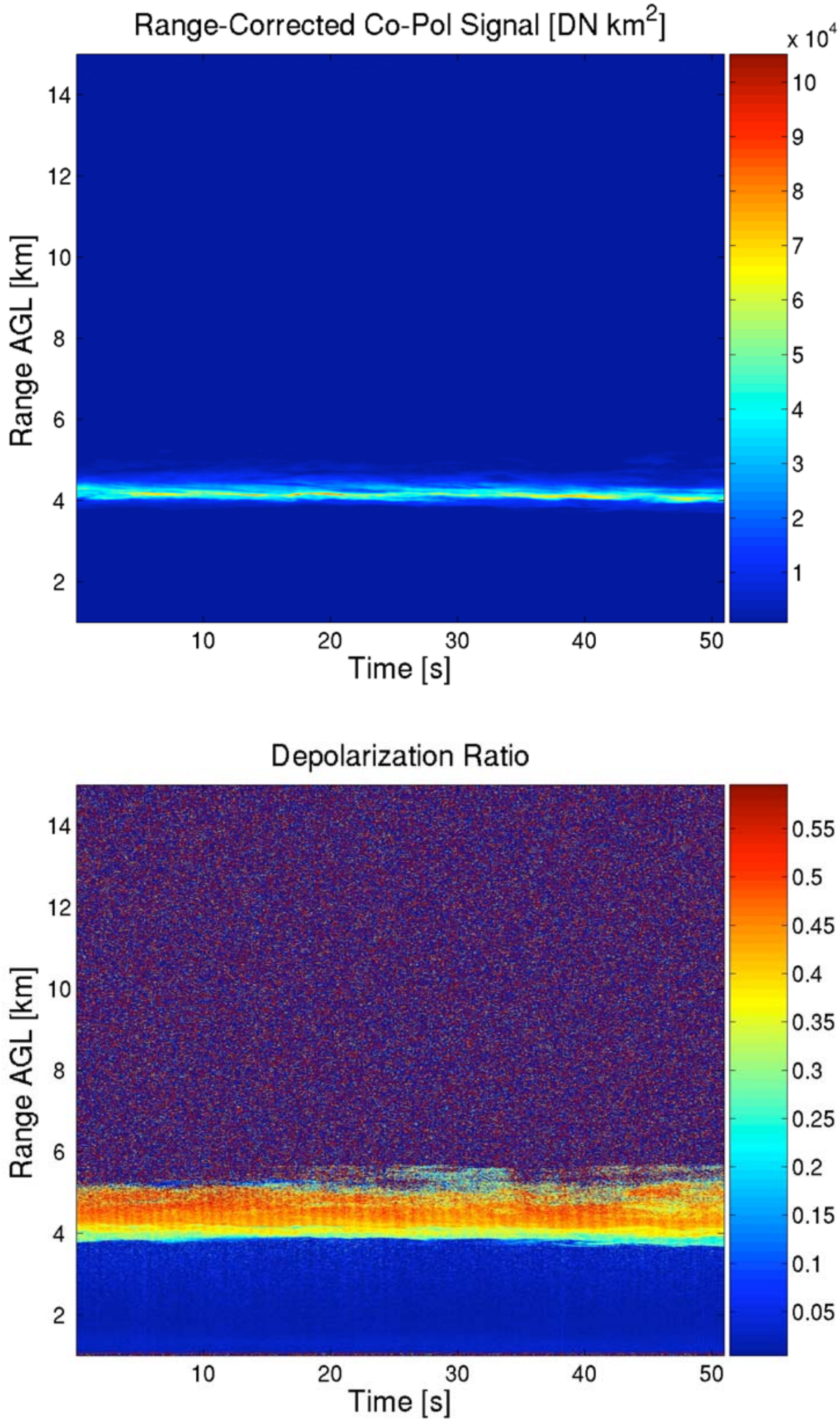

Figure 17. Co-polarized signal and depolarization ratio for 3 March 2005, 04:19 UTC.

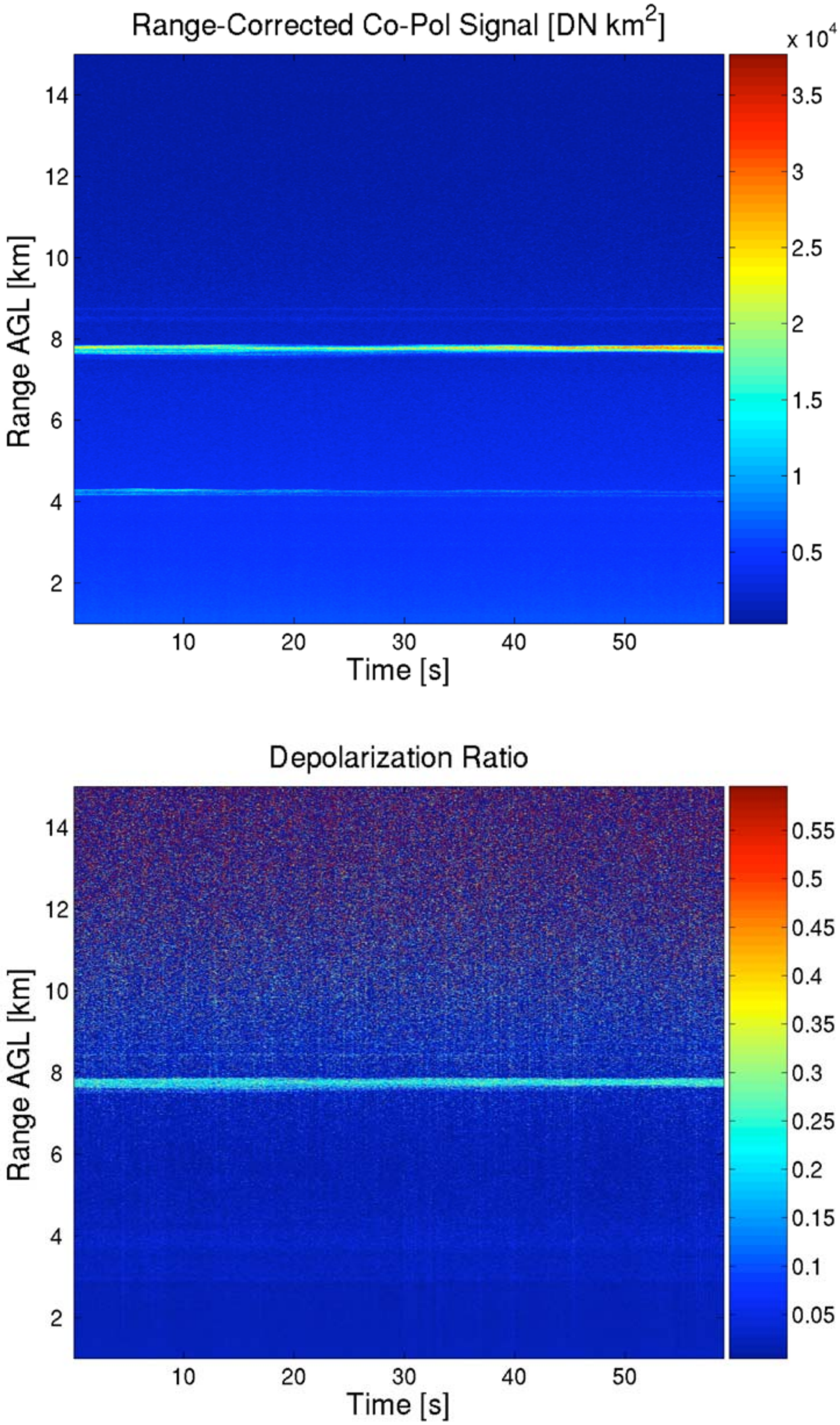

These are so faint (~ 25 DN), that the depolarization ratio doesn't mean much. These layers are also either ice crystals or some other aerosol layer. Figures 20, 22 and 23, from March 1 and 3, also show evidence of a thin layer at high altitude, so I will come back to this when I discuss those.

8 March 2005, 02:44 UTC (Figure 18) — This case illustrates extinction of the signal from one cloud by another cloud. The 3.8 km layer increases in density over the course of the minute, causing the 7.6 km layer to disappear. The high layer, at -46.8 °C and with $\delta \sim 0.4$, is a very thin layer of ice, and the low layer, at -16.5 °C and with $\delta = 0.01$, is water. As the lower layer gets denser, multiple scattering is apparent – the depolarization increases up to 0.4 at the top of the layer. Figure 19 is a plot of the depolarization as a function of cloud penetration depth for this data. An increase in depolarization from near zero up to about 0.4 after 150-200 m matches well the characteristics of multiple scattering given by Pal and Carswell (1973).

1 March 2005, 01:21 UTC (Figure 20) — In this image, two thin layers (~100 DN) at 9 and 9.5 km have $\delta = 0.02$ and 0.30, respectively. The lower layer is actually the slightly stronger of the two in the co-pol signal, yet its depolarization is almost zero. Therefore, the difference between the layers cannot be attributed to some kind of extinction of these small signals – there is a real difference between these layers. On this evening, there were no clouds visible to the eye, and the stars were sharply visible. The temperature at this altitude is below -60 °C, so liquid water is not a possibility. The only possibility for the lower δ layer to be ice would be if the crystals were oriented

Figure 18. Co-polarized signal and depolarization ratio for 8 March 2005, 02:44 UTC.

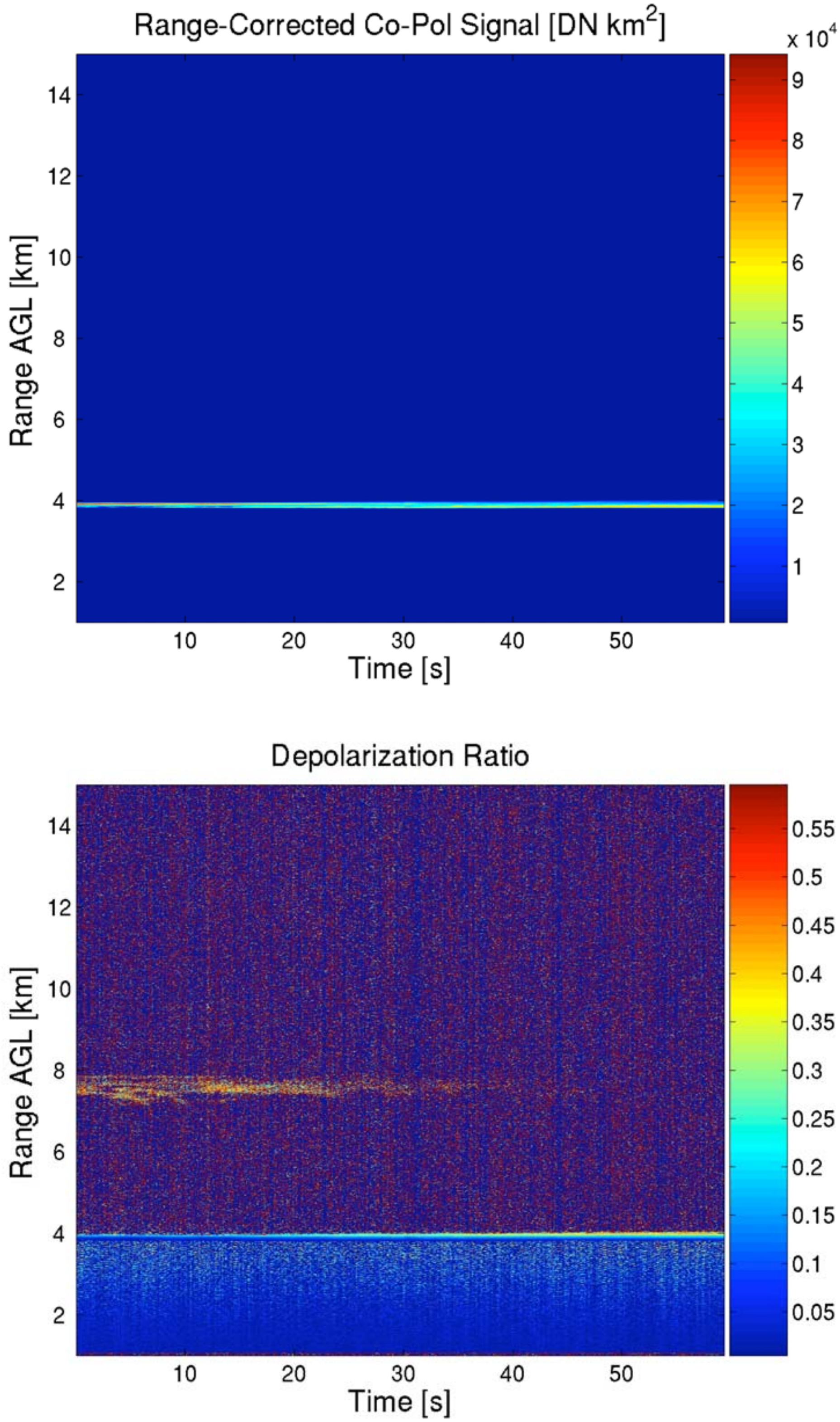

Figure 19. Increasing depolarization with cloud penetration depth (evidence of multiple scattering) on 8 March 2005, 02:44 UTC, at a range of 3.8 km and at -16.5 ºC.

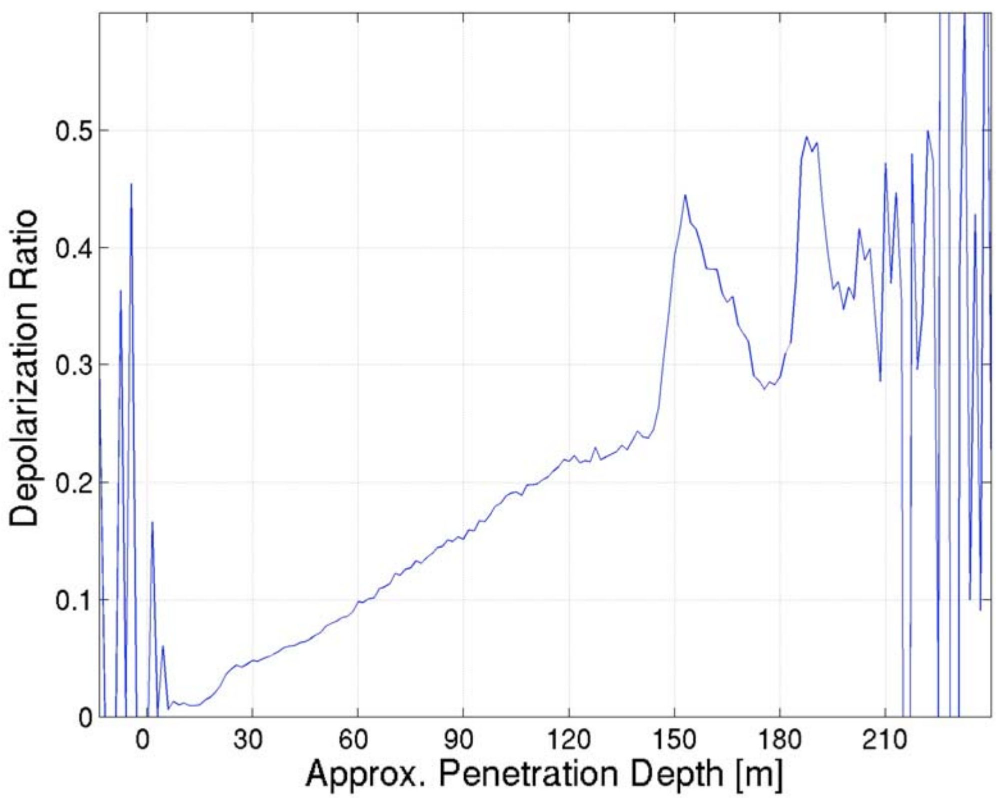

horizontally and the lidar was precisely pointing at the zenith. One or both of these layers could be an aerosol, such as dust or pollution.

It is known that dust from high altitudes on the Tibetan plateau in China can be blown across the pacific. Asian dust has been observed by lidars in Japan, Alaska, Utah and Colorado, to name a few (Sugimoto, Asian Dust Network, 2005). Dust has been observed with $\delta = 0.14\text{-}0.27$ (Sakai et al. 2003) and with $\delta = 0.1\text{-}0.2$ (Sassen 2005), and since the presence of dust can cause cirrus ice particles to nucleate, it is often observed mixed with cirrus. Figure 21 is a NOAA back-trajectory analysis of the atmosphere at

Figure 20. Co-polarized signal and depolarization ratio for 1 March 2005, 01:21 UTC.

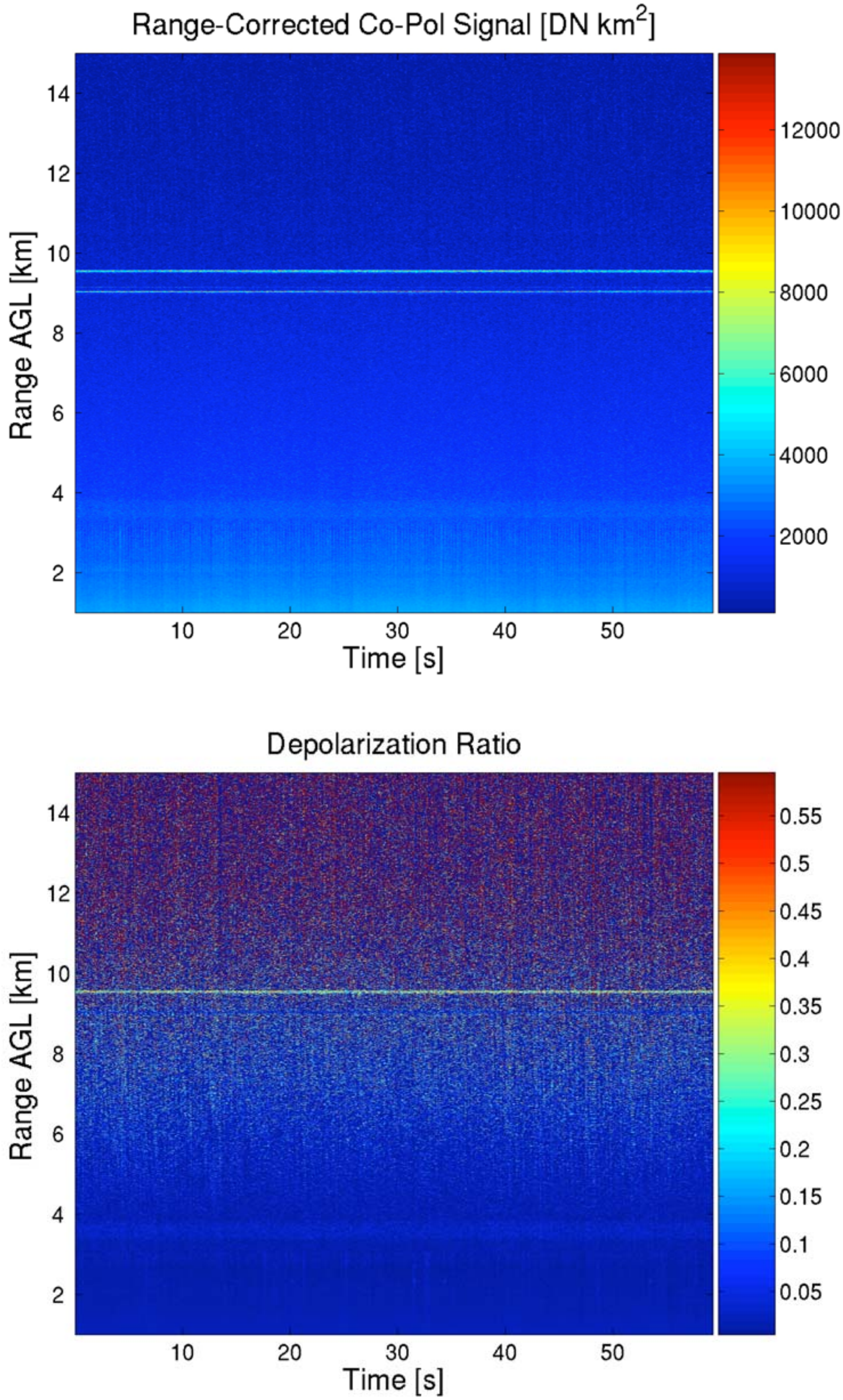

different altitudes over Bozeman on 1 March 2005. It shows that air that was at 7500 m AGL over Bozeman is calculated to have come from 3500 m over east-central China ten days earlier. Around 20 February 2005, there was thick haze over Beijing and most of

Figure 21. Ten-day backward trajectory analysis of the atmosphere at 500 m, 4000 m, and 7500 m AGL over Bozeman, MT, on 1 March 2005.

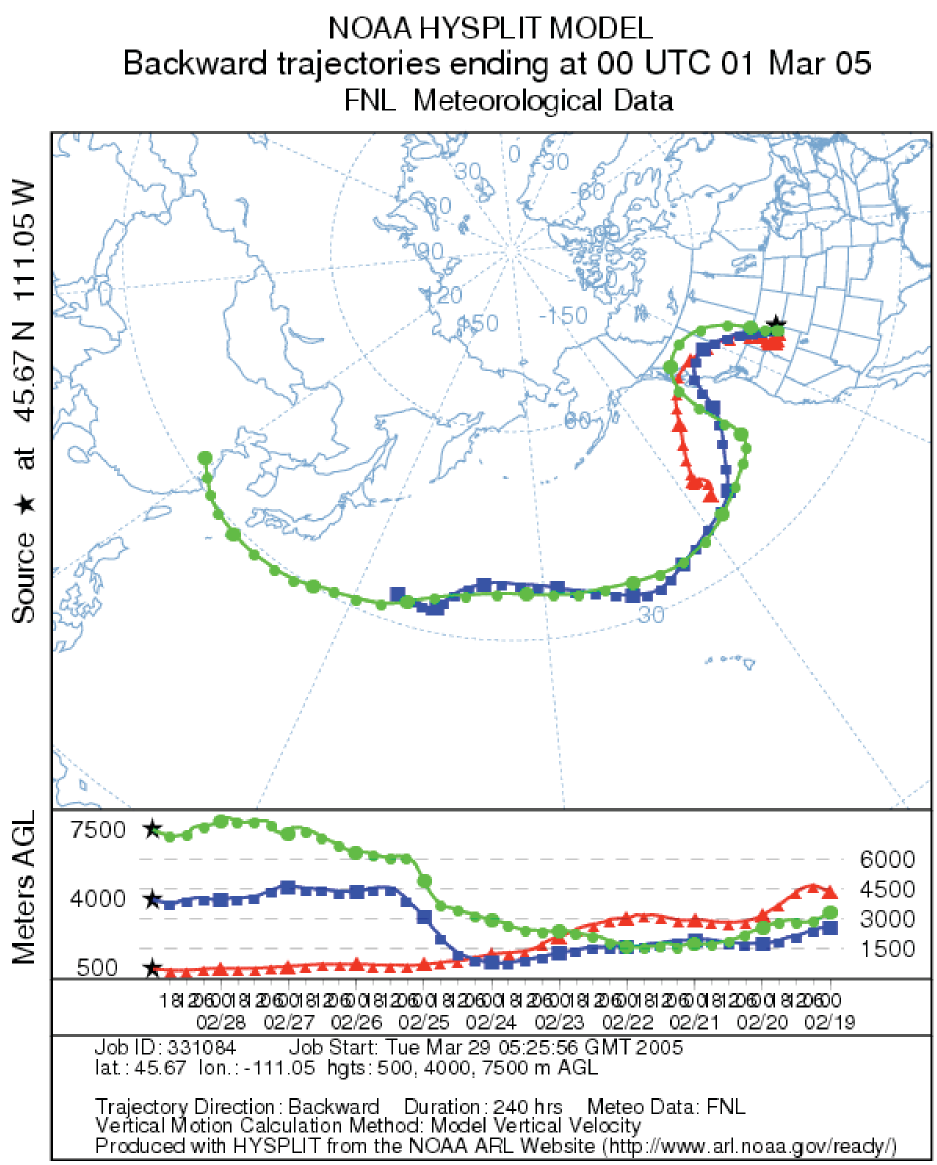

central China, but the air was very stable, so the likelihood is low that haze could have risen out of the boundary layer to an altitude where it would be blown eastward. Chances are greater that sand on the Tibetan plateau, at an elevation of about 3500 m, was blown across this stable air and out over the Pacific (G. Shaw 2005). Given the available information, this is the best explanation of these data. The final two examples (also on March 1 and 3) exhibit the same probability of Asian dust.

1 March 2005, 03:32 UTC (Figure 22) — This minute of data has more than four distinguishable layers between 6.9 and 8.7 km, and as noted before, the stars were still visible. The temperature at those altitudes ranges from -47 to -60 °C, and δ ranges from 0.18 to 0.24. As in the previous case, this is either subvisual cirrus ice, or dust, or some combination.

3 March 2005, 00:17 UTC (Figure 23) — In this last example, there are layers at 4.3, 4.6, and 4.8 km, and they have $\delta = 0.237$, 0.220, and 0.013, respectively. The temperature is -26.4 °C at 4.3 km and is -30.6 °C at 4.8 km, so there is likely a mixture of liquid water and ice here. The fact that the highest of the three layers has the lowest depolarization suggests that it is supercooled water and the lower layers are not. Notice also, the very thin (~ 20 DN) signal at 8.8 km. The depolarization ratio is approximately 0.15, but it is uncertain with such a small signal.

Table 6 is a summary of the scattering features in these figures, with measured depolarization ratios, heights and temperatures.

Figure 22. Co-polarized signal and depolarization ratio for 1 March 2005, 03:32 UTC.

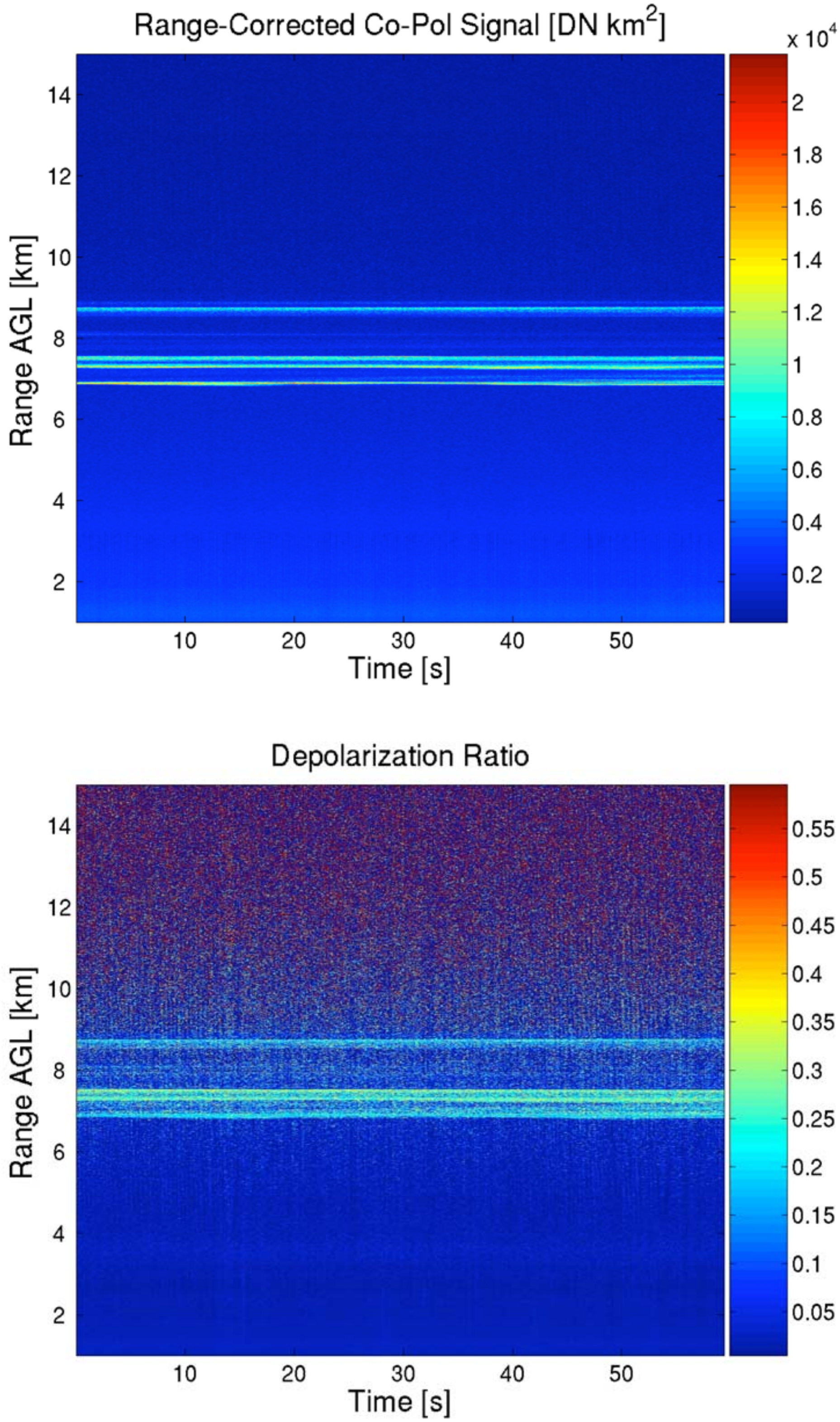

Figure 23. Co-polarized signal and depolarization ratio for 3 March 2005, 00:17 UTC.

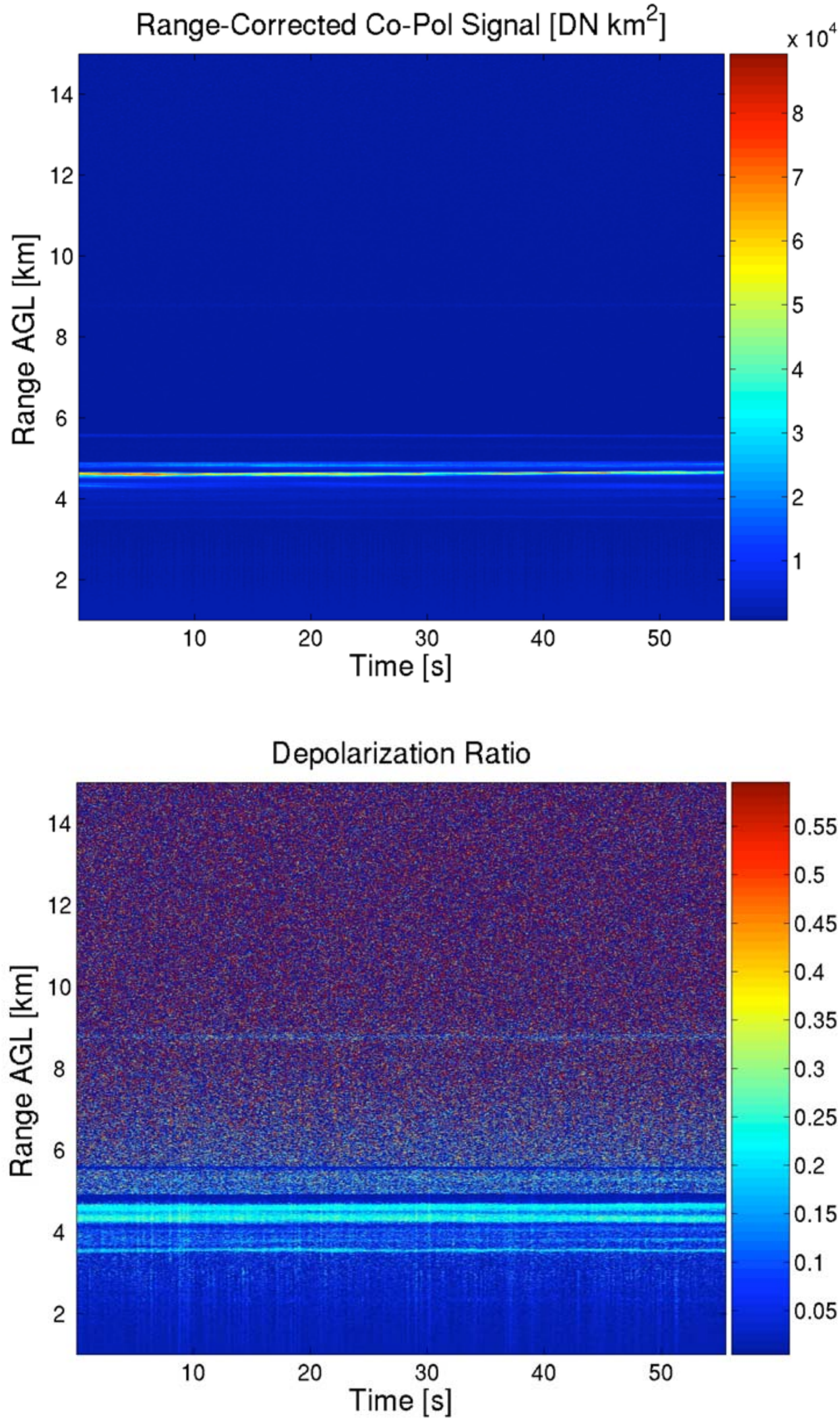

Table 6. Summary of scattering features observed in Figures 14-18, 20 , 22, and 23.

Date, Min., Figure	*A/D Range [V]*	*PMT Gain Cont. [V]*	*Height AGL [km]*	*Depol. Ratio δ*	*Temp [ºC]*	*Approx. Peak [DN]*	*Interpretation*
3/7 23:04 Fig. 14	1	3.5	6.2	0.046	-37.8	4000	Dense, supercooled water layer
3/9 22:04 Fig. 15	2	3.0	4.4	0.022	-19.6	1000	Supercooled water
3/10 01:42 Fig. 16	1	3.5	3.9 – 5	< 0.1 up to 0.43	-18.7 up to -24.4	3000	Thick water (or mixed phases), with multiple scattering
3/3 04:19 Fig. 17	0.5	3.85	4.2	0.023	-25	225	Water
			7.8	0.22	< -40	330	Ice or dust
			8.4, 8.6	0.1 ?	< -40	25	Very faint, ice crystals or dust
3/8 02:44 Fig. 18	5	3.5	3.8	0.01 up to 0.4	-16.5	3200	Water, with multiple scattering
			7.6	0.4 ?	-46.8	~5	Faint, ice
3/1 01:21 Fig. 20	0.5	3.5	9	0.02	-62.7	85	Thin, dust, subvisual
			9.5	0.30	-61.7	70	Thin, dust or ice, subvisual
3/1 03:32 Fig. 22	0.5	3.5	6.9	0.18	-46.7	220	Ice or dust, subvisual
			7.3	0.25	-50.5	200	Ice or dust, subvisual
			7.5	0.25	-51.5	150	Ice or dust, subvisual
			8.7	0.18	-60.3	100	Ice or dust, subvisual
3/3 00:17 Fig 23	1	3.5	4.3	0.237	-26.4	430	Ice or mixed phases
			4.6	0.220	-28.6	2200	Ice or mixed phases
			4.8	0.013	-30.6	820	Supercooled water
			8.8	0.15 ?	< -40	~20	Faint, dust or ice

Comparison with Cloud Imager Data

The Infrared Cloud Imager (ICI) uses an uncooled microbolometer detector array to image downwelling radiance from the sky in the 8-14 μm band. Its purpose is to measure spatial cloud statistics in its 18° by 13.5° field of view (Thurairajah and Shaw 2005). The measured radiance of every image is calibrated by turning the field of view to two blackbody radiators at different temperatures. Clouds are seen as warmer than clear sky, but water vapor also radiates in this band. To good approximation, radiance from the whole vertical water vapor column needs to be subtracted. The magnitude of this correction, which is based on MODTRAN simulations, depends on the integrated water vapor obtained from the radiosondes (or from a microwave radiometer), and the surface temperature.

The ICI was operated with the lidar on March 1, 3 and 8, taking measurements every couple of minutes. Figure 24 shows six images, after the water vapor correction, for comparison with the lidar data just presented. Image A was not taken with the lidar running – it is included as an example of a clear, dry sky. Image B (compare to Figure 22) was taken on the evening that the stars were visible, but the lidar saw four high altitude layers. ICI also shows that it is not clear out. Residual radiance values of 6-8 $Wm^{-2}sr^{-1}$ are not high, but they would normally be above the threshold used to determine whether it is clear or cloudy. This is evidence that the ICI can see either subvisual cirrus or dust. Dust could be seen either due to its own emission or by reflection of the infrared emission of the earth. Image C (compare to Figure 17) has about the same radiance, and the lidar data showed two layers that were not thick. Image D (compare to Figures 10-11), again, is about the same. Image E (compare to Figure 18), at $> 15\ Wm^{-2}sr^{-1}$ is more typical of a thick cloud, though some can be even warmer. In the lidar data, a low water cloud was increasing in intensity, and there was a thin layer up high. On this evening, clouds were moving in and out on short time scales, and Image F catches the edge of a low cloud. Given the lidar data, Image F could be interpreted as two layers: there is the cloud (in yellow), and the background is not completely clear.

Figure 24. Images and average radiances from the Infrared Cloud Imager, corrected for the presence of water vapor, on days of lidar operation.

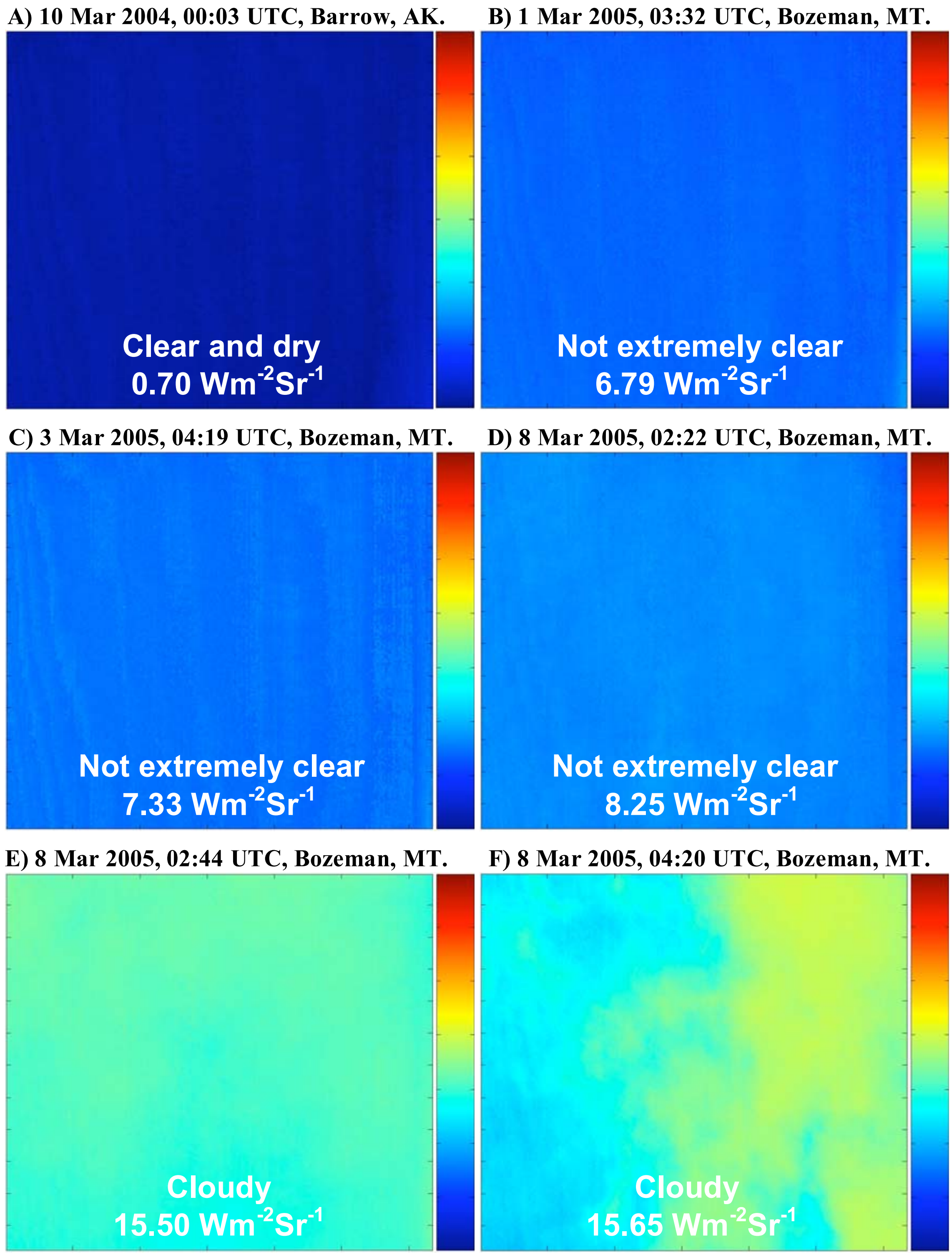

The ICI data and the lidar data are consistent. However, information from the two instruments complement each other more than they can verify each other. The imager gets spatial cloud statistics in a surer way than the lidar (with a wider field of view), and is a direct measure of the radiation from a cloud. The lidar has the higher time resolution and vertical resolution, and is able to measure microphysical cloud properties. Longer-term operation of the two instruments side by side could yield some interesting atmospheric science.

Receiver Polarization Purity

How accurate are the depolarization measurements? Answering this question requires measuring the response of the receiver to light with a known polarization state. The following description of the system will fall short of a full Stokes parameterization; light that is incident on the receiver is treated as being composed exclusively of linear co-pol and linear cross-pol components.

One common measure for polarizing optics is the extinction ratio (stated as 100:1 or 10,000:1 for different polarizers, for example). This is the ratio of co-pol to cross-pol light exiting the optic, assuming that the light incident on the optic was randomly polarized. Another measure of polarization is called the degree of polarization. If a polarizer, used as an analyzer, is rotated in the beam, followed by a detector, the degree of polarization of the beam is the difference between the maximum and minimum powers on the detector, divided by the sum of the maximum and minimum powers. A linearly polarized beam has a degree of polarization of one. If you assume a perfectly linear input beam, then the degree of polarization of the output beam is descriptive of the device under test.

Since the goal is find the difference in the measured depolarization from the depolarization caused by the scattering particles, the most relevant measure of the system components is a simple depolarization ratio, the cross-pol signal divided by the co-pol signal. This is similar in concept to an extinction ratio, being just the inverse. System components (such as the telescope or lenses) could potentially depolarize the signal. To measure this, linearly polarized light (with nearly perfect degree of polarization) is incident on the device under test, and the exiting beam is tested with an analyzing polarizer and detector. Any cross-polarized signal is due to depolarization by the device. Testing components such as the liquid crystal and polarizers is a little different. In this case, the test is of how well the desired polarization is selected – the analyzer is built into the device under test. Therefore, to test the whole receiver system, co-pol and cross-pol light is made incident separately. For each, the transmission through the system is measured for each receiver setting (each state of the liquid crystal).

I will describe tests performed on the telescope, lenses, and liquid crystal separately, and then tests of the whole assembled receiver. For most of the tests, a 5 mW CW 532 nm Nd:YAG laser source was used, with a glan-laser polarizer which is specified to a 100,000:1 extinction. The polarization of this beam was assumed to be perfectly linear. With it, a polarizer used as an analyzer (specified at an extinction of 10,000:1) was repeatably tested to be better than 70,000:1. As extinction ratios get extreme these measurements are very touchy, and the best measurement of this polarizer was as good as 162,600:1. These values imposes limits on the measurements of the system components.

Testing the telescope is a bit tricky since it is hard to come by a linearly polarized beam of light that simultaneously fills the whole 8" aperture and is collimated, like light from the far-field. I test it three ways: (1) with a laser beam diverged to fill the aperture – but not collimated, (2) with a narrow laser beam aimed at different places on the primary mirror – but not filling the aperture, and (3) with skylight, which both fills the aperture and is collimated – but has less certain polarization. For the first method, the ray incidence angles are not realistic since the beam is diverging severely. Since the source is in the near-field of the telescope, the beam exiting the telescope is donut-shaped due to the central obstruction. By varying the position of the source within the FOV, the measured depolarization of the exiting beam varies from 1.12×10^{-4} to 3.53×10^{-4} (8,949:1 to 2,833:1). In the second method, the narrow laser beam is aimed at different points on the primary mirror, some near the center and some near the edge. All points are better than 3.06×10^{-5} (32,654:1). Some are as good as 1.50×10^{-5} (66,554:1), whereas, if the telescope is entirely removed, the beam depolarization is 1.17×10^{-5} (85,183:1). There is no clear correlation between the beam position on the primary mirror and the depolarization, but the beam position on the secondary mirror was unclear and this could have an effect. The third method, aiming the telescope at the daytime sky, is attractive because it fills the telescope aperture with light from far away. The disadvantage is that measurements had to be taken quickly so that the polarization and irradiance of the skylight can be assumed not to have changed. The light from the telescope goes through a laser line filter and is focused on a detector. I observe the detector power vary by 2% over 1 minute for clear blue sky, and vary by 10% over seconds for cloudy sky, so I take the measurements on a clear day. To make the skylight as linearly polarized as possible, a large sheet polarizer (only rated at 100:1) covers the front of the telescope. In two measurements, the depolarization of the light exiting the telescope is 5.49×10^{-4} and 5.1×10^{-4} (1,821:1 and 1,960:1). With a second sheet polarizer added, coaligned with the first, the exiting beam improves to 4.68×10^{-4} (2,136:1). The skylight measurements, being well beyond the quality of the polarizers, are not very informative. Each of the three methods has its drawbacks, but none of the measurements show that depolarization by the telescope is very large.

Of the two 1" lenses used in the receiver, I test the shorter focal length lens, a 40 mm Thor Labs LB1027-A lens, because it has higher curvature, and higher ray incidence angles are expected to give the worst case depolarization. (However, the only lens that matters is the longer focal length lens because only it comes before the liquid crystal and polarizer.) The same lens is tested with and without a broadband visible anti-reflection coating. I expand the beam to 1 cm to get a realistic distribution of incidence angles on the lens, analyze the beam, and then focus it onto the detector. In repeated measurements, the depolarization of the uncoated lens is $\sim 8.02 \times 10^{-4}$ (12,462:1) and the depolarization of the coated lens is $\sim 2.70 \times 10^{-5}$ (37,037:1). Not only does the coated lens preserve linear polarization better, but it has a higher transmission. Therefore, I have chosen coated lenses for the receiver.

The liquid crystal and polarizer are tested as a unit – together they act as the polarization analyzer in the receiver. The lidar laser is vertically polarized, so the co-pol orientation in the receiver is also vertical as the components are mounted (perpendicular to the mounting surface). I choose to orient the polarizer vertically, so that if the lidar was operated in a single-polarization mode, the liquid crystal could be simply removed. The polarizer is a 2" film polarizer from Meadowlark Optics, with better than 10,000:1 extinction. The fast and slow axes of the liquid crystal need to be at 45° degrees off the polarizer orientation, and this is how it comes mounted from the manufacturer. With a co-pol beam expanded to avoid spatial uniformity errors, and with the liquid crystal tuned to switch between zero and half-wave retardances, the beam exiting the liquid crystal-polarizer combination has a 2,651:1 switching ratio. This is not the same as an extinction ratio, because it involves two different liquid crystal states. I test the liquid crystal in a way that more clearly relates to lidar depolarization measurements next, in the assembled receiver.

A polarization characterization of the whole assembled receiver is the most important test, because it could reveal misalignments between the components. The previous tests tell whether or not a certain component is good enough to be a part of the system, but this test will show the accuracy of the lidar depolarization measurements. In this test, the lidar is aimed horizontally on an optics table. It is crucial to align the polarization of the input beam precisely to be horizontal (cross-pol) and then vertical (co-pol), so I use the part of the beam rejected out across the room by the glan-laser polarizer as an indicator of the polarizer's orientation. For each input polarization, the power is measured before the telescope and again behind the receiver optics box, and the transmission is calculated. After the alignment is correct, this measurement is done four times – once for each combination of input polarization and liquid crystal state. Also, various other configurations, such as with the liquid crystal removed, are tested.

The transmission measurements, in Table 7, are useful for both for finding the error in lidar depolarization ratios, as well as for radiometrically calibrating the system. Note that $T_{\frac{\lambda}{2}\perp}$ and $T_{0\parallel}$ are the transmissions of the two polarization states when you intend to measure each of those states by setting the liquid crystal appropriately. It is good that these transmissions are the same, and acheiving this requires very precise alignment. The other two values, $T_{\frac{\lambda}{2}\parallel}$ and $T_{0\perp}$, are the ones that should be minimized.

To find the error in depolarization ratios, first recall (from Equation 1.6) that the depolarization caused by a target scattering object is the ratio of the two linearly polarized optical powers *incident on the receiver*, $\delta_{target} = P_{\perp} / P_{\parallel}$. However, the measured depolarization ratio is the ratio between the signals *incident on the detector* for the two liquid crystal states:

$$\delta_{measured} = \frac{T_{\frac{\lambda}{2}\perp} P_{\perp} + T_{\frac{\lambda}{2}\parallel} P_{\parallel}}{T_{0\perp} P_{\perp} + T_{0\parallel} P_{\parallel}}. \tag{3.1}$$

This can be neatly rewritten in terms of the target depolarization:

$$\delta_{measured} = \frac{T_{\frac{\lambda}{2}\perp} \frac{P_{\perp}}{P_{\parallel}} + T_{\frac{\lambda}{2}\parallel}}{T_{0\perp} \frac{P_{\perp}}{P_{\parallel}} + T_{0\parallel}} = \frac{T_{\frac{\lambda}{2}\perp} \delta_{target} + T_{\frac{\lambda}{2}\parallel}}{T_{0\perp} \delta_{target} + T_{0\parallel}} \tag{3.2}$$

Table 7. Measured transmission of the assembled receiver (with the liquid crystal set for zero and half-wave retardances) for different incident linear polarization states.

Measured With Laser Line Interference Filter, T = 0.5212		Liquid Crystal Setting	
		Zero Retardance (4.950 V)	Half-wave Retardance (2.055 V)
Incident Polarization	Co-polarized	$T_{0\parallel} = 0.3653$	$T_{\frac{\lambda}{2}\parallel} = 0.0014$
	Cross-polarized	$T_{0\perp} = 0.0019$	$T_{\frac{\lambda}{2}\perp} = 0.3651$

Transmissions for Other System Configurations:

Without Laser Line Filter
$T_{0\parallel} \approx T_{\frac{\lambda}{2}\perp} = 0.7007$

Without Liquid Crystal (Single-Polarization Mode)
$T_{\parallel} = 0.3993,\ T_{\perp} = 2.009 \times 10^{-4}$

Without Laser Line Filter or Liquid Crystal
$T_{\parallel} = 0.7660,\ T_{\perp} = 3.855 \times 10^{-4}$

Using the transmissions with the current filter, from Table 7,

$$\delta_{measured} = \frac{0.3651\delta_{target} + 0.0014}{0.0019\delta_{target} + 0.3653}. \quad (3.3)$$

Finally, the error in a measured depolarization ratio is $\Delta\delta = \delta_{measured} - \delta_{target}$, and using Equation 3.3, the predicted error is plotted as a function of target depolarization in Figure 25. For target depolarization ratios up to 0.7, the error is always positive; it sets a minimum measured depolarization. The worst case is an additive error of 0.0038, about 0.4%. This is an acceptable error for depolarization ratio measurements, which are typically not stated to better than 1%. The worst error occurs when δ_{target} is zero. This is easily explained as follows: If the system has a depolarization such that it mixes a fixed fraction of the co-pol and cross-pol signals into the other, the net effect will be less when the two signals are comparable to begin with.

Of course, good receiver polarization discrimination is useless without a highly-polarized transmitter. The laser polarization is measured with a glan-laser polarizer and a volume absorbing calorimeter (without filters). The transmitted average power is 3.2 W with the polarizer aligned vertically, and 2.4 mW with the polarizer aligned horizontally. Therefore, the laser is linear to 7.5×10^{-4} (1,333:1). The two beam steering mirrors are designed for high energies at 532 nm, and for 45° incidence angles. I find that these

Figure 25. Predicted depolarization ratio errors given the measured transmission of the receiver for each liquid crystal state and each incident polarization.

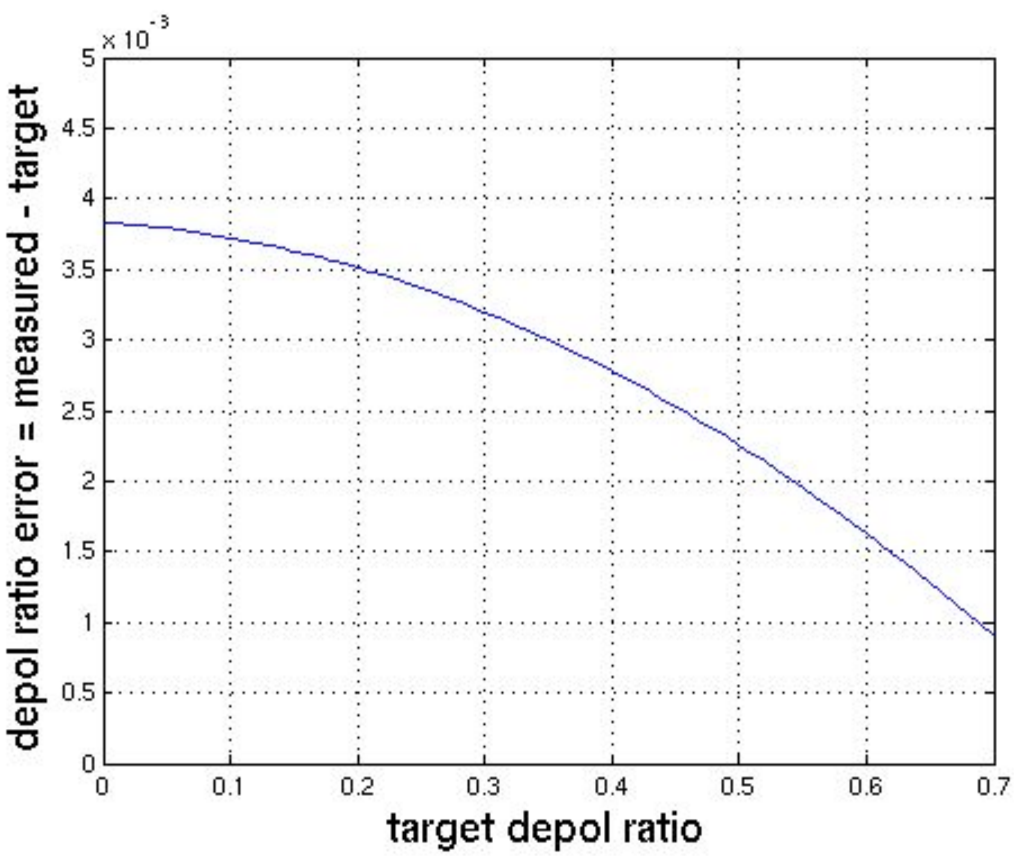

mirrors have a higher reflection, but slightly worse depolarization, compared to standard uncoated mirrors. I use the mirrors in an orientation in which the plane of polarization is perpendicular to the plane of reflection, the *S* polarization. Measurements of both coated and uncoated lenses show that the reflection is better for incident *S* polarization, and the polarization is better maintained for incident *P* polarization. However, the depolarization in this configuration is still good to 29000:1, so this is not an issue.

Overlap and Alignment

The overlap between the laser and telescope as a function of range is computed for various fields of view and inclination angles between the laser and telescope. The gaussian shape of the laser beam is taken into account. Overlap function increase with range from zero to some maximum value, such as one, where, ideally, its value is flat with range, and then for non-zero inclination angles, the beam comes out of overlap at long ranges.

The four independent variables are the laser divergence, the telescope field of view, the horizontal separation between laser and telescope, and the inclination angle between the laser and telescope. For these calculations, I fix the laser divergence at 2.16 mrad and the horizontal separation at 19 cm. Each of the six plots in Figure 26 are for a different field of view, and each plot shows the overlap function as the inclination angle is moved away from 0°. Table 8 shows some lower and upper range limits for certain overlap values.

Appendix C contains the MATLAB routine used to produce each overlap function. The computation can take a very long time, even when one reduces the

Table 8. Selected range limits for certain overlaps at various FOVs and inclinations.

Aperture #; & FOV	Incllnation θ [mrad]	Peak overlap value	Overlap value at 15 km	Lower range limit [m]	Upper range limit [m]
				Range limits for overlap ≥ 0.999:	
#10; 8.829 mrad	0	1.0000	1.0000	72	> 15000
	0.5	1.0000	1.0000	60	> 15000
	1	1.0000	1.0000	46	> 15000
	1.5	1.0000	1.0000	46	> 15000
	2	1.0000	1.0000	42	> 15000
	2.5	1.0000	0.9998	38	> 15000
	3	1.0000	0.9949	34	600
	4	1.0000	0.7667	29	140
	5	1.0000	0.1320	25	80
#9; 6.754 mrad	0	1.0000	1.0000	120	> 15000
	0.5	1.0000	1.0000	90	> 15000
	1	1.0000	1.0000	72	> 15000
	1.5	1.0000	0.9996	62	> 15000
	2	1.0000	0.9933	54	500
	2.5	1.0000	0.9401	46	220
	3	1.0000	0.7381	42	140
	4	1.0000	0.1145	34	80
#8; 4.414 mrad	0	0.9998	0.9998	500	< 15000
	0.5	0.9998	0.9984	220	1800
	1	0.9998	0.9811	140	300
	1.5	0.9998	0.8817	110	170
	2	0.9998	0.6094	80	110
	2.5	0.9998	0.2630	66	90
	3	0.9998	0.0606	58	72
	4	0.9998	0.0004	44	52
				Range limits for overlap ≥ 0.99:	
#7; 3.532 mrad	0	0.9952	0.9952	600	> 15000
	0.5	0.9952	0.9813	240	1050
	1	0.9952	0.8917	150	275
	1.5	0.9952	0.6360	110	160
	2	0.9952	0.2895	85	110
	2.5	0.9952	0.0716	68	85
	3	0.9952	0.0087	58	70
	4	0.9952	0.0000	44	50
				Range limits for overlap ≥ 0.90:	
#6; 2.914 mrad	0	0.9737	0.9737	325	> 15000
	0.5	0.9738	0.9290	180	> 15000
	1	0.9739	0.7386	120	475
	1.5	0.9735	0.4041	95	210
	2	0.9738	0.1268	74	130
	2.5	0.9738	0.0202	62	100
	3	0.9736	0.0015	54	78
	4	0.9734	0.0000	42	54
#5; 2.649 mrad	0	0.9506	0.9506	450	> 15000
	0.5	0.9507	0.8849	210	2800
	1	0.9510	0.6482	140	325
	1.5	0.9502	0.3093	100	170
	2	0.9506	0.0815	80	120
	2.5	0.9506	0.0107	66	90

Figure 26. Computed overlap function for various FOVs and laser-telescope inclination angles θ (with laser divergence 2.16 mrad, and laser-telescope separation 19 cm).

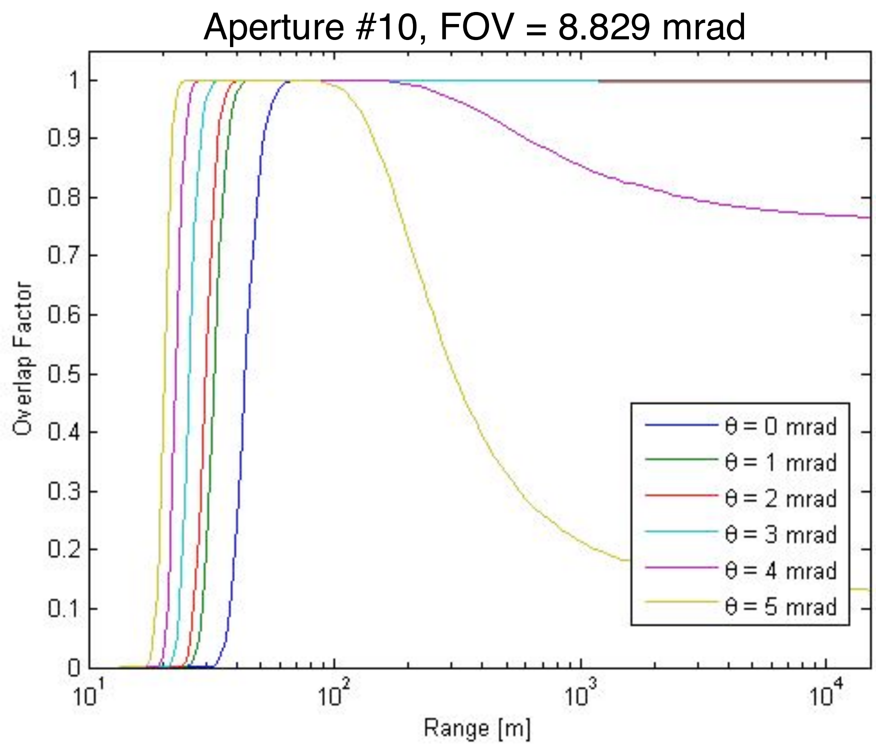

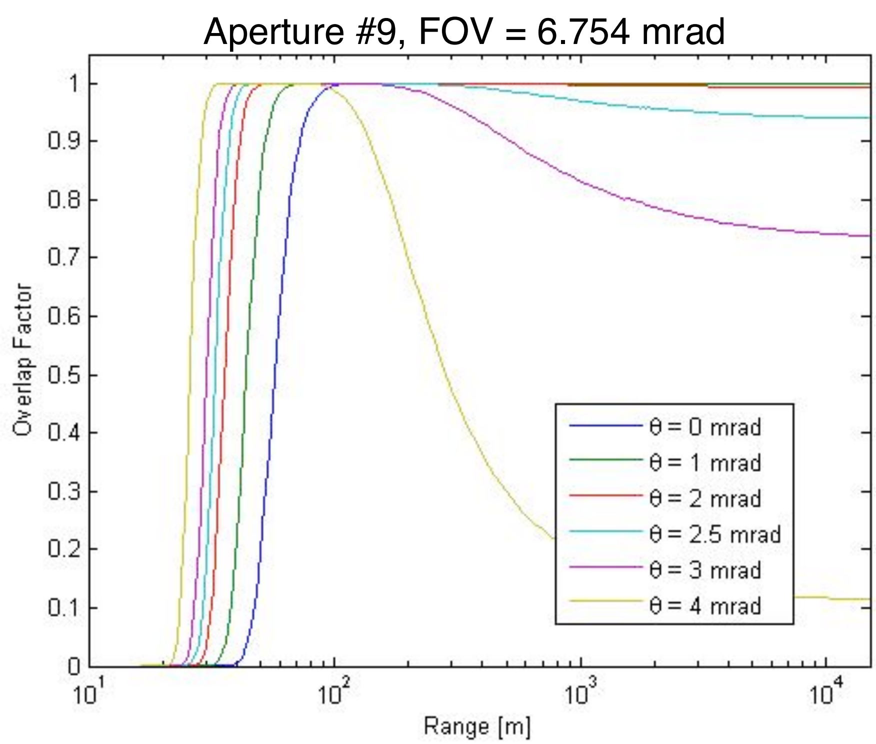

Figure 26 – continued.

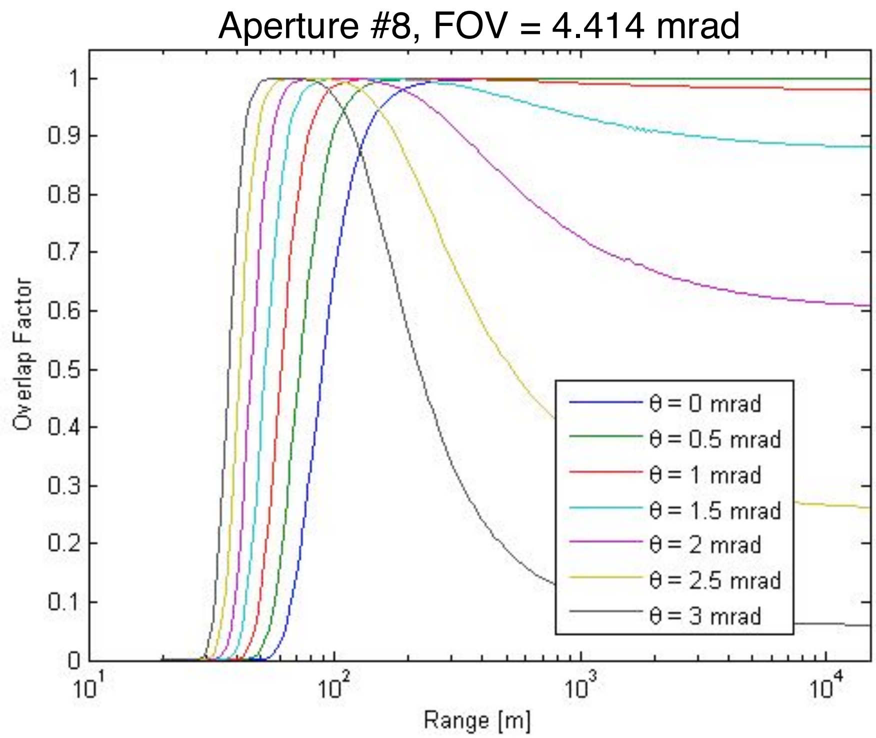

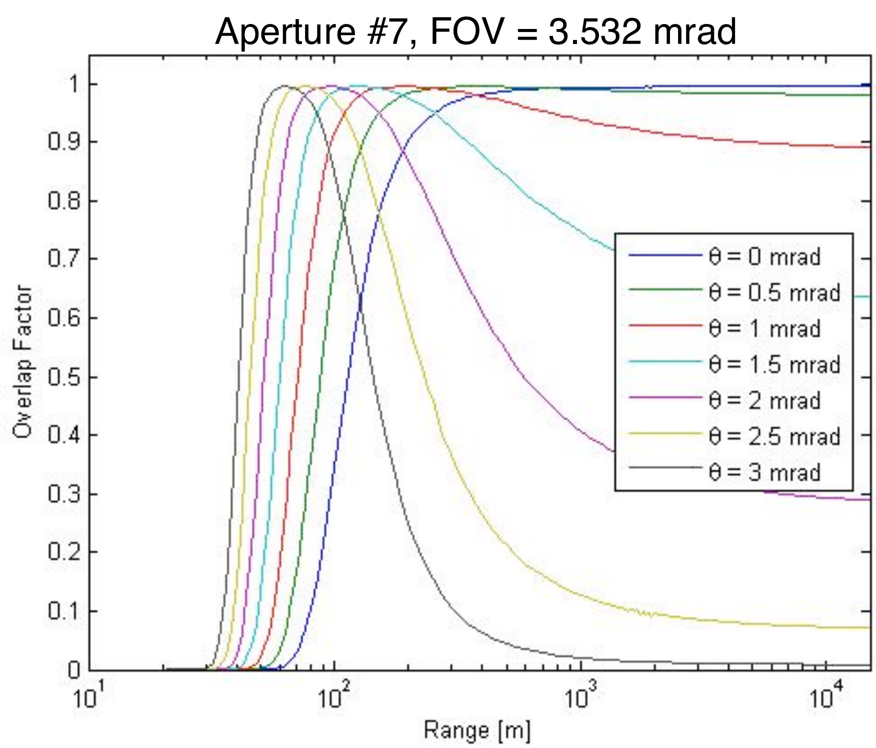

Figure 26 – continued.

Aperture #6, FOV = 2.914 mrad

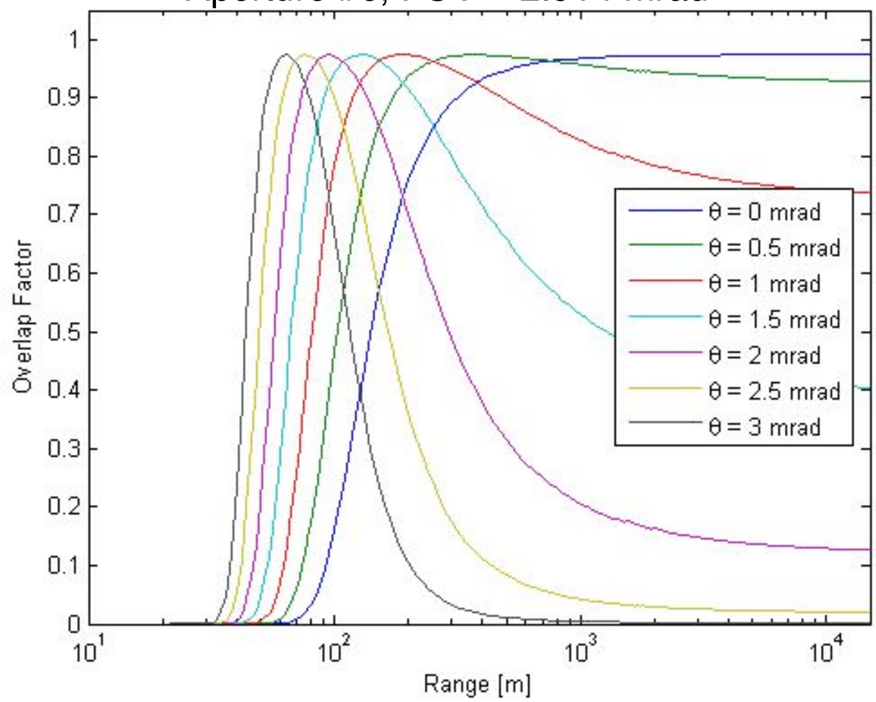

Aperture #5, FOV = 2.649 mrad

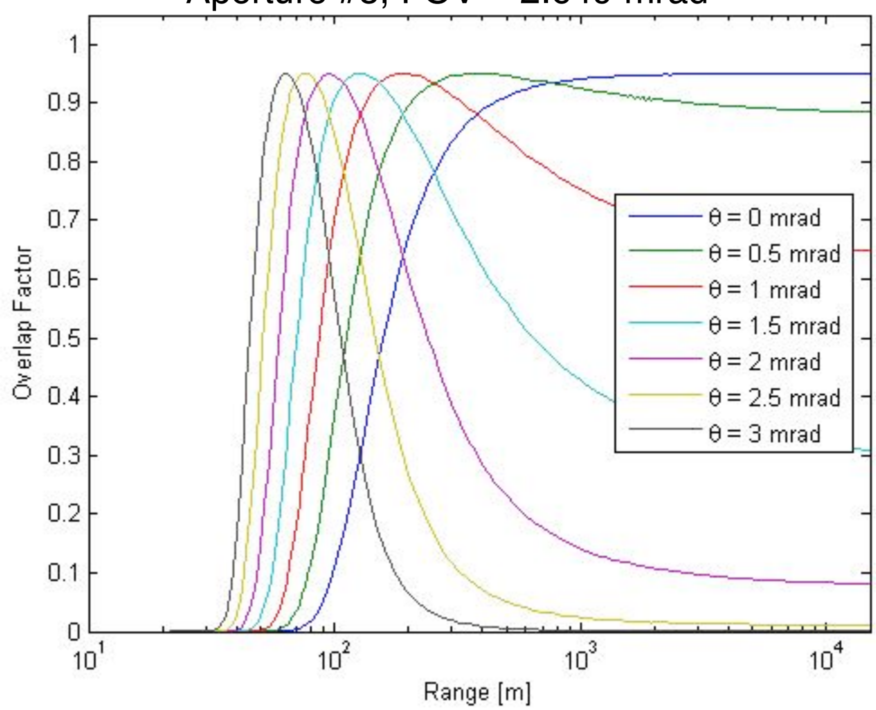

horizontal and vertical resolution at the longer ranges, where it is not needed. The overlap is computed at ranges between 5 m and 15000 m, and over those ranges, the range resolution is varied from 1 m to 500 m. The horizontal resolution is 0.5 mm for ranges up to 150 m, 0.5 cm for ranges up to 150 m, and 5 cm for ranges up to 15 km. At each range, the laser divergence is used to construct a normalized gaussian distribution in the middle of a horizontal 10001 × 10001 array. Then, the center position and size of the telescope FOV disc is determined. Finally, the sum of the normalized gaussian values inside the disc is divided by the sum of all the values, and this is the overlap fraction at this range. There are limitations on the inclination angle and divergences that make this program valid (see Appendix C). Also, the accuracy of the overlap calculation with this program will be worse for very small laser divergences and small telescope FOVs, but the values presented in Table 8 and Figure 26 are good to much better than 1%.

From Figure 26, it is clear that the inclination angle must be small to achieve an overlap of 1.0 all the way up to 15 km. For aperture #10, the inclination angle θ must satisfy $-3 \leq \theta \leq 3$ mrad; for aperture #8, it must satisfy $-0.5 \leq \theta \leq 0.5$ mrad. In practice, it is very hard to measure the inclination angle with mrad precision. The angle is controlled by the two mirrors that the steer the laser beam. The Thor Labs "Vertical Drive" mirror mounts have 50 divisions per turn of the knob, and the mirror rotates 0.005°/division. Converted to radians, and doubled for the beam deflection, it gives a resolution of 0.175 mrad/division. If the range of acceptable inclination angles is 6 mrad (such as for aperture #10), that range corresponds to about two-thirds of a turn on a mirror knob. With this resolution, it is possible to peak up the signal, but it is important not to just peak up the near-field signal, but to peak up the signal from a high cloud, if there is one.

Range Calibration

A range calibration principally involves determining the distance between the lidar instrument and the first sampled range, which is called the turn-on distance. Also, the vertical offset between the lidar and the weather station (which calibrates the weather balloon radiosondes) is found, so that the range can be referenced to the lidar or to sea level.

The weather station is located on the roof of Cobleigh Hall at Montana State University in Bozeman. A USGS map gives the ground elevation as 1500 m (4920 ft). The weather station height is measured to be 24 ± 0.5 m above the ground. This gives an elevation of 1524 m (5000 ft.) Above Mean Sea Level (AMSL). This is also the height at which weather balloons are launched, so the radiosonde software is programmed to offset its data by 1524 m, and the absolute weather station pressure calibrates the pressure measured by the weather balloon at launch. The weather station also gives the pressure relative to sea level (for comparison with other weather stations), but this value should not be used for weather balloon calibration. The lidar instrument is located beneath a roofport, 4 m below the weather station, at 1520 m AMSL.

The lidar turn-on distance is affected by the rise time of the laser pulse detector, the speed of the signal through all the cables in the system, a minimum delay in the delay generator, and the trigger bandwidths and trigger levels for the A/D card and delay generator. I determine the turn-on distance experimentally, by aiming the lidar horizontally at a concrete wall. The wall is measured to be 117.65 m from the telescope aperture. The first rise in the lidar signal occurs in the 73rd sample, which would be interpreted to be a distance of 72 × 1.5 m = 108 m, if the first sample was at 0 m. Therefore, the turn-on distance is 117.65 m – 108 m = 9.65 m.

The MATLAB processing routines use two kinds of ranges: those measured from the lidar (used to range-correct the signal) and those measured from sea level (used for comparison with radiosondes). A precise value for the speed of light in a vacuum is used, even though it only makes a difference of 10 m after 15 km. No correction for the speed of light in air is used, becuase it only makes a 0.03% difference at standard atmospheric pressure, and most of the beam path is through much lower pressures. The resulting range calibration is that the 10112 sampled ranges are described by the two MATLAB vectors:

$$\begin{aligned} &\mathit{rangesfromlidar} = 9.65 : 1.49896 : (15155.98456 + 9.65); \\ &\mathit{rangesfromsealevel} = \mathit{rangesfromlidar} + 1520; \end{aligned} \tag{3.4}$$

The turn-on distance of 9.65 m should be explained by individual delays in the system. Table 9 shows an accounting of the delays in the system from the laser pulse emission to the detection of the signal. Both the signal and sampling columns should add up to be the same if the 9.65 m distance is to be explained. The speed of the signal in a RG58/U coaxial cable is 0.66*c*. The laser pulse output photo-diode has a 1 ns rise-time, and it is verified that this trigger doesn't ring for long (~40 ns). The delay generator is set to output both the PMT gate and A/D trigger as soon as it receives this pulse, but it delays them both by 85 ns. The A/D card trigger bandwidth is 30 MHz, and the trigger level is 2.36 V. The delay generator trigger level is 2.5 V, and all trigger input impedances are

Table 9. An accouting of the system delays, counting from laser pulse emission, for the range calibration test.

ns	**Signal delays**	**ns**	**Sampling delays**
784.9	Laser pulse out to 117.65 m and back	1	Pulse detection photo-diode rise time
4.7	Transit time through receiver	23.9	Trigger cable
23.7	PMT transit time for 2.05 $V_{\text{Gain Cont.}}$	85	Delay generator
1.7	PMT rise time	23.9	Trigger cable
28.5	Signal Cable to A/D	?	A/D trigger 30 MHz bandwidth
?	A/D signal 50 MHz bandwidth	720	Sample position of the target: 10 ns times the number of samples after the first.
?	Detection threshold difference between receiver/PMT at this gain and the photodiode		
843.5 total		**853.8 total**	
10.3 ns difference, ~ 1 sample period, is attributable to the unknown values above.			

set to 50 Ω. The transit time of the PMT, specified at 16 ns for 4.5 V gain control, is longer in this case because of the low gain setting used in looking at the signal off the brick wall (the transit time is inversely proportional to the square root of the cathode-anode voltage). The cathode-anode voltage is hidden in this PMT module, but assuming the gain-control voltage is proportinal to the cathode-anode voltage, the transit time for a gain-control voltage of 2.05 V is 23.7 ns. The biggest uncertainties are the PMT transit time (which is probably 18-20 ns for the gains used in most cloud data), the effect of the bandwidths of the A/D card, and the detection threshold difference between the lidar receiver and the photo-diode. The purpose of doing this accounting is to explain the observed turn-on distance. When precise absolute ranging is required, the range should be measured relative to objects in the signal with known positions, if possible.

The laser pulse shape in time is another important piece of these timing issues. Also, as noted earlier, if we had a faster sampling rate, the measured pulse shape could be deconvolved from the data. I measure the pulse shape with a 1 ns rise-time detector (similar to the PMT's 1.7 ns rise-time). The laser is specified with a FWHM of 9.28 ns, and I measure 10.4 ns. I make a 150-point, 30 ns, pulse model from the measurements (Figure 27). After noise-subtracting and normalizing the shape to its peak, and using a 3-point median filter, the FWHM is 10.6 ns. Pulse to pulse, the FWHM stays about the same, though the structure around the peaks vary. There tend to be two maxima and the second is higher than the first.

Figure 27. 150-point model of measured laser pulse shapes, normalized from zero to one, with a 10.6 ns FWHM.

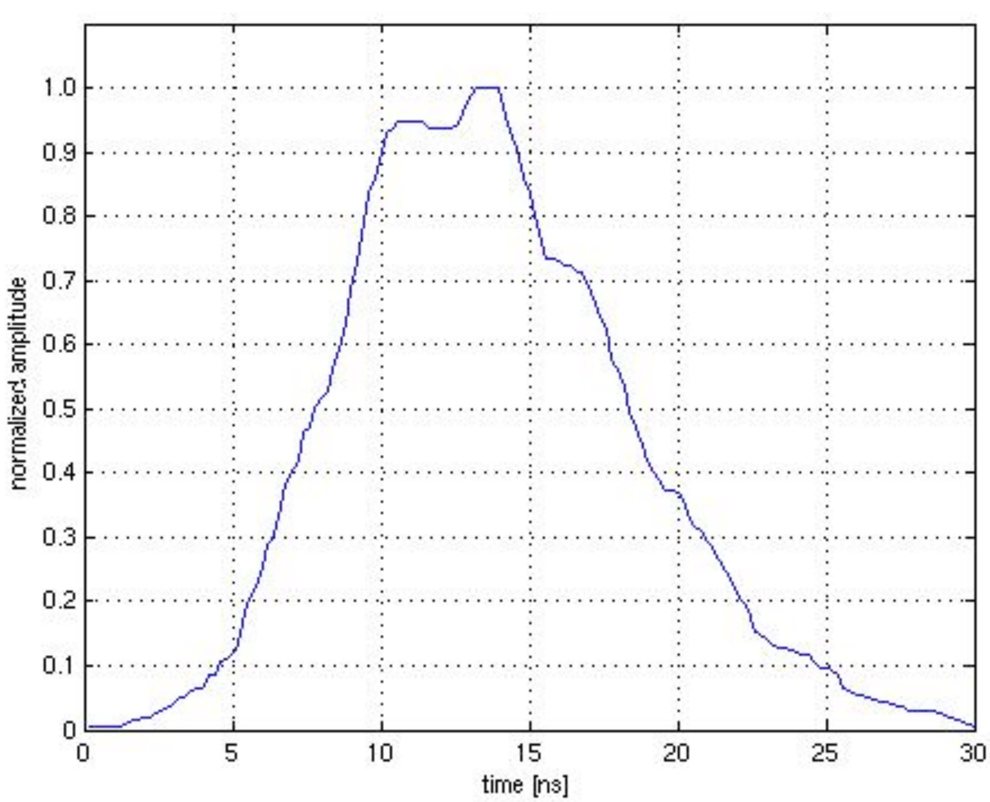

Gain Calibration and Radiometry

The photomultiplier tube gain is specified only at its peak wavelength, 420 nm, and only with a 4.5 V gain voltage. I measure the PMT responsivity (the cathode radiant sensitivity times the gain) at 12 commonly used gain control voltages, at 532 nm. This is done by switching a beam between a calibrated reference detector and the PMT, with a different amount of individually calibrated neutral density filters in each path.

The specified responsivity is 4.4×10^5 A/W, and the wavelength dependence curve shows we should be down to 57% of this value at this wavelength. At 4.5 V, Table 10 shows a responsivity of 2.53×10^5 A/W, which is only 1% off of this estimate. PMT's lose their sensitivity over time, and are typically down to 60% of their initial sensitivity after the first 100 hours of operation (Burle Technologies, 1980). This measurement shows that degradation of this sort has not been a problem thus far, but in the future, gain calibrations should be repeated periodically, and different tubes of the same model should be compared with each other. Figure 28 plots the responsivity data in Table 10, for the most common gains used. Ideally, the logarithm of the gain control voltage is proportional to the logarithm of the responsivity (as is the cathode-anode voltage). The measured points from 2.85 V gain control and above have a linear correlation coefficient of 0.9976, when plotted on a log-log scale. For gain control voltages near 3.5 V, the following relation is the best estimate of the responsivity:

$$\text{Responsivity}\left[A/W\right] = 10^{7.9\log(V_{GC})}. \qquad (3.5)$$

Having measured the laser power, receiver transmission, and detector gain, let's return to the lidar equation and put this information together. Equation 1.5 can be

Table 10. Photomultiplier tube responsivity at 532 nm as a function of the gain control voltage.

PMT Gain Cont. [V]	PMT Beam Filters Trans.	Ref. Beam Filters Trans.	Ref. Power [μW]	PMT Sig. [mV]	PMT Sig. [uA]	Responsivity V/W	Responsivity A/W	Log (A/W)
2.05	2.5454 E-01	1	5828	35.2	704	2.3728E+01	4.7457E-01	-0.3237
2.15	2.5454 E-01	1	5828	85.6	1712	5.7703E+01	1.1541E+00	0.0622
2.65	7.7792 E-03	1	5828	125	2500	2.7571E+03	5.5142E+01	1.7415
2.85	2.0270 E-04	6.2969 E-01	3631	105	2100	8.9831E+04	1.7966E+03	3.2545
3	1.2886 E-04	1.0237 E-01	585.9	91.2	1824	1.2366E+05	2.4732E+03	3.3933
3.25	3.3583 E-05	1.0237 E-01	585.4	85.6	1712	4.4574E+05	8.9148E+03	3.9501
3.5	1.3443 E-05	1.0237 E-01	585.5	76.4	1528	9.9366E+05	1.9873E+04	4.2983
3.75	4.0527 E-06	1.2354 E-02	72.29	47.6	952	2.0072E+06	4.0144E+04	4.6036
3.85	4.0527 E-06	1.2354 E-02	72.29	61.2	1224	2.5807E+06	5.1613E+04	4.7128
4	4.0527 E-06	1.2354 E-02	72.26	91.6	1832	3.8642E+06	7.7283E+04	4.8881
4.25	1.6223 E-06	1.2354 E-02	72.19	74	1480	7.8060E+06	1.5612E+05	5.1935
4.5	1.6223 E-06	1.2354 E-02	72.19	120	2400	1.2658E+07	2.5317E+05	5.4034

rewritten in terms of the detector responsivity and A/D range:

$$\begin{aligned} r^2 P(r) &= \left(r^2\left[m^2\right] Signal(r)\left[DN\right]\right)\left(\frac{ADC\ Range\left[V\right]}{8192\left[DN\right]}\right)\left(\frac{1}{50\left[\Omega\right] Responsivity\left[A/W\right]}\right) \\ &= \left(P_0 \xi_\lambda A \frac{c\tau_0}{2}\right)\beta_\pi(r) T_0^{\,2} \exp\left[-2\int_{r_0}^{r} \kappa_t(x)\,dx\right] \end{aligned} \tag{3.6}$$

Putting all the known quantities on the right side of the equation, we have:

Figure 28. Photomultiplier tube responsivity at 532 nm as a function of the gain control voltage.

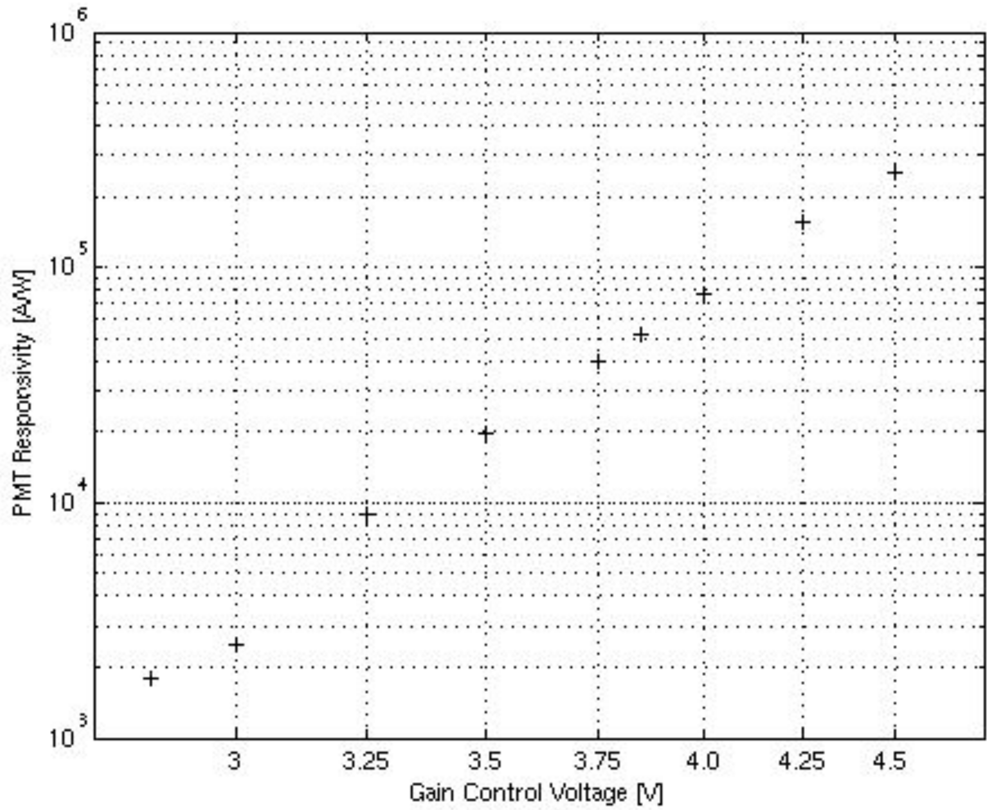

$$\beta_\pi(r)T_0^2\exp\left[-2\int_{r_0}^{r}\kappa_t(x)dx\right]$$

$$=\left(r^2\left[m^2\right]Signal(r)\left[DN\right]\right)\left(\frac{ADC\ Range\left[V\right]}{8192\left[DN\right]}\right)\left(\frac{1}{50\left[\Omega\right]Responsivity\left[A/W\right]}\right)\left(\frac{1}{P_0\xi_\lambda A\frac{c\tau_0}{2}}\right) \tag{3.7}$$

Remember that this assumes perfect overlap. The responsivity is looked up in Table 10, for a given PMT gain control voltage. The average laser power is measured to be 3.55 W. For 10 ns pulses at 30 Hz, this is equivalent to 11.83 MW power during the pulses (118 mJ pulses), so $P_0 = 1.183\times10^7\ W$ and $\tau_0 = 10^{-8}\ s$. With the transmission measured in

Table 7, for the current filter, $\xi_\lambda = 0.3652$. The area of the receiver aperture, subtracting the central obstruction, is $A = 0.028862\ m^2$. Therefore,

$$P_0 \xi_\lambda A \frac{c\tau_0}{2} = 1.8704 \times 10^5\ Wm^3 \tag{3.8}$$

The whole left side of Equation 3.7 is really just $\beta_\pi(r)T(r)^2$, the backscattering coefficient times the two-way transmission of the beam (its extinction due to absorption and scattering), which are both functions of range. Assuming a backscatter-to-extinction ratio is one strategy that allows inversion of the data, a subject that is beyond the scope of this thesis.

CHAPTER 4

CONCLUSION

Summary

The lidar system has been shown to be capable of detecting clouds or aerosols up to 9.5 km, and of measuring depolarization ratios with an error of less than 0.4%. Table 11 summarizes the system parameters.

Table 11. Summary of system parameters.

Transmitter	
Wavelength	532 nm
Pulse Repetition Rate	30 Hz
Pulse Energy	118 mJ
Beam Divergence	2.16 mrad
Pulse Width	10 ns
Receiver	
Effective Aperture Area	0.028862 m^2 (8" Schmidt-Cassegrain)
Focal Length	2265 mm
Field of View	Variable up to 8.83 mrad
Spectral filter	1 nm FWHM, normally.
Transmission	0.3652 (with 1 nm FWHM filter, see Table 7)
	0.7660 (without filter or liquid crystal)
Detector	Gated photomultiplier tube
Signal Processing	
Sample Rate	100 MS/s (1.5 m sample spacing)
Nominal Bit Depth	14 bits
Data Rate	2.16 GB/hour, with 15 km range.
Polarization	
Discrimination Method	Nematic Liquid Crystal
System Max. δ Error	<0.004 (better than 250:1)
Instrument Size	
Optics Package	31 cm wide × 46 cm deep × 97 cm tall
Electronics Rack	59 cm wide × 89 cm deep × 87 cm tall

Future Work

It has been shown that multiple scattering can cause problems with using a depolarization ratio to distinguish between liquid water and ice in clouds. The clearest solution to the problem is to limit multiple scattering by limiting the field of view. The receiver optics make the field of view easily controllable. However, with the current laser divergence, the field of view cannot be reduced much without making overlap problematic. The laser beam must be expanded and then collimated to make smaller fields of view possible. A two-lens expander must have an entrance aperture large enough for a 5.5 mm beam, a damage threshold above 1.2 J/cm^2, and must not focus retroreflections on the laser. A power of 10 would give the beam a divergence of approximately 216 μrad, which would be a significant improvement to the system.

Another intriguing way to solve the problem is not to reduce multiple scattering, but to transmit and receive circular polarization, the depolarization of which has been predicted to be less affected by multiple scattering (Hu et al. 2003). Circular polarization could be transmitted by putting a quarter-wave plate in front of the laser, and the liquid crystal would need to be tuned to quarter-wave retardance as well. In this case, scattering from liquid water is predicted to return as circularly polarized with the opposite handedness, even in dense clouds where multiple scattering is significant, while ice or other asymmetric particles should scatter with little circular polarization or circularly with the same handedness.

Another improvement to the system would be to the packaging. It is already compact and easy to transport, but it could be made more weatherproof, and the optics package should be modified to mount it securely on different platforms. Also, the zenith angle of the whole instrument should be made variable.

Finally, the lidar should be used in longer-term experiments, operating in conjunction with other instuments. The lidar system, having been characterized, is now useful, and its data should be used for further cloud studies and instrument development.

REFERENCES CITED

American National Standard Institute, 2000: American National Standard for the Safe Use of Lasers (ANSI Z136.1-2000), 163 pp.

Browell, Edward V., 1989: Differential Absorption Lidar Sensing of Ozone. *Proc. IEEE*, **77**, 419-432.

Burle Technologies, 1980: Photomultiplier Handbook. 180 pp.

Byer, Robert L., and Max Garbuny, 1973: Pollutant Detection by Absorption Using Mie Scatterring and Topographic Targets as Retroreflectors. *Appl. Opt.*, **12**, 1496-1505.

Campbell, James R., Dennis L. Hlavka, Ellsworth J. Welton, Connor J. Flynn, David D. Turner, James D. Spinhirne, V. Stanley Scott III, and I. H. Hwang, 2002: Full-Time, Eye-Safe Cloud and Aerosol Lidar Observation at Atmospheric Radiation Measurement Program Sites: Instruments and Data Processing. *J. Atmos. Oceanic Technol.*, **19**, 431-442.

Chipman, Russell A., 1999: Depolarization. *Proc. SPIE Conf. on Polarization: Measurement, Analysis, and Remote Sensing II*, **3754**, Denver, CO, 14-20.

Churnside, James H., James J. Wilson, and Viatcheslav V. Tatarskii, 2001: Airborne lidar for fisheries applications. *Opt. Eng.*, **40**, 406-414.

Collis, R. T. H., 1966: Lidar: a new atmospheric probe. *Quart. J. Roy. Meteor. Soc.*, **92**, 220-230.

Collis, R. T. H., and M. G. H. Ligda, 1966: Note on Lidar Observations of Particulate Matter in the Stratosphere. *J. Atmos. Sci.*, **23**, 255-257.

Cooney, J. A., 1968: Measurements on the Raman Component of Laser Atmospheric Backscatter. *Appl. Phys. Lett.*, **12**, 40-42.

Eberhard, Wynn L., 1992: Ice-cloud depolarization of backscatter for CO2 and other infrared lidars. *Applied Optics*, **31**, 6485-6490.

Flynn, Connor J., 2005: personal communication. MS K9-24, Battelle NW, Pacific Northwest National Laboratory, P. O. Box 999, Richland, Washington, 99352.

Frehlich, Rod, Stephen M. Hannon, and Sammy W. Henderson, 1997: Coherent Doppler lidar measurements of winds in the weak signal regime. *Appl. Opt.*, **36**, 3491-3499.

Girard, Tony: Understanding Effective Bits. Application Note AN95091, Signatec, 9 pp.

Grant, William B., 1991: Differential absorption and Raman lidar for water vapor profile measurements: a review. *Opt. Eng.*, **30**, 40-48.

Hawley, James G., Russell Targ, Sammy W. Henderson, Charley P. Hale, Michael J. Kavaya, and Daniel Moerder, 1993: Coherent launch-site atmospheric wind sounder: theory and experiment. *Appl. Opt.*, **32**, 4557-4568.

Heymsfield, Andrew J., and C. M. R. Platt, 1984: A Parameterization of the Particle Size Spectrum of Ice Clouds in Terms of the Ambient Temperature and the Ice Water Content. *J. Atmos. Sci.*, **41**, 846-855.

Hodgson, Michael E., John R. Jensen, Laura Schmidt, Steve Schill, and Bruce Davis, 2003: An evaluation of LIDAR- and IFSAR-derived digital elevation models in leaf-on conditions with USGS Level 1 and Level 2 DEMs. *Remote Sens. Environ.*, **84**, 295-308.

Hogan, Robin J., Mukunda D. Behera, Ewan J. O'Connor, and Anthony J. Illingworth, 2004: Estimate of the global distribution of stratiform supercooled liquid water clouds using the LITE lidar. *Geophys. Res. Lett.*, **31**, L05106.

Hu, Yong-X, Ping Yang, Bing Lin, Gary Gibson, and Chris Hostetler, 2003: Discriminating between spherical and non-spherical scatterers with lidar using circular polarization: a theoretical study. *J. Quant. Spectroscopy Rad. Trans.*, **79-80**, 757-764.

Intrieri, J. M., M. D. Shupe, T. Uttal, and B. J. McCarty, 2002: An annual cycle of Arctic cloud characteristics observed by radar and lidar at SHEBA. *J. Geophys. Res.*, **107**, SHE5-1-15.

Kane, Thomas J., W. J. Kozlovsky, Robert L. Byer, and Charles E. Byvik, 1987: Coherent laser radar at 1.06 μm using Nd:YAG lasers. *Opt. Lett.*, **12**, 239-241.

Kovalev, Vladimir A., and William E. Eichinger, 2004: *Elastic Lidar*. Wiley and Sons, 615 pp.

Kristjánsson, J. E., J. M. Edwards, and D. L. Mitchell, 2000: Impact of a new scheme for optical properties of ice crystals on climates of two GCMs. *J. Geophys. Res.*, **105**, 10063-10079.

Lehmann, Stefan, Volker Wulfmeyer, and Jens Bösenberg, 1997: Time-dependent attenuator for dynamic range reduction of lidar signals. *Appl. Opt.*, **36**, 3469-3474.

Leonard, Donald A., 1967: Observation of Raman Scattering from the Atmosphere using a Pulsed Nitrogen Ultraviolet Laser. *Nature*, **216**, 142-143.

Liou, Kuo-Nan, and James E. Hansen, 1971: Intensity and Polarization for Single Scattering by Polydisperse Spheres: A Comparison of Ray Optics and Mie Theory. *J. Atmos. Sci.*, **28**, 995-1004.

Liou, Kuo-Nan, and Henry Lahore, 1974: Laser Sensing of Cloud Composition: A Backscattered Depolarization Technique. *J. Appl. Meteor.*, **13**, 257-263.

Liou, Kuo-Nan, 1986: Influence of Cirrus Clouds on Weather and Climate Processes: A Global Perspective. *Mon. Wea. Rev.*, **114**, 1167-1199.

Liou, K. N., P. Yang, Y. Takano, K. Sassen, T. Charlock, and W. Arnott, 1998: On the radiative properties of contrail cirrus. *Geophys. Res. Lett.*, **25**, 1161-1164.

Liou, K. N., 2002: *An Introduction to Atmospheric Radiation*. 2nd Edition. International Geophysical Series, Vol. 84, Academic Press, 583 pp.

Meadowlark Optics, 2003: Response Time in Liquid-Crystal Variable Retarders. Application Note, 5 pp.

Measures, Raymond M., 1984: *Laser Remote Sensing*. Wiley and Sons, 510 pp.

McGuffie, K., and A. Henderson-Sellers, 2001: Forty Years of Numerical Climate Modelling. *Int. J. Climatol.*, **21**, 1067-1109.

Melfi, S. H. and D. Whiteman, 1985: Observation of Lower-Atmospheric Moisture Structure and Its Evolution Using a Raman Lidar. *Bull. Amer. Meteor. Soc.*, **66**, 1288-1292.

Pal, S. R., and A. I. Carswell, 1973: Polarization Properties of Lidar Backscattering from Clouds. *Appl. Opt.*, **12**, 1530-1535.

Platt, C. M. R., N. L. Abshire, and G. T. McNice, 1978: Some Microphysical Properties of an Ice Cloud from Lidar Observation of Horizontally Oriented Crystals. *J. Appl. Meteor.*, **17**, 1220-1224.

Pope, Robin M., and Edward S. Fry, 1997: Absorption spectrum (380-700 nm) of pure water. II. Integrating cavity measurements. *Appl. Opt.*, **36**, 8710-8723.

Post, M. J., R. A. Richter, R. M. Hardesty, T. R. Lawrence, and F. F. Hall, Jr., 1981: National Oceanic and Atmospheric Administration's (NOAA) pulsed, coherent, infrared Doppler lidar – characteristics and data. *Physics and Technology of Coherent Radar*, R. C. Harney, Ed., *Proc. SPIE,* **300**, 60-65.

Reagan, John A., M. Patrick McCormick, and James D. Spinhirne, 1989: Lidar Sensing of Aerosols and Clouds in the Troposphere and Stratosphere. *Proc. IEEE*, **77**, 433-448.

Rogers, R. R., and M. K. Yau, 1989: *A Short Course in Cloud Physics*. 3rd edition. International Series in Natural Philosophy, Vol. 113, Butterworth-Heinemann, 290 pp.

Sakai, Tetsu, Tomohiro Nagai, Masahisa Nakazato, Yuzo Mano, and Takatsugu Matsumura, 2003: Ice clouds and Asian dust studied with lidar measurements of particle extinction-to-backscatter ratio, particle depolarization, and water-vapor mixing ratio over Tsukuba. *Appl. Opt.,* **42**, 7103-7116.

Saleh, Bahaa E. A., and Malvin Carl Teich, 1991: *Fundamentals of Photonics*. Wiley and Sons, 966 pp.

Sassen, Kenneth, 1974: Depolarization of Laser Light Backscattered by Artificial Clouds. *J. Appl. Meteor.*, **13**, 923-933.

Sassen, Kenneth, Michael K. Griffin, and Gregory C. Dodd, 1989: Optical Scattering and Microphysical Properties of Subvisual Cirrus Clouds, and Climatic Implications. *J. Appl. Meteor.*, **28**, 91-98.

Sassen, Kenneth, 1991: The Polarization Lidar Technique for Cloud Research: A Review and Current Assessment. *Bull. Amer. Meteor. Soc.*, **72**, 1848-1866.

Sassen, Kenneth, and Byung Sung Cho, 1992: Subvisual-Thin Cirrus Lidar Dataset for Satellite Verification and Climatological Research. *J. Appl. Meteor.*, **31**, 1275-1285.

Sassen, Kenneth, and Hongjie Zhao, 1993: Supercooled Liquid Water Clouds in Utah Winter Mountain Storms: Cloud-seeding Implications of a Remote-Sensing Dataset. *J. Appl. Meteor.*, **32**, 1548-1558.

Sassen, Kenneth, 1994: Advances in Polarization Diversity Lidar for Cloud Remote Sensing. *Proc. IEEE*, **82**, 1907-1914.

Sassen, Kenneth, Kuo-Nan Liou, Yoshihide Takano, and Vitaly I. Khvorostyanov, 2003: Diurnal effects in the composition of cirrus clouds. *Geophys. Res. Lett.*, **30**, 1539.

Sassen, Kenneth, 2005: Dusty ice clouds over Alaska. *Nature*, **434**, 456.

Schotland, R. M., 1966: Some Observations of the Vertical Profile of Water Vapor by Means of a Lase Optical Radar. *Proc. Fourth Symposium on Remote Sensing of the Environment*, Ann Arbor, MI, University of Michigan, 271-273.

Schotland, Richard M., Kenneth Sassen, and Richard Stone, 1971: Observations by Lidar of Linear Depolarization Ratios for Hydrometeors. *J. Appl. Meteor.*, **10**, 1011-1017.

Shaw, Glenn, 2005: personal communication through Joseph A. Shaw. 903 Koyukuk Dr., University of Alaska, Fairbanks, AK, 99775-7320, gshaw@gi.alaska.edu.

Smith, Warren J., 2000: Modern Optical Engineering. 3rd Ed. *McGraw-Hill*, 617 pp.

Spinhirne, J. D., and J. A. Reagan, 1976: Gain-switching amplifier for compression of optical radar return signals. *Rev. Sci. Instrum.*, **47**, 437-439.

Spinhirne, James D., 1993: Micro Pulse Lidar. *IEEE Trans. Geosci. Remote Sens.*, **31**, 48-55.

Sugimoto, Nobuo, National Institute for Environmental Studies, Japan, cited 2005: Asian Dust Network. [Available online at http://info.nies.go.jp:8094/kosapub/index.html.]

Tan, Songxin, and Ram N. Narayanan, 2004: Design and performance of a multiwavelength airborne polarimetric lidar for vegetation remote sensing. *Appl. Opt.*, **43**, 2360-2368.

Thurairajah, Brentha, and Joseph A. Shaw, 2005: Cloud Statistics Measured With the Infrared Cloud Imager (ICI). *IEEE Trans. Geosci. Remote Sens.*, in press.

Wallace, John M., Peter V. Hobbs, 1977: Atmospheric Science. *Academic Press*, 467 pp.

Warren, Stephen G., 1984: Optical constants of ice from the ultraviolet to the microwave. *Appl. Opt.*, **23**, 1206-1225.

Weibring, Petter, Hans Edner, and Sune Svanberg, 2003: Versatile mobile lidar system for environmental monitoring. *Appl. Opt.*, **42**, 3583-3594.

Whiteman, D. N., S. H. Melfi and R. A. Ferrare, 1992: Raman lidar system for the measurement of water vapor and aerosols in the Earth's atmosphere. *Appl. Opt.,* **31**, 3068-3082.

Wilson, James J., 2003: personal communication. NOAA Environmental Technology Laboratory, 325 Broadway R/ETL, Boulder, Colorado, 80305-3328.

Winker, David M., Richard H. Couch, and M. Patrick McCormick, 1996: An Overview of LITE: NASA's Lidar In-space Technology Experiment. *Proc. IEEE*, **84**, 164-180.

Wulfmeyer, Volker, and Craig Walther, 2001: Future performance of ground-based and airborne water-vapor differential absorption lidar. I. Overview and theory. *Appl. Opt.*, **40**, 5304-5320.

Xiao, Xifeng, David Voelz, and Hiroshi Sugiura, 2003: Field of View Characteristics of a Liquid Crystal Variable Retarder. *Proc. SPIE Conf. Polarization Science and Remote Sensing*, **5158**, Bellingham, WA, 142-150.

Zhao, Yanzeng, R. M. Hardesty, and M. J. Post, 1992: Multibeam transmitter for signal dynamic range reduction in incoherent lidar systems. *Appl. Opt.*, **31**, 7623-7632.

APPENDICES

APPENDIX A:

INSTRUCTIONS FOR OPERATION

Step-by-Step Procedure and Guidelines

Startup sequence:

- Call Air Traffic Control at Bozeman (406-388-9082) and Salt Lake City (801-320-2561).
- Turn on the computer (if it is connected to the laser, the computer should be started first).
- Turn on the laser power supply to let the water temperature stabilize. Having the laser warmed up improves its pointing stability and pulse energy stability.
- Turn on the liquid crystal driver. Open "CellDRIVE 3000 Advanced" Program, only after the device is connected. Set the temperature to 40 degrees Celsius. Set channel 1 to the T.N.E. Waveform. The TNE characteristics should be set to 10 V and 5 ms. Set V1 to 2.055 V, and V2 to 4.95 V. *Don't* start that waveform running, LabVIEW will do that. It will take 10-15 minutes for the temperature to rise. Then exit the program, before starting LabVIEW.
- *Before* connecting the 9-pin connectors to the PMT, turn on the PMT power supply and gain control supply, set them to 15 V and 2.5 V, respectively, and then turn them off. Then connect the PMT 9-pin connectors.
- Turn on optical trigger detector.
- Measure and record the laser power. When the calorimeter is turned on, the mode must be set to "W", and the range to "10." (It is more accurate to measure the average power than the single pulse energy.) A typical power, at a 30 Hz pulse repetition rate, is 3.55 W. Don't turn on the laser until you have the calorimeter in position in the beam path. (Don't turn on the delay generator when the laser is on, until after the PMT power supply is on. You don't want to be triggering the PMT until it has power.) Stop the laser firing.
- Turn on the delay generator.
- In C:\MAML, click on "Maml Main Dual Pol.vi". Then start the program (click the arrow in the upper left corner).
- Start the PMT power supply (set to 15 V).
- Don appropriate eyewear. Turn on the room's laser warning light and post the magnetic warning sign outside the door. Open roofport hatch.
- Start the laser. Sequence: (1) Open shutter. (2) Flashlamp ready and then start. (3) Q-switch start.
- Start the PMT Gain Control Supply (3.0 - 3.5 V tends to be the appropriate level for cloud measurements. Never turn past 5 V!) This gain should only be turned on after there is a gate generated by the laser and delay generator.
- Check that *all three* LEDs on the PMT status indicator box are lit. If they are not, the power supply or the gain control are out of the acceptable range, or there is too much light on the PMT.
- Ensure that the proper A/D levels, PMT gain, and optics settings are entered into the software front panel, and then press the button to start taking data.

Shutdown sequence:

- Press button to stop taking data.
- Turn off PMT Gain.
- Stop laser Q-switch and Flashlamp (don't turn of the laser until the PMT gain is off).
- Turn off PMT power supply (don't turn off the supply until gates are no longer being sent to the PMT).
- Archive the data, with the button on the front panel. This may take a while if you have taken a lot of data. It could be done later, if desired. Then, press "End program" and quit LabVIEW.
- Turn off the laser supply, the liquid crystal driver, the delay generator and the optical trigger detector. If you *don't* turn off the liquid crystal driver, use the "CellDRIVE 3000 Advanced" Program to change the set temperature back down to 20 degrees Celcius.
- Shutdown computer.
- Turn off laser warning lights. Recover the magnetic laser warning sign. Call the ATC towers.
- If you launched a radiosonde, archive it, and export the data to a TSV format.

Guidelines for lidar settings:

PMT Gain, Digitizer Range, and Gated Turn-On Distance

The signal from the PMT should be kept below 1.5 V, and it is probably best to make the peak of the signal (whether it is from the near field or from a cloud) at about 1 V. I have found that making the peak of the near field signal larger than 1.5 V will affect the shape of the (lower magnitude) cloud signal from a higher altitude – this is saturation of the PMT. Also, look for both shot-to-shot and sample-to-sample oscillation in the signal after large peaks, which are characteristic of a gain level that is too high.

The A/D range should be set as small as possible, so that the signal peak is at about 90% of the full range. You don't want the range to be less than 500 mV, because below this level, the DC accuracy of the card is worse. An A/D range of 1 V is a good default value.

If there is a very faint high-altitude signal, but the large near-field signal is too big too allow it to be measured with much resolution, you may gate-out some of the near field signal, by delaying the PMT gate. A 6.667 μs delay makes the turn-on distance 1 km, for example. Enter the desired delay on the delay generator, under the delay menu once it reads A = T0 + ____. For simplicity in data processing, the A/D card is not delayed; it still samples before the PMT is gated on.

Optical Filters

For taking cloud measurements, with fields of view up to 8.83 mrad as described in this thesis, there is no reason to use a laser line filter with a bandwidth wider than 1 nm. Especially during the daytime, a 1 nm filter is significantly better at reducing the sky noise, compared to a 10 nm filter. The filters currently available for use (obtained from Andover Corp., www.andcorp.com) are labeled A through D:

Label	Model #	FWHM (nm)	Peak Transmission
A	532FS02-25, Serial #M094-54	0.88	52.12%
B	532FS02-25, Serial #M094-55	0.89	51.63%
C	532FS03-25	3.00	54.93%
D	532FS10-25	8.83	67.49%

Neutral density filters are not the best way to reduce a signal level, since the PMT dark noise is increases with the PMT gain, and using ND filters just increases the gain necessary for a given signal level.

Field of View and Alignment

Peak up the signal from a cloud, if available, with the two beam-steering mirrors. Note that just because the near-field signal is peaked up doesn't mean you have overlap at high altitudes.

A large field of view makes the alignment easy – the beam is steered into the field of view and you have complete telescope-laser beam overlap at a wide range of altitudes with good certainty. However, a smaller field of view is nice because it reduces the problems of multiple scattering, sky noise, and receiver optics incidence angles. As explained into the conclusion, the laser beam divergence must be reduced in order to have smaller fields of view and keep good overlap.

Liquid Crystal

The liquid crystal should be removed from the system if you want to take single-polarization data. (When no voltage is applied, the liquid crystal affects the polarization of the beam in an unpredictable way.)

Electronics Settings and Connections

Delay Generator Settings:

Trigger Source	External	
Trigger Level	2.5 V, Rising Edge	
Trigger Impedance	50 Ω	
T0 Output Level & Impedance	TTL, 50 Ω	(to A/D card)
AB Output Level & Impedance	TTL, 50 Ω	(required by PMT gate)
Delays:	A = T0 + 0	(unless you delay the PMT turn-on time)
	B = T0 + 120 μs	

A/D Settings:

Trigger Source	External	
Trigger Range	5 V	
Trigger Level (0-127)	60	(= 2.36 V)
Trigger Impedance	50 Ω	(important to keep the signal from the optical trigger detector from ringing)
Channels:	Single Channel	(both channels operate in ping-pong mode)
Sampling Rate	100 MS/s	
Signal Impedance	50 Ω	(important for the PMT signal to be measured over 50 Ω)

PMT Status Indicator Box:

<ins>Cable from PMT</ins>

1. 15 V Power Supply (PMT red wire)
2. Not connected
3. Gain Control Voltage (PMT white wire)
4. Not connected
5. Overlight Monitor (PMT grey wire)
6. Ground (PMT black wire)
7. Not connected
8. Supply Monitor (PMT blue wire)
9. Protect Monitor (PMT yellow wire)

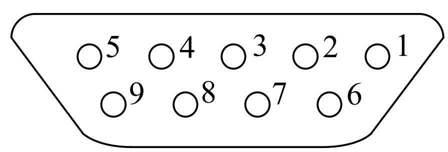

Cable from Power Supplies	Cable-Wire
1. 15 V Power Supply	A-Red
2. Tied to pin 1	A-Red
3. Connected, not used	B-Red
4. Connected, not used	A-Green
5. Gain Control Voltage	A-White
6. Ground	A-Black
7. Tied to pin 6	A-Black
8. Connected, not used	B-Green
9. Connected, not used	B-White

Connections:

- PMT Signal BNC Connector (from the PMT, split to both channels A & B on the A/D card, with equal cable lengths)
- PMT Gate BNC Connector (from PMT to delay generator's A-to-B pulse output)
- Optical Trigger Detector BNC Connector (from detector to delay generator's external trigger)
- PMT Power 9-pin Connectors (from the PMT to the PMT status indicator box, and from the rack power supplies to the PMT status indicator box)
- Liquid Crystal Driver USB cable (from liquid crystal driver to the bottom USB port on the computer PCI bus)
- Laser Serial Cable (only if you want to control the laser with the computer)
- GPS Serial Cable (if applicable)
- Liquid Crystal Temperature Cable with Lemo Connector, and Control SMA Cable (from the liquid crystal driver – LC1 – to receiver optics box)
- A/D Card Trigger BNC (from T0 trigger output on delay generator to the A/D card trigger input)
- Wall power to rack power strip and to optics power strip

Laser Safety Calculations

Safety calculations are different for pulsed lasers than for continuous-wave (CW) lasers. The tables and sections referred to below are from ANSI Z136.1-2000 (listed under the cited references) Section 8.2.3 is the section that is most relevant to our lasers.

Descriptions of our lasers:

	Laser A	*Laser B*	
Wavelength	532 nm	532 nm	
Pulse Length	10 ns	10 ns	
Pulse Repetition Rate	30 Hz	20 Hz	(The lasers are pointed striaght up
Pulse Energy	0.130 J	0.035 J	at the zenith, and are not scanned.)
Beam Divergence	2.16 mrad	5 mrad	

Skin Exposure: From Tables 6 and 7, the maximum permissible exposure for *skin*, at 532 nm, is 0.02 J/cm^2 (in 10 ns pulses), or 0.2 W/cm^2 (CW). For our lasers, the CW requirement is actually the limiting one. This gives a skin-safe beam at 76 feet for Laser A, and 14 feet for Laser B.

Eye Exposure: For ocular exposure to a pulsed laser, there are three criteria for safety:

1. *Single-Pulse MPE (Maximum Permissible Exposure)*. No single pulse should be greater than the MPE value for an exposure time equal to the pulse length.
    - For 10 ns pulses at 532 nm, this MPE = 5×10^{-7} J/cm^2 (see Table 5a).
    - For Laser A, the safe distance due to this criterion is 2663.7 m (8739 ft AGL). For Laser B, it is 597.1 m (1959 ft AGL).

2. *Average Power MPE.* The total energy of many pulses, when averaged over the total time T they take, should be beneath the MPE for a single pulse of the same total energy and an exposure time of T. This criterion is identical to the criterion for CW (Continuous-Wave) lasers.

    - At 532 nm, this MPE is 1×10^{-3} W/cm^2 (from Table 5a).
    - This puts the safe distance for Laser A at 326.3 m (1071 ft AGL). For Laser B, it is 59.7 m (196 ft AGL).

    This limit less strict than criterion #1, so it can be disregarded.

3. *Multiple-Pulse MPE.* The exposure for any single pulse should not exceed the single-pulse MPE for pulses of a certain minimum length (18×10^{-6} s for 532 nm), with that energy density multiplied by a correction factor, $n^{-0.25}$ (where n is the number of pulses in the exposure time).

    - The minimum time, for our wavelength, is 18×10^{-6} s. (from section 8.2.3.2).
    - The MPE for this minimum time is 5×10^{-7} J/cm^2 (from Table 5a.)
    - The relevant exposure time is 0.25 s, for this wavelength, for accidental viewing (from Table 4a).
    - For Laser A (30 Hz), there are n = 8 pulses in the exposure time, so the multiple pulse correction factor (calculated by $n^{-0.25}$) is 0.594. The MPE times the correction factor gives 2.97×10^{-7} J/cm^2. This puts the safe distance for Laser A at 3456.2 m (11340 ft AGL).
    - For Laser B (20 Hz), there are n = 5 pulses in the exposure time, so the multiple pulse correction factor (calculated by $n^{-0.25}$) is 0.669. The MPE times the correction factor gives 3.35×10^{-7} J/cm^2. This puts the safe distance for Laser B at 729.5 m (2394 ft AGL).

    This criterion is more strict than either criteria #1 or #2.

    Therefore, for Laser A, 11340 feet AGL is the minimum vertical height at which the beam is eye-safe. At this altitude, the beam has a lateral diameter of 25 feet.

    For Laser B, 2394 feet AGL is the minimum vertical height at which the beam is eye-safe. At this altitude, the beam has a lateral diameter of 12 feet.

APPENDIX B:

LABVIEW CONTROL SOFTWARE

Overview of the LabVIEW Virtual Instruments

The directory C:\MAML is the central directory for the LabVIEW lidar control software. New datalog (.dat) files are saved in C:\MAML\currentdata. Archived MATLAB (.mat) files are saved in C:\MAML\archiveddata. The LabVIEW Virtual Instruments are described below, and the following page shows the relationships between them.

Acquire One Shot Fast.vi Aquires one externally triggered record of 10000 samples, without changing any A/D card settings.

Archive Status Global Variable.vi Lets the front panel of the software monitor the archiving process.

Archive.vi Performs the archiving of .dat files into .mat files.

BigSky ICE TxRx.vi Communicates with the Big Sky Laser on a serial port.

Color Table Master.llb\Load Color Table.vi Loads the color table used for the shot history views on the fron panel.

Data File Global Variable.vi Gives certain settings from the front panel to the data-writing process, and gives the status of the data writing process to the front panel.

Datalog to Array.vi Reads a datalog file, record by record, into an array.

Fire.ctm A color table with warm colors that transmits well through laser googles designed for 532 nm.

Maml Main Dual Pol.vi The front panel of the lidar operation software, which calls everything else. Open this first.

Maml Main Single Pol.vi Single-polarization (no liquid crystal) version of the previous.

Maml Time Loc.vi Gets the computer's time and default location, or communicates with the GPS.

Meadowlark USB.llb Contains all the VIs for communication with the Meadowlark liquid crystal (see the hierarchy on the following page).

Optics Global Variable.vi Optics settings from the front panel are recorded here to be read by the data-writing process.

PMT Global Variable.vi Photomultiplier settings are recorded here to be read by the data-writing process.

Prepare Fast 16-bit OScope.vi Initializes the A/D card with the correct settings. Is run once per data-session.

Save Mat.vi Saves .mat files with the format particular to this system's lidar data.

Saveml.llb Contains lower level functions for saving .mat files from LabVIEW (see the hierarchy on the following page)

Time Location Global Variable.vi The time and location are continuously updated here, to be read by the front panel and the data-writing processes.

Write Data File Dual Pol.vi Writes the datalog files, switches the liquid crystal, and calls the A/D board. This is called by the front panel, and is run once for a data-taking session (multiple minute-long files).

Write Data File Single Pol.vi Single-polarization (no liquid crystal) version of the previous.

LabVIEW VI Hierarchy:

(All VIs are in C:\MAML, except the low level Gage functions, which are in C:\Program Files\National Instruments\LabVIEW 6.1\instr.lib\gage 14100\CS Sub VIs\)

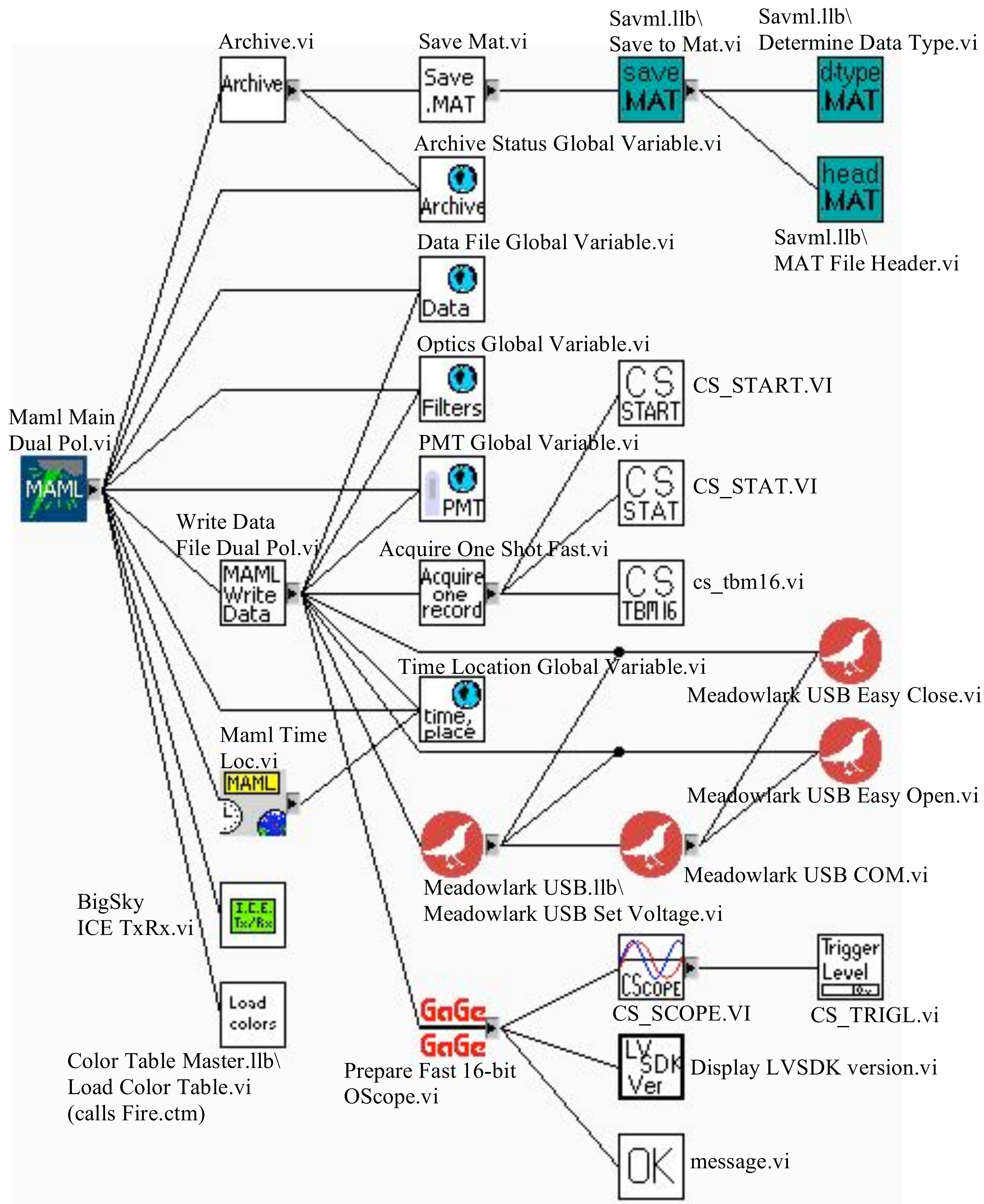

File Format

Each shot is a column with 10200 rows. Each file is for one minute (approx. 1800 shots). Each entry in this format is a single precision integer.

Row	
1-10112	Samples, in Data Numbers
10113	Second (SS)
10114	Minute (MM)
10115	Hour (HH)
10116	Day of Month (DD)
10117	Month (MM)
10118	Year (YYYY)
10119	0 if time is from computer and location is the Cobleigh default, 1 if time and location are from the GPS
10120	N Lat degrees
10121	N Lat integer minutes
10122	N Lat decimal minutes times 1000
10123	W Long degrees
10124	W Long integer minutes
10125	W Long decimal minutes times 1000
10126	Is this dual polarization data? (1 yes, 0 no)
10127	Polarizer alignment: co-pol (1), cross-pol (0), or no polarizer (2).
10128	Polarization Rotator: half-wave retardance (1), zero-retardance (0), or no rotator (2).
10129	LC Readout Voltage (times 1000)
10130	Current Data Co-pol? (1 if yes, 0 if no)
10131	Which PMT: Gated (1), R3896 (0)
10132	Gain Control Voltage – times 100
10133	Output Offset V – times 100
10134	ND Filters OD – times 100
10135	BP Filter FWHM (nm) – times 100
10036	BP Filter peak Transmission (between 0 and 10000, where 10000 corresponds to a Transmission = 1).
10137	Aperture (Field Stop) Number (1, 2, 3, etc.)
10138	A/D Card Range – A number 1 through 6 (1 = 5V, 2 = 2V, 3 =1 V, 4 = 500 mV, 5 = 200 mV, 6 = 100 mV) for both channels.
10139	Millisecond timer value. Should be about 33, if you're operating at 30 Hz.

APPENDIX C:

MATLAB DATA PROCESSING

Overlap Calculation

overlap.m

```
function [overlapfactor ranges] = overlap(laserdiv, scopefov, deltax, theta);
%[overlapfactor ranges] = overlap(laserdiv, scopefov, deltax, theta);
%
%   Computes the overlap fraction for one angle between laser and scope, and with one
%   scope FOV. Takes into account the gaussian beam shape. Models the scope FOV as a
%   perfect cone (not attenuated toward the edges).
%
%       laserdiv = laser divergence full angle in mrads.
%       scopefov = telescope full-angle field of view in mrads.
%       deltax = is the separation, in meters, and to the nearest mm, between the scope
%           and laser. It should be measured from the center of the beam to the center of
%           the scope aperture. It assumes the beam waist is located at this same
%           vertical level. This code is not designed for values of deltax greater than
%           say, 1 m.
%       theta = inclination angle between scope and laser in mrads. The laser is assumed
%           to be zenith-pointing, and the scope is inclined. The overlap shouldn't
%           change if, in reality, you tilt the laser beam instead of the scope. theta is
%           defined to be positive when the scope is tilted toward the laser.
%       ranges = are the ranges values, in meters, for the corresponding overlap
%           fractions.
%
%   Example:
%       [overlapfactor ranges] = overlap(2.16, 8.829, 0.19, 0);
%
%   Are there limits on the angles entered?
%           Yes. Small angle approximations are made. But even more important, the
%       horizontal space is defined finitely. So some combinations of angles (either the
%       scope FOV, laser divergence, and the inclination between the two) may be out of
%       range.
%           The laser is pointed at the zenith in the center of a box. The footprint of
%       the box is a square 500 m on a side. The boundary of this box (at 15 km range)
%       forms a 16.6 mrad angle from the zenith. Therefore, to be good up to 15 km, the
%       following must be satisfied:
%           Criteria #1:   scopefov(mrad)/2 + theta(mrad) < 16.6 mrad
%           Criteria #2:   laserdiv(mrad)/2 < about 3 mrad.
%       (For the lower ranges, up to 1500 m, the box is only 50 m on a side -- to get 0.5
%       cm horizontal resolution. For up to 150 m, the box is only 5 m on a side -- to
%       get 0.5 mm horizontal resolution. However, these limiting angles are the same, so
%       they don't add any additional criteria to those above.)
%
%   What is the spatial resolution?
%           The horizontal resolution is 0.5 mm for ranges up to 150 m, 0.5 cm for ranges
%       up to 150 m, and 5 cm for ranges up to 15 km. The vertical resolution varies with
%       range, to minimize computation. The ranges [m] at which it does calculations are
%       arbitrarily defined (see lowranges, midranges, and highranges in the code). So
%       the vertical resolution varys between 1 m and 500 m.
%           The accuracy of the overlap calculation is worse for small laser divergences
%       and small telescope FOVs (when they are comparable, say less than 30 times the
%       horizontal grid size). For example, the accuracy is not good for ranges < 7 m,
%       when the laser divergence angle is 2.16 mrad, since only at 7 m is the divergence
%       diameter = 15 mm. At the two points where we switch to lower (worse) horizontal
%       resolution, with a 2.16 mrad divergence, we have a divergence diameter > 60 times
%       the grid size, so we should have about 800 sampled points on the laser 1/e^2
%       disc.
disp(['Computing overlap for FOV = ' num2str(scopefov) ...
    ' mrad and theta = ' num2str(theta) ' mrad']);

%Rounds to nearest mm, but keeps the units in meters.
deltax = round(deltax*1000)/1000;

%This initializes the overlap array, and provides the 0 overlap, 0 m point.
overlapfactor = 0;

%Ranges at which to compute overlap at 0.5 mm horizontal resolution:
lowranges = [5:1:30 32:2:80 85:5:100 110:10:150];
```

```
if length(lowranges) > 0,
for n = 1:length(lowranges), %   For each range, ...
    z = lowranges(n);

    %Compute the square of the radius (in 0.5 mm units) of the laser
    %divergence at this range, and the square of the radius (in 0.5 mm
    %units) of the scope FOV at this range.
    rlaserdivsqu = ((laserdiv/1000) * (z * 2000)/2)^2;
    rscopefovsqu = ((scopefov/1000) * (z * 2000)/2)^2;

    %How far from the laser, horizontally, in 0.5 mm units, is the center
    %of the scope FOV, at this range.
    xfieldcenter = round(- deltax * 2000 + z * 2000 * theta/1000);

    %Initialize these running sums for this range.
    sumatthisrange = 0;
    suminfov = 0;

    for x = 1:10001,   %For each column,

            %Compute the fraction of the maximum [W/m^2] that exists at
            %this range, that is here in this horizontal column.
            lighthere = exp(-2*((x-5001)^2 + ((1:10001)-5001).^2) ...
                ./rlaserdivsqu);
            %Add this to the total light at this range
            sumatthisrange = sumatthisrange + sum(lighthere);

            %Where we're in the FOV, add it to a second sum.
            ind = find((((x-5001)-xfieldcenter)^2 + ...
                ((1:10001)-5001).^2) < rscopefovsqu);
            if length(ind) > 0,
                suminfov = suminfov + sum(lighthere(ind));
            end;
    end;

    %Compute the overlap at this range
    thisoverlap = suminfov/sumatthisrange;

    disp(['Range = ' num2str(z) ' m, Overlap Factor = ' ...
        num2str(thisoverlap)]);
    overlapfactor = [overlapfactor thisoverlap];
end;
end;

%Ranges at which to compute overlap at 0.5 cm horizontal resolution:
midranges = [160:10:250 275:25:500 550:50:1500];

if length(midranges) > 0,
for n = 1:length(midranges), %   For each range, ...
    z = midranges(n);

    %Compute the square of the radius (in 0.5 cm units) of the laser
    %divergence at this range, and the square of the radius (in 0.5 cm
    %units) of the scope FOV at this range.
    rlaserdivsqu = ((laserdiv/1000) * (z * 200)/2)^2;
    rscopefovsqu = ((scopefov/1000) * (z * 200)/2)^2;

    %How far from the laser, horizontally, in 0.5 cm units, is the center
    %of the scope FOV, at this range.
    xfieldcenter = round(- deltax * 200 + z * 200 * theta/1000);

    %Initialize these running sums for this range.
    sumatthisrange = 0;
    suminfov = 0;

    for x = 1:10001,   %For each column,

            %Compute the fraction of the maximum [W/m^2] that exists at
            %this range, that is here in this horizontal column.
```

```
            lighthere = exp(-2*((x-5001)^2 + ((1:10001)-5001).^2) ...
                ./rlaserdivsqu);
            %Add this to the total light at this range
            sumatthisrange = sumatthisrange + sum(lighthere);

            %Where we're in the FOV, add it to a second sum.
            ind = find((((x-5001)-xfieldcenter)^2 + ...
                ((1:10001)-5001).^2) < rscopefovsqu);
            if length(ind) > 0,
                suminfov = suminfov + sum(lighthere(ind));
            end;
    end;

    %Compute the overlap at this range
    thisoverlap = suminfov/sumatthisrange;

    disp(['Range = ' num2str(z) ' m, Overlap Factor = ' ...
        num2str(thisoverlap)]);
    overlapfactor = [overlapfactor thisoverlap];
end;
end;

%Ranges at which to compute the overlap at 5 cm horizontal resolution:
highranges = [1550:50:2000 2100:100:10000 10500:500:15000];

if length(highranges) > 0,
for n = 1:length(highranges), %   For each range, ...
    z = highranges(n);

    %Compute the square of the radius (in 5 cm units) of the laser
    %divergence at this range, and the square of the radius (in 5 cm
    %units) of the scope FOV at this range.
    rlaserdivsqu = ((laserdiv/1000) * (z * 20)/2)^2;
    rscopefovsqu = ((scopefov/1000) * (z * 20)/2)^2;

    %How far from the laser, horizontally, is the center of the scope FOV,
    %at this range.
    xfieldcenter = round(- deltax * 20 + z * 20 * theta/1000);

    %Initialize these running sums for this range.
    sumatthisrange = 0;
    suminfov = 0;

    for x = 1:10001,   %For each column,

            %Compute the fraction of the maximum [W/m^2] that exists at
            %this range, that is here in this horizontal column.
            lighthere = exp(-2*((x-5001)^2 + ((1:10001)-5001).^2) ...
                ./rlaserdivsqu);
            %Add this to the total light at this range
            sumatthisrange = sumatthisrange + sum(lighthere);

            %Where we're in the FOV, add it to a second sum.
            ind = find((((x-5001)-xfieldcenter)^2 + ...
                ((1:10001)-5001).^2) < rscopefovsqu);
            if length(ind) > 0,
                suminfov = suminfov + sum(lighthere(ind));
            end;
    end;

    %Compute the overlap at this range
    thisoverlap = suminfov/sumatthisrange;
    disp(['Range = ' num2str(z) ' m, Overlap Factor = ' ...
        num2str(thisoverlap)]);
    overlapfactor = [overlapfactor thisoverlap];
end;
end;

%Compile ranges, and account for the zero overlap at zero meters point.
ranges = [0 lowranges midranges highranges];
```

Lidar Data Functions

Most lidar data functions operate on the first 10112 rows of data only, preserving the footer information in rows 10113-10200. "*pollidar.m*" is the main routine which calls most of the others, and is the routine which should be modified depending on the sort of processing you want to do.

clip.m

```
function  y = clip( x, lo, hi )
%y = clip(x, lo, hi)
%
%   Clips a signal so values fall between "lo" and "hi".
%
%     x = input
%     lo = set everything below here to lo
%     hi = set everything above here to hi
%     y = output
%
y = (x .* [x <= hi])  +  (hi .* [x > hi]);
y = (y .* [x >= lo])  +  (lo .* [x < lo]);
```

cliplidardata.m

```
function  y = cliplidardata( x, lo, hi )
%y = cliplidardata(x, lo, hi)
%
%   Clips lidar data (where the top 10112 rows are to be clipped) so that values fall
%   between "lo" and "hi".
%
%     x = input
%     lo = set everything below here to lo
%     hi = set everything above here to hi
%     y = output
%
y = x;
y(1:10112,:) = (x(1:10112,:) .* [x(1:10112,:) <= hi])  +  ...
    (hi .* [x(1:10112,:) > hi]);
y(1:10112,:) = (y(1:10112,:) .* [x(1:10112,:) >= lo])  +  ...
    (lo .* [x(1:10112,:) < lo]);
```

dpr.m

```
function dprdata = dpr(copoldata, crosspoldata);
%dprdata = dpr(copoldata, crosspoldata);
%
%   Divides the crosspol and copol data arrays, shot by shot and sample by sample. Arrays
%   should be the same size, and should by already offset so that the sky noise level is
%   at zero. Some elements in the result will probably be Inf, -Inf or NaN.
%
dprdata = copoldata;
warning('off','MATLAB:divideByZero');
dprdata(1:10112,:) = crosspoldata(1:10112,:)./copoldata(1:10112,:);
warning('on', 'all');
```

fig2jpg.m

```
function fig2jpg(figfilename);
%fig2jpg(figfilename);
%
%   Export a saved matlab figure file (.fig) as a 300 DPI jpeg (.jpg).
%       figfilename = name of .fig file, without the '.fig'
%   The new file has the same name, but with a different extension.
%
fig = open(strcat(figfilename,'.fig'));
whichfig = strcat('-f', num2str(fig));
print('-djpeg90',whichfig,'-r300',figfilename);
close(fig);
```

formattitle.m

```
function head = formattitle(data, text, date, time, advoltage, pmtgain, aperturenum,
filterfwhm);
%head = formattitle(data, text, date, time, advoltage, pmtgain, aperturenum, filterfwhm);
%
%   Formats the title of a plot, inserting whatever information on various
%   settings that belong to that data. Assumes all the settings are the
%   same for the whole file. Uses MAML data format version 3, good for data
%   after 2/21/05.
%
%   Assumes you will include some text, or the date, or both. If you have neither, head
%   will begin with a comma. Also assumes that if you want to see any of pmtgain,
%   aperturenum, or filterfwhm, you will also want to see the advoltage. If not, the
%   second line will begin with a comma.
%
%       data  =  name of loaded MAML .mat file
%       text  =  any general name, in single quotes, for graph title.
%       data, time, advoltage, pmtgain, aperturenum, and filterfwhm should
%       be set to 1 if you want them printed to the title, otherwise set
%       them to 0.
%
%   Example:
%       head = formattitle(data,'nice plot!',1,1,0,0,0,0);

head = text;

%Date
if date ==1,
    if length(head) ~= 0; head = [head ', ']; end;
    head = [head num2str(data(10117,1),'%02d') '/' ...
        num2str(data(10116,1),'%02d') '/' num2str(data(10118,1))];
end;

%Time
if time == 1, head = [head ', ' num2str(data(10115,1),'%02d') ':' ...
        num2str(data(10114,1),'%02d') ' UTC'];
end;

%Start second line
head2 = '';

%A/D Voltage
if advoltage == 1,
    rangecode=data(10138,1);
    if rangecode==1, adrange='5 V';
    elseif rangecode==2, adrange='2 V';
    elseif rangecode==3, adrange='1 V';
    elseif rangecode==4, adrange='500 mV';
    elseif rangecode==5, adrange='200 mV';
    elseif rangecode==6, adrange='100 mV';
    else adrange='?';
    end;
    head2 = [head2 'A/D Range ' adrange];
end;

%PMT gain
if pmtgain == 1,
    head2 = [head2 ', PMT Gain ' num2str(data(10132,1)/100) ' V'];
end;

%Aperture Number
if aperturenum == 1,
    head2 = [head2 ', Aperture #' num2str(data(10137,1))];
end;

%Filter FWHM
if filterfwhm == 1,
    head2 = [head2 ', BP Filter ' num2str(data(10135,1)/100) ' nm FWHM'];
end;
```

```
%If there is anything on line 2, put a comma on line 1 and put them both in 'head'
if (advoltage + pmtgain + aperturenum + filterfwhm) > 0,
    head = {[head ',']; head2};
end;
```

getreprate.m

```
function reprate = getreprate(data);
%reprate = getreprate(data);
%
%   Gets the laser pulse repetition rate (assumes it was either 20 or 30 Hz.)
%
%       data = 2-d array of loaded .mat file
%       (row 10139 of which is the millisecond timer value between shots)
%
if median(data(10139,:)) > 42,
    reprate = 20;
else
    reprate = 30;
end;
```

hmedian15pt.m

```
function [copoldataout crpoldataout nshotsh15] = hmedian15pt(copoldata, crpoldata,
nshots);
%[copoldataout crpoldataout nshotsh15] = hmedian15pt(copoldata, crpoldata, nshots);
%
%   This runs a horizontal (shot-to-shot) 15-point running median filter of the data. It
%   is useful for removing isolated shots where the liquid crystal didn't switch
%   correctly, and for reducing noise. Don't use this on arrays that contain more than
%   one polarization.
%
copoldataout = copoldata(:,8:nshots-7);
crpoldataout = crpoldata(:,8:nshots-7);
for n = 1:(nshots-14),
     copoldataout(1:10112,n) = median(copoldata(1:10112,n:n+14),2);
     crpoldataout(1:10112,n) = median(crpoldata(1:10112,n:n+14),2);
end;
nshotsh15 = nshots-14;
```

hmedian3pt.m

```
function [copoldataout crpoldataout nshots] = hmedian3pt(copoldata, crpoldata, nshots);
%[copoldataout crosspoldataout nshots] = hmedian3pt(copoldata, crpoldata, nshots);
%
%   This runs a horizontal (shot-to-shot) 3-point running median filter of the data. It
%   is useful for removing isolated shots where the liquid crystal didn't switch
%   correctly. Don't use this on arrays that contain more than one polarization.
%
copoldataout = copoldata(:,2:nshots-1);
crpoldataout = crpoldata(:,2:nshots-1);
for n = 1:(nshots-2),
     copoldataout(1:10112,n) = median(copoldata(1:10112,n:n+2),2);
     crpoldataout(1:10112,n) = median(crpoldata(1:10112,n:n+2),2);
end;
nshotsh3 = nshots - 2;
```

hmedianall.m

```
function [copoldataout crpoldataout] = hmedianall(copoldata, crpoldata);
%[copoldataout crpoldataout] = hmedianall(copoldata, crpoldata);
%
%   This runs a horizontal (shot-to-shot) median filter of ALL the data. It is useful for
%   giving a single-shot equivalent of a whole minute of data. Don't use this on arrays
%   that contain more than one polarization.
%
copoldataout = copoldata(:,1);
crpoldataout = crpoldata(:,1);
copoldataout(1:10112) = median(copoldata(1:10112,:),2);
crpoldataout(1:10112) = median(crpoldata(1:10112,:),2);
```

imagedata.m

```
function fighandle = imagedata(data, minrange, maxrange, minamp, maxamp, sampledranges,
head, reprate);
%fighandle = imagedata(data, minrange, maxrange, minamp, maxamp, sampledranges, ...
%head, reprate);
%
%   Plots all the shots in one file as a "history view" image.
%
%       data = variable name of a processed 10200 X n array of data.
%       minrange = enter a number such as 1000, for the minimum range in meters.
%       maxrange = enter a number such as 5000, for the maximum range in meters.
%                       (Not higher than 15000.)
%       minamp = minimum amplitude (Usually 0 for ordinary data)
%       maxamp = maximum amplitude (Usually 8192 for ordinary data.)
%       sampledranges = a vector containing the heights, in meters for the
%                       sampled data.
%       head = variable name for plot title.
%       reprate = laser pulse repetition rate (Hz). Should be 20 or 30 only.
%
%   Example:
%       >> imagecopol = imagedata(copoldata, 1000, 15000, 0, 8192, ...
%           rangesfromlidar, head, reprate);

%Adjust range
sampledranges = sampledranges(1:10000);
if minrange < sampledranges(1), minrange = sampledranges(1); end;
if maxrange > sampledranges(10000), maxrange = sampledranges(10000); end;
lastsample = max(find(sampledranges <= maxrange));
firstsample = min(find(sampledranges >= minrange));
samplelocs = sampledranges(firstsample:lastsample);
maxrange = max(samplelocs);
minrange = min(samplelocs);
nsamples = length(firstsample:lastsample);
data = data(firstsample:lastsample,:);

%Display the array as an image
fighandle = figure;
imagesc(data,[minamp maxamp]);
set(gca,'YDir','normal');
colorbar;
title(head);

%Fix the X Axis, Scales and Labels
xticklocinc = reprate * 5;
%...This increment is the number of samples in 10 seconds (in dualpol data)
xticklocations = [0:xticklocinc:(xticklocinc*floor(length(data(1,:))/...
    xticklocinc))];
xticklabels = [0:10:(10*(length(xticklocations)-1))];
set(gca,'XTick',xticklocations);
set(gca,'XTickLabel',xticklabels);
xlabel('Time [s]');

%Fix the Y Axis, Scales and Labels
maxrangeinc = (maxrange-minrange)/5;
%...We want at least 5 labels on the vertical axis
possiblerangeinc = [5 10 20 25 50 100 200 500 1000 2000];
rangeincmeters = max(possiblerangeinc(find(possiblerangeinc <= ...
    maxrangeinc)));
labelsampleinc = round(rangeincmeters/1.49896);
firstlabel = ceil(minrange/rangeincmeters) * rangeincmeters;
firstlabeledsample = min(find(samplelocs >= firstlabel));
nylabels = floor((nsamples-firstlabeledsample)/labelsampleinc) + 1;
yticklocations = firstlabeledsample:labelsampleinc:(firstlabeledsample ...
    + (nylabels - 1) * labelsampleinc);
yticklabels = firstlabel:rangeincmeters:(firstlabel + (nylabels - 1) * ...
    rangeincmeters);
set(gca,'YTick',yticklocations);
set(gca,'YTickLabel',yticklabels/1000);
ylabel('Range AGL [km]');
```

imagedatarsq.m

```
function fighandle = imagedatarsq(data, minrange, maxrange, sampledranges, head,
reprate);
%fighandle = imagedatarsq(data, minrange, maxrange, minamp, maxamp, sampledranges, ...
%head, reprate);
%
%   Plots all the shots in one file as a "history view" image.
%   For use with range-squared corrected data.
%
%       data = variable name of a processed 10200 X n array of data.
%       minrange = enter a number such as 1000, for the minimum range in meters.
%
%       maxrange = enter a number such as 5000, for the maximum range in meters.
%                       (Not higher than 15000.)
%       sampledranges = a vector containing the heights, in meters for the
%                       sampled data.
%       head = variable name for plot title.
%       reprate = laser pulse repetition rate (Hz). Should be 20 or 30 only.
%
%   Example:
%       >> fig = imagedatarsq(copolh3v3osrsq, 1000, 15000, rangesfromlidar,
%       head, reprate);

%Adjust range
sampledranges = sampledranges(1:10000);
if minrange < sampledranges(1), minrange = sampledranges(1); end;
if maxrange > sampledranges(10000), maxrange = sampledranges(10000); end;
lastsample = max(find(sampledranges <= maxrange));
firstsample = min(find(sampledranges >= minrange));
samplelocs = sampledranges(firstsample:lastsample);
maxrange = max(samplelocs);
minrange = min(samplelocs);
nsamples = length(firstsample:lastsample);
data = data(firstsample:lastsample,:);

%Display the array as an image
fighandle = figure;
maxamp = ceil(max(max(data))/1000)*1000;
%...This basically auto-ranges the color scale, but I didn't want to
%autorange the minimum.
minamp = 0;
imagesc(data,[minamp maxamp]);
set(gca,'YDir','normal');
colorbar;
title(head);

%Fix the X Axis, Scales and Labels
xticklocinc = reprate * 5;
%...This increment is the number of samples in 10 seconds (in dualpol data)
xticklocations = [0:xticklocinc:(xticklocinc*floor(length(data(1,:))/ ...
    xticklocinc))];
xticklabels = [0:10:(10*(length(xticklocations)-1))];
set(gca,'XTick',xticklocations);
set(gca,'XTickLabel',xticklabels);
xlabel('Time [s]');

%Fix the Y Axis, Scales and Labels
maxrangeinc = (maxrange-minrange)/5;
%...We want at least 5 labels on the vertical axis
possiblerangeinc = [5 10 20 25 50 100 200 500 1000 2000];
rangeincmeters = max(possiblerangeinc(find(possiblerangeinc <= ...
    maxrangeinc)));
labelsampleinc = round(rangeincmeters/1.49896);
firstlabel = ceil(minrange/rangeincmeters) * rangeincmeters;
firstlabeledsample = min(find(samplelocs >= firstlabel));
nylabels = floor((nsamples-firstlabeledsample)/labelsampleinc) + 1;
yticklocations = firstlabeledsample:labelsampleinc:(firstlabeledsample ...
    + (nylabels - 1) * labelsampleinc);
yticklabels = firstlabel:rangeincmeters:(firstlabel + (nylabels - 1) ...
    * rangeincmeters);
```

```
set(gca,'YTick',yticklocations);
set(gca,'YTickLabel',yticklabels/1000);
ylabel('Range AGL [km]');
```

imagedpr.m

```
function fighandle = imagedpr(data, minrange, maxrange, mindpr, maxdpr, sampledranges,
head, reprate);
%fighandle = imagedpr(data, minrange, maxrange, mindpr, maxdpr, sampledranges, ...
%head, reprate);
%
%   Plots the DPR from all the shots in one file as a "history view" image.
%
%       data = variable name of a processed 10200 X n array of data.
%       minrange = enter a number such as 1000, for the minimum range in meters.
%       maxrange = enter a number such as 5000, for the maximum range in meters.
%                        (Not higher than 15000.)
%       mindpr = minimum value DPR to plot
%       maxdpr = maximum value DPR to plot
%       head = variable name for plot title.
%       reprate = laser pulse repetition rate (Hz). Should be 20 or 30 only.
%
%   Example:
%       >> fig = imagedpr(dprh3v3os, 1000, 15000, 0, 0.6, ...
%                        rangesfromlidar, head, reprate);

%Adjust range
sampledranges = sampledranges(1:10000);
if minrange < sampledranges(1), minrange = sampledranges(1); end;
if maxrange > sampledranges(10000), maxrange = sampledranges(10000); end;
lastsample = max(find(sampledranges <= maxrange));
firstsample = min(find(sampledranges >= minrange));
samplelocs = sampledranges(firstsample:lastsample);
maxrange = max(samplelocs);
minrange = min(samplelocs);
nsamples = length(firstsample:lastsample);
data = data(firstsample:lastsample,:);

%Display the array as an image
fighandle = figure;
imagesc(data,[mindpr maxdpr]);
set(gca,'YDir','normal');
colorbar;
title(head);

%Fix the X Axis, Scales and Labels
xticklocinc = reprate * 5;
%...This increment is the number of samples in 10 seconds (in dualpol data)
xticklocations = [0:xticklocinc:(xticklocinc*floor(length(data(1,:))/...
    xticklocinc))];
xticklabels = [0:10:(10*(length(xticklocations)-1))];
set(gca,'XTick',xticklocations);
set(gca,'XTickLabel',xticklabels);
xlabel('Time [s]');

%Fix the Y Axis, Scales and Labels
maxrangeinc = (maxrange-minrange)/5;
%...We want at least 5 labels on the vertical axis
possiblerangeinc = [5 10 20 25 50 100 200 500 1000 2000];
rangeincmeters = max(possiblerangeinc(find(possiblerangeinc <= ...
    maxrangeinc)));
labelsampleinc = round(rangeincmeters/1.49896);
firstlabel = ceil(minrange/rangeincmeters) * rangeincmeters;
firstlabeledsample = min(find(samplelocs >= firstlabel));
nylabels = floor((nsamples-firstlabeledsample)/labelsampleinc) + 1;
yticklocations = firstlabeledsample:labelsampleinc:(firstlabeledsample ...
    + (nylabels - 1) * labelsampleinc);
yticklabels = firstlabel:rangeincmeters:(firstlabel + (nylabels - 1) ...
    * rangeincmeters);
set(gca,'YTick',yticklocations);
```

```
set(gca,'YTickLabel',yticklabels/1000);
ylabel('Range AGL [km]');
```

loadmat.m

```
function data = loadmat(filename);
%data = loadmat(filename);
%
%   Loads a lidar data array from a .mat file.
%
%   filename = name of .mat file in single quotes (without the '.mat').
%   data = 2-D array.
%
%   Example:
%       data = loadmat('AA0503030511');
%
matfilename = strcat(filename,'.mat');
filestructure = open(matfilename);
data = getfield(filestructure,{1,1},filename);
```

offset.m

```
function [offsetdata offsetvalue] = offset(data);
%[offsetdata offsetvalue] = offset(data);
%
%   Uses the median of samples 9334 to 10000, for all shots, as the noise level.
%   Assumes you want the signal there to be zero (from 14-15 km).
%
%   data = variable name of 2-D data array from file, including footer.
%
offsetvalue = - round(median(median(data(9334:10000,:))));
offsetdata = data;
offsetdata(1:10112,:) = data(1:10112,:) + offsetvalue;
```

offseteachshot.m

```
function [offsetdata offsetvalues] = offseteachshot(data);
%[offsetdata offsetvalues] = offseteachshot(data);
%
%   Uses the median of samples 9334 to 10000, for each shots, as the noise level.
%   Assumes you want the signal there to be zero (from 14-15 km).
%
%   data = variable name of 2-D data array from file, including footer.
%   offsetvalues = a 1 X nshots array of values that were added to the respective shots.
%
%   Note: This routine offsets each shot separately. If you want the same offset value
%   for all shots, use 'offset.m'
%
offsetvalues = - round(median(data(9334:10000,:), 1));
offsets = ones(10112,1) * offsetvalues;
offsetdata = data;
offsetdata(1:10112,:) = data(1:10112,:) + offsets;
```

plotshot.m

```
function fighandle = plotshot(data, minrange, maxrange, sampledranges, head);
%fighandle = plotshot(data, minrange, maxrange, sampledranges, head);
%
%   Plots single-shot data.
%
%       data = 1-dimensional vector of shot data (10200 X 1)
%       minrange, maxrange = limits for data to be plotted, in meters
%       sampledranges = a vector containing the heights of the data samples, in meters.
%       head = plot title text
%
%   Example:
%       shotcopol = plotshot(copolhnos, 1100, 15000, sampledranges, head);

%Adjust range
sampledranges = sampledranges(1:10000);
```

```
if minrange < sampledranges(1), minrange = sampledranges(1); end;
if maxrange > sampledranges(10000), maxrange = sampledranges(10000); end;
lastsample = max(find(sampledranges <= maxrange));
firstsample = min(find(sampledranges >= minrange));
samplelocs = sampledranges(firstsample:lastsample);
maxrange = max(samplelocs);
minrange = min(samplelocs);
nsamples = length(firstsample:lastsample);
data = data(firstsample:lastsample);

%Plot
fighandle = figure;
plot(samplelocs/1000,data);
xlabel('Range [km]');
ylabel('Signal [DN]');
title(head);
```

pollidar.m

```
function pollidar(file);
%pollidar(file);
%
%   This routine puts one dual-polarization lidar data file through the data processing
%   pipeline and saves the results. This routine will load the file, but you need to be
%   in the right directory to start with.
%
%       file = name of lidar '.mat' file, such as 'AA0503030511'
%
%   The order of the following commands should be preserved, though some are optional,
%   and if you comment some out, you should check to see that the output of one is
%   correctly piped to the next.

%Make a new directory to move the data file into, and for all results to be saved.
mkdir(file);
curdir = pwd;
movefile([curdir '/' file '.mat'],[curdir '/' file '/' file '.mat']);
if length(sondefile) > 0,
    copyfile([curdir '/' sondefile '.mat'],[curdir '/' file '/' ...
        sondefile '.mat']);
end;
cd([curdir '/' file]);

disp('Loading .mat file');
data = loadmat(file);

disp('Getting pulse repetition rate');
reprate = getreprate(data);

disp('Splitting the data into copolarized and crosspolarized arrays');
[copoldata crpoldata nshots] = splitpols(data);

%Horizontal Median Filters
disp('Applying horizontal median filters');
[copolhn crpolhn] = hmedianall(copoldata, crpoldata);
[copolh15 crpolh15 nshotsh15] = hmedian15pt(copoldata, crpoldata, nshots);
[copolh3 crpolh3 nshotsh3] = hmedian3pt(copoldata, crpoldata, nshots);

%Vertical Median Filters
disp('Applying vertical median filters');
copolh3v3 = vmedian3pt(copolh3);
crpolh3v3 = vmedian3pt(crpolh3);

%Offset to compensate for noise level -- constant offset for all shots.
%disp('Offsetting to compensate for sky noise');
%[copolh3v3os1 offset1valco] = offset(copolh3v3);
%[crpolh3v3os1 offset1valcr] = offset(crpolh3v3);
%copolhnos1(1:10112) = copolhn(1:10112) + offset1valco;
%crpolhnos1(1:10112) = crpolhn(1:10112) + offset1valcr;

%Offset to compensate for noise level -- separate offset for each shot.
```

```
%(These make the previous offsets irrelevant.)
disp('Offsetting to compensate for sky noise');
[copolh3v3os offsetvalscoh3] = offseteachshot(copolh3v3);
[crpolh3v3os offsetvalscrh3] = offseteachshot(crpolh3v3);
[copolh15os offsetvalscoh15] = offseteachshot(copolh15);
[crpolh15os offsetvalscrh15] = offseteachshot(crpolh15);
[copolhnos offsetvalscohn] = offseteachshot(copolhn);
[crpolhnos offsetvalscrhn] = offseteachshot(crpolhn);

%R-squared factor
disp('Applying an R^2 factor correction');
%Distance calibration ...
turnondist = 9.65;
rangesfromlidar = turnondist:1.49896:(15155.98456+turnondist);
turnondist = turnondist + 1520;
rangesfromsealevel = turnondist:1.49896:(15155.98456+turnondist);
clear turnondist;
copolh3v3osrsq = rsq(copolh3v3os, rangesfromlidar);
crpolh3v3osrsq = rsq(crpolh3v3os, rangesfromlidar);
copolh15osrsq = rsq(copolh15os, rangesfromlidar);
crpolh15osrsq = rsq(crpolh15os, rangesfromlidar);
copolhnosrsq = rsq(copolhnos, rangesfromlidar);
crpolhnosrsq = rsq(crpolhnos, rangesfromlidar);

%Compute depol
disp('Compute depolarization ratios');
dprh3v3os = dpr(copolh3v3os, crpolh3v3os);
dprhnos = dpr(copolhnos, crpolhnos);
dprh15os = dpr(copolh15os, crpolh15os);

%Save all variables, except for the raw data.
disp('Saving all variables');
clear data;
newfile = strcat(file, 'results'); save(newfile);

%Plot & save images...
disp('Creating various amplitude vs. range plots');

head = formattitle(copolhnos, 'Co-pol Signal',1,1,1,1,1,1);
fig = plotshot(copolhnos, 1100, 15000, rangesfromlidar, head);
saveas(fig,strcat(file, 'plotcopolhnos.fig'));
print('-djpeg90',fig,'-r300','plotcopolhnos');
close(fig);

head = formattitle(crpolhnos, 'Cross-pol Signal',1,1,1,1,1,1);
fig = plotshot(crpolhnos, 1100, 15000, rangesfromlidar, head);
saveas(fig,strcat(file, 'plotcrpolhnos.fig'));
print('-djpeg90',fig,'-r300','plotcrpolhnos');
close(fig);

head = formattitle(copolhnosrsq,...
    'Range-corrected Co-pol Signal',1,1,1,1,1,1);
fig = plotshotrsq(copolhnosrsq, 1100, 15000, rangesfromlidar, head);
saveas(fig,strcat(file, 'plotcopolhnosrsq.fig'));
print('-djpeg90',fig,'-r300','plotcopolhnosrsq');
close(fig);

head = formattitle(crpolhnosrsq, ...
    'Range-corrected Cross-pol Signal',1,1,1,1,1,1);
fig = plotshotrsq(crpolhnosrsq, 1100, 15000, rangesfromlidar, head);
saveas(fig,strcat(file, 'plotcrpolhnosrsq.fig'));
print('-djpeg90',fig,'-r300','plotcrpolhnosrsq');
close(fig);

head = formattitle(copolh15os(:,1), ...
    'Co-pol Signal (1 second of data)',1,1,1,1,1,1);
fig = plotshot(copolh15os(:,1), 1100, 15000, rangesfromlidar, head);
saveas(fig,strcat(file, 'plotcopolh15os.fig'));
print('-djpeg90',fig,'-r300','plotcopolh15os');
close(fig);
```

```
head = formattitle(crpolh15os(:,1), ...
    'Cross-pol Signal (1 second of data)',1,1,1,1,1,1);
fig = plotshot(crpolh15os(:,1), 1100, 15000, rangesfromlidar, head);
saveas(fig,strcat(file, 'plotcrpolh15os.fig'));
print('-djpeg90',fig,'-r300','plotcrpolh15os');
close(fig);

head = formattitle(copolh15osrsq(:,1), ...
    'Range-corrected Co-pol Signal (1 second of data)',1,1,1,1,1,1);
fig = plotshotrsq(copolh15osrsq(:,1), 1100, 15000, rangesfromlidar, head);
saveas(fig,strcat(file, 'plotcopolh15osrsq.fig'));
print('-djpeg90',fig,'-r300','plotcopolh15osrsq');
close(fig);

head = formattitle(crpolh15osrsq(:,1), ...
    'Range-corrected Cross-pol Signal (1 second of data)',1,1,1,1,1,1);
fig = plotshotrsq(crpolh15osrsq(:,1), 1100, 15000, rangesfromlidar, head);
saveas(fig,strcat(file, 'plotcrpolh15osrsq.fig'));
print('-djpeg90',fig,'-r300','plotcrpolh15osrsq');
close(fig);

disp('Creating images of the data');
head = formattitle(copolh3v3os, 'Co-pol Signal [DN]', ...
    1,1,1,1,1,1);
fig = imagedata(copolh3v3os, 1000, 15000, 0, 8192, rangesfromlidar, ...
    head, reprate);
saveas(fig,strcat(file, 'imagecopolh3v3os.fig'));
print('-djpeg90',fig,'-r300','imagecopolh3v3os');
close(fig);

head = formattitle(crpolh3v3os, 'Cross-pol Signal [DN]', ...
    1,1,1,1,1,1);
fig = imagedata(crpolh3v3os, 1000, 15000, 0, 8192, rangesfromlidar, ...
    head, reprate);
saveas(fig,strcat(file, 'imagecrpolh3v3os.fig'));
print('-djpeg90',fig,'-r300','imagecrpolh3v3os');
close(fig);

head = formattitle(copolh3v3osrsq, ...
    'Range-corrected Co-pol Signal [DN km^2]',1,1,1,1,1,1);
fig = imagedatarsq(copolh3v3osrsq, 1000, 15000, rangesfromlidar, head, ...
    reprate);
saveas(fig,strcat(file, 'imagecopolh3v3osrsq.fig'));
print('-djpeg90',fig,'-r300','imagecopolh3v3osrsq');
close(fig);

head = formattitle(crpolh3v3osrsq, ...
    'Range-corrected Cross-pol Signal [DN km^2]',1,1,1,1,1,1);
fig = imagedatarsq(crpolh3v3osrsq, 1000, 15000, rangesfromlidar, head, ...
    reprate);
saveas(fig,strcat(file, 'imagecrpolh3v3osrsq.fig'));
print('-djpeg90',fig,'-r300','imagecrpolh3v3osrsq');
close(fig);

head = formattitle(dprh3v3os, 'Depolarization Ratio',1,1,1,1,1,1);
fig = imagedpr(dprh3v3os, 1000, 15000, 0, 0.6, rangesfromlidar, head, ...
    reprate);
saveas(fig,strcat(file, 'imagedepolh3v3os.fig'));
print('-djpeg90',fig,'-r300','imagedepolh3v3os');
close(fig);

disp(['Done with file ' file ' ----------']);
cd ..
```

<u>pollidardir.m</u>

```
function pollidardir;
%pollidardir;
%
%   Runs the pollidar function on each file in the current directory, one after another
```

```
%   This will treat any '.mat' file beginning with 'AA' as lidar data.
%
listdir = dir('AA*.mat');
for k = 1:size(listdir,1);
    filename = strrep(listdir(k).name, '.mat', '');
    disp(['Working on file ' num2str(k) ' of ' num2str(size(listdir,1))]);

    %Do this to each file in the directory:
    pollidar(filename);
end
clear all;
disp('Done with all files');
```

pollidarlist.m

```
function pollidarlist(filelist);
%pollidarlist(filelist);
%
%   Runs the pollidar function on each file on the list in the current directory, one
%   after another.
%       filelist = one dimensional array of .mat filenames (without the extension)
%
%   Example:
%       >> pollidarlist({'AA0503010322' 'AA0503010323'});
%
for k = 1:length(filelist);
    filename = filelist{1,k};
    disp(['Working on file ' num2str(k) ' of ' num2str(length(filelist))]);

    %Do this to each file on the list in the directory:
    pollidar(filename);
end
clear all;
disp('Done with all files');
```

rsq.m

```
function rsqdata = rsq(data, sampledranges);
%rsqdata = rsq(data, sampledranges);
%
%   Scales the amplitude of the data by a factor of range (in km) squared.
%       sampledranges = 10112 X 1 array, in meters.
%
nshots = length(data(1,:));

%The following factor has the width of nshots and the length of 10112
%samples.
rsqfactor = ((sampledranges/1000).^2)'*ones(1,nshots);
rsqdata = data;
rsqdata(1:10112,:) = data(1:10112,:) .* rsqfactor;
```

splitpols.m

```
function [copoldata crpoldata nshots] = splitpols(data);
%[copoldata crpoldata nshots] = splitpols(data);
%
%   Splits the data from a loaded .mat file into a separate array for each polarization,
%   and evens out the number of shots for each.
%
%       data = 2-d array of a loaded .mat data file
%       copoldata = 2-d array (10200 X nshots) of co-polarized shots.
%       crpoldata = 2-d array (10200 X nshots) of cross-polarized shots.
%       nshots = Number of shots

%See the data format. This looks at the orientation of the polarizer AND
%the state of the liquid crystal for each shot.
testpol=xor(data(10127,:),data(10128,:));

%Split into arrays of uniform polarization
copolind = find(testpol);
```

```
copoldata = data(:,copolind);
crpolind = find(not(testpol));
crpoldata = data(:,crpolind);

%Even out lengths of the two arrays, throwing away any extra shots
if length(crpoldata(1,:)) > length(copoldata(1,:)),
     crpoldata = crpoldata(:,1:length(copoldata(1,:)));
elseif length(copoldata(1,:)) > length(crpoldata(1,:)),
     copoldata = copoldata(:,1:length(crpoldata(1,:)));
end;

nshots = length(crpoldata(1,:));
```

Radiosonde Data Functions

readsonde.m

```
function [T, RH, Height, P, TD, w, ew, ei, wvdensity, wvdensityice, wvcolumn] =
readsonde(edtfile, newfile);
%[T, RH, Height, P, TD, w, ew, ei, wvdensity, wvdensityice, wvcolumn] ...
%   = readsonde(edtfile, newfile);
%
%   Reads a Vaisala Radiosonde Edited Data (EDT) file that has been previous exported
%   into a tab-separated ASCII format. This routine skips over the header and disregards
%   it.
%
%       edtfile = file name in the current directory, in single quotes, with the file
%           extension, such as 'edt.tsv'\
%       newfile = name (without the extension) of new .mat file to save containing the
%           data variables. Use a date and time in the name.
%
%       Returns six one-column arrays (number of data points X 1) from the sonde file:
%           T = temperature [K]
%           RH = relative humidty [%]
%           Height = Height above sea level [m]
%           P = total pressure [hPa]
%           TD = depoint temperature [K]
%           w = water vapor mixing ratio [g/kg]
%
%       Uses abswv.m to calculate vapor pressure and wvdensity:
%           ew = vapor pressure with respect to water [mb]
%           ei = vapor pressure with respect to ice [mb]
%           wvdensity = water vapor density (w.r.t. water) [g/m^3]
%           wvdensityice = water vapor density (w.r.t. ice) [g/m^3]
%           wvcolumn = integrated water vapor column [cm]
%
%    Example:
%       [T, RH, Height, P, TD, w, ew, ei, wvdensity, wvdensityice, ...
%           wvcolumn] = readsonde('edt.tsv', '20050310_021326');

%Open file
fid = fopen(edtfile);

%Skip up to the line of asterisks.
garbage1 = textscan(fid,'%[^*]');
 %Skip up until the asterisks end.
garbage2 = textscan(fid,'%[*]');
 %Skip until we see a number.
garbage3 = textscan(fid,'%[^1234567890]');

%For the rest of the file, read certain columns only.
sondedata = textscan(fid,'%*f %*f %f %f %*f %*f %f %f %f %f %*[^\n]', 'delimiter', '\t');

%Close file.
fclose(fid);
```

```
%Separate into arrays.
T = sondedata{1,1};
RH = sondedata{1,2};
Height = sondedata{1,3};
P = sondedata{1,4};
TD = sondedata{1,5};
w = sondedata{1,6};

[ew, ei, wvdensity, wvdensityice, wvcolumn] = abswv(T, TD, P, Height);

save(newfile, 'T', 'RH', 'Height', 'P', 'TD', 'w', 'ei', 'ew', ...
    'wvdensity', 'wvdensityice', 'wvcolumn');
```

abswv.m

```
function [ew, ei, wvdensity, wvdensityice, wvcolumn] = abswv(T, TD, P, Height);
%[ew, ei, wvdensity, wvdensityice, wvcolumn] = abswv(T, TD, P, Height);
%
%   Calculates the water vapor pressure (not necessarily the saturation value at a
%   specific temp) and water vapor density from the measured temperature, dewpoint
%   temperature, and total pressure.
%
%   Inputs:
%       T = Temp [K]
%       TD = Dewpoint Temp [K]
%       P = total pressure [mb] or [hPa]
%
%   Outputs:
%       ew = vapor pressure with respect to water [mb]
%       ei = vapor pressure with respect to ice [mb]
%       wvdensity = water vapor density (calculated w.r.t. water) [g/m^3]
%       wvdensityice = water vapor density (calculated w.r.t. ice) [g/m^3]
%       wvcolumn = integrated water vapor column [cm]
%
%   The formulae for saturation wv pressure come from Antoine's Equation, which is good
%   to a couple of percent for pressures over 10 torr. It has different coefficients for
%   vapor pressure over ice compared to vapor pressure over water. This makes it more
%   accurate than the Clasius-Clapeyron equation, which uses a single constant heat of
%   vaporization of water, which actually varies in the presence of ice, which holds H2O
%   with tighter bonds than liquid water does.
%       Therefore, the saturation vapor pressure over ice (esi) should be lower than that
%   over water (esw). So disregard esi for temperatures over freezing, 273 K. However, we
%   can't just disregard esw below freezing, since water is still likely present.

%Convert Temps to Celcius for use in the next equation
Tc = T - 273.15;
TDc = TD - 273.15;

%Saturation Vapor Pressure with respect to water (Antoine's Eqn)
esw = 6.1078*10.^((Tc*7.5)./(Tc+237.3));

%Actual Vapor Pressure with respect to water
ew = 6.1078*10.^((TDc*7.5)./(TDc+237.3));

%Saturation Vapor Pressure with respect to ice
esi = 6.1078*10.^((Tc*9.5)./(Tc+265.5));

%Actual Vapor Pressure with respect to ice
ei = 6.1078*10.^((TDc*9.5)./(TDc+265.5));

%Convert pressures to Pascals
Ppa = P * 100;
ewpa = ew * 100;
eipa = ei *100;

%Total air density [g/m^3] ... ideal gas law... assuming no ice:
%airdensity = 1000 * (Ppa - ewpa)./(T * 287);

%Water vapor density  ... ideal gas law:
wvdensity = 1000 * ewpa./(T * 461.5);
```

```
wvdensityice = 1000 * eipa./(T * 461.5);

%Integrate the density to find the precipitable water vapor column in cm:
%[km] * [g/m^3] = [mm] = 0.1 [cm]
wvcolumn = 0;
for n = 1:length(Height)-1,
    diffs(n) = Height(n+1)-Height(n);
    wvcolumn = wvcolumn + (diffs(n)/1000 * wvdensity(n))/10;
end;
```

loadsondemat.m

```
function [T, RH, Height, P, TD, w, ew, ei, wvdensity, wvdensityice, wvcolumn] =
loadsondemat(filename);
%[T, RH, Height, P, TD, w, ew, ei, wvdensity, wvdensityice, wvcolumn] ...
%  = loadsondemat(filename);
%
%   Loads arrays from a '.mat' file of processed radiosonde data.
%
%   filename = name of '.mat' file in single quotes (without the '.mat').
%
%   Example:
%     [T, RH, Height, P, TD, w, ew, ei, wvdensity, wvdensityice, ...
%          wvcolumn] = loadsondemat('20050301_025237');
%
matfilename = strcat(filename,'.mat');
filestructure = open(matfilename);
T = getfield(filestructure,{1,1},'T');
RH = getfield(filestructure,{1,1},'RH');
Height = getfield(filestructure,{1,1},'Height');
P = getfield(filestructure,{1,1},'P');
TD = getfield(filestructure,{1,1},'TD');
w = getfield(filestructure,{1,1},'w');
ew = getfield(filestructure,{1,1},'ew');
ei = getfield(filestructure,{1,1},'ei');
wvdensity = getfield(filestructure,{1,1},'wvdensity');
wvdensityice = getfield(filestructure,{1,1},'wvdensityice');
wvcolumn = getfield(filestructure,{1,1},'wvcolumn');
```

logpplot.m

```
function fig = logpplot(T, TD, P, wvdensity, Height);
%fig = logpplot(T, TD, P, wvdensity, Height);
%
%   Plots a "LogP-SkewT" diagram, except without the Skew.
%   If you don't want to include wvdensity on the plot, use ''
%
if length(wvdensity)>0,
    fig = plot(T-273, log10(P), TD-273, log10(P));
    axis([-90 40 2 3.006466]);
    set(gca,'YDir','reverse');
    xlabel('Temperature and Dewpoint [C]');
    yticklabels = 100:100:1000;
    yticklocations = log10(yticklabels);
    set(gca,'YTick', yticklocations);
    set(gca,'YTickLabel', yticklabels);
    ylabel('Pressure [mb]');
    ax1 = gca;
    set(ax1,'XColor','b','YColor','b')
    grid on;
    ax2 = axes('Position',get(ax1,'Position'),...
           'XAxisLocation','top',...
           'YAxisLocation','right',...
           'Color','none',...
           'XColor','r'...
           ,'YColor','b'...
           );
    hl2 = line(wvdensity,log10(P),'Color','r','Parent',ax2);
    set(gca,'YDir','reverse');
    yticklabels = 100:100:800;
```

```
    yticklocations = log10(yticklabels);
    set(gca,'YTick', yticklocations);
    axis([-Inf Inf 2 3.006466]);
    for n = 1:length(yticklabels),
         indices = find(P>=yticklabels(n));
         if length(indices)>0,
             yticklabels2(n)=Height(max(indices));
         else
             yticklabels2(n) = '-';
         end;
    end;
    set(gca,'YTickLabel', round(yticklabels2/100)/10);
    ylabel('Height AMSL [km]');
    xlabel('Water Vapor Density [g/m^3]');
else
    fig = plot(T-273, log10(P));
    axis([-90 40 2 3.006466]);
    set(gca,'YDir','reverse');
    xlabel('Temperature [C]');
    yticklabels = 100:100:1000;
    yticklocations = log10(yticklabels);
    set(gca,'YTick', yticklocations);
    set(gca,'YTickLabel', yticklabels);
    ylabel('Pressure [mb]');
    ax1 = gca;
    set(ax1,'XColor','b','YColor','b')
    grid on;
    ax2 = axes('Position',get(ax1,'Position'),...
           'XAxisLocation','bottom',...
           'YAxisLocation','right',...
           'Color','none',...
           'XColor','b'...
           ,'YColor','b'...
           );
    hl2 = line(TD-273,log10(P),'Color','g','Parent',ax2);
    set(gca,'YDir','reverse');
    yticklabels = 100:100:800;
    yticklocations = log10(yticklabels);
    set(gca,'YTick', yticklocations);
    axis([-90 40 2 3.006466]);
    for n = 1:length(yticklabels),
         indices = find(P>=yticklabels(n));
         if length(indices)>0,
             yticklabels2(n)=Height(max(indices));
         else
             yticklabels2(n) = '-';
         end;
    end;
    set(gca,'YTickLabel', round(yticklabels2/100)/10);
    ylabel('Height AMSL [km]');
end;
```